UNIVERSITÀ DEGLI STUDI DI TRIESTE

XXV CICLO DEL DOTTORATO DI RICERCA IN

FISICA

SINGLE PHOTON COUNTING SYSTEM FOR MAMMOGRAPHY WITH SYNCHROTRON RADIATION

Settore Scientifico-disciplinare FIS/07 Fisica Applicata

Dottoranda:
Frances Caroline M. Lopez

Supervisore:
Prof. Renata Longo

Coordinatore:
Prof. Paolo Camerini

ANNO ACADEMICO 2011-2012

UNIVERSITY OF TRIESTE

CYCLE 25 - PHD SCHOOL IN PHYSICS

SINGLE PHOTON COUNTING SYSTEM FOR MAMMOGRAPHY WITH SYNCHROTRON RADIATION

Scientific Discipline FIS/07 Applied Physics

Candidate:
Frances Caroline M. Lopez

Research Supervisor:
Prof. Renata Longo

PhD School Coordinator:
Prof. Paolo Camerini

SCHOOL YEAR 2011-2012

Contents

List of Figures

List of Tables

Abstract

Digital imaging systems for medical applications must be based upon highly efficient detectors to ensure low patient dose. This is considerably important, especially in mammography, because the high sensitivity of the breast to radiation. A mammoraphy system must also provide high spatial and contrast resolution to be able to detect important structures related to breast malignancies.

The work performed and described in this thesis is the development of a readout system for a detector optimised for clinical mammography with synchrotron radiation. The detector called PICASSO (Phase Imaging for Clinical Application with Silicon detector and Synchrotron radiatiOn) is developed mainly for the mammography station of the SYRMEP beamline. The detector described in this work is based on Silicon microstrip sensors that are illuminated *edge-on*. The incoming beam impinging the detector is parallel to the strips of its sensors. This configuration permits high detection efficiency in the energy range that is of interest for mammography. Moreover, the Silicon sensors also allow direct conversion of X-rays.

The readout electronics of the Picasso detector works on single-photon counting mode. That is, only signals from photons that are equal or greater than a pre-set threshold are counted, and low freqency noise are automatically rejected. The visibility of small details, normally valuable in mammograms, are maximised because the system is *quantum limited*, *ie,* the quality of the image is limited only by the intrinsic fluctuation of the detected photons.

Picasso has four layers, each containing three detector modules. The layers are grouped into pairs and arranged one in front of the other along the beam of propagation. The pairs are controlled separately but are working in parallel. The system is a modular detector that implements a read-out system with MYTHEN II ASICs, an embedded Linux-based controller board and a Scientific Linux acquisition workstation. The developed system architecture and its characteristics will be presented.

Preliminary imaging tests were perfomed and results with the new system will be presented. Standard mammographic phantoms were imaged and good quality images were obtained at doses comparable with what is delivered in conventional full field mammographic systems. The whole system was able to sustain fast acquisition speeds up to $10ms/frame$ and runs stable until a breast-equivalent length acquisition is accomplished. A delay between frame of 150μs and delay between controllers of around 750μs is achieved.

Phase-contrast imaging has revolutionized the face of mammography with synchrotron radiation in the last ten years as the first clinical phase has been successfully implemented in our facility. This initial step made use of commercial screen-film system producung promising results. Thanks to the coherence and monochromaticity of light coming from synchrotron sources that edge-enhancement in the image is achieved due to phase effects. The compatibility of the Picasso detector to phase-contrast imaging with other novel techniques has also been evaluated in line with this project. Phase-contrast was well demonstrated with the system, details of which will be fully described.

Riassunto

I sistemi di imaging per la radiologia devono essere basati su rivelatori di alta efficienza per ottenere immagini di buona qualità con una dose contenuta al paziente. Questo è importante soprattutto in mammografia data l'elevata sensibilitá del tessuto mammario alle radiazioni ionizzanti. Un sistema per mammografia deve anche fornire immagini con alta risoluzione spaziale ed in contrasto per permettere la diagnosi precoce del tumore al seno.

In questo lavoro di tesi è stato sviluppato un sistema di lettura per un rivelatore disegnato e ottimizzato per la mammografia clinica con luce di sincrotrone. Il rivelatore, chiamato PICASSO (Phase Imaging for Clinical Application of Silicon detector and Synchrotron radiatiOn), é stato sviluppato principalmente per la linea di luce mammografia SYRMEP (SYnchrotron Radiation for MEdical Physics). Il rilevatore descritto in questo lavoro si basa su sensori a microstrip di silicio illuminati in geometria detta "edge-on": il fascio di radiazione che colpisce il rivelatore è parallelo alle microstrip. Questa configurazione consente un'alta efficienza nell'intervallo di energia che è utilizzata in mammografia. Inoltre, i sensori di silicio permettono la conversione diretta di raggi X in segnale elettrico. L'elettronica di lettura del rivelatore PICASSO è basata sul conteggio dei singoli fotoni: quando il segnale, la cui ampiezza è proporzionale allenergia depositata dal fotone nel silicio, è uguale o superiore ad una predeterminata soglia viene contata, in questo modo il segnale dovuto al rumore è automaticamente scartato. Così facendo la visibilità dei dettagli di piccole dimensioni o di basso contrasto, importantissimi in mammografia, è massima poichè la qualità dell'immagine è limitata solo dalla fluttuazione intrinseca dei fotoni rilevati.

Il rivelatore PICASSO è costituito da quattro strati di sensori di silicio, contenenti ciascuno tre moduli dellelettronica di lettura del segnale. Gli strati sono organizzati in coppie e disposti uno dopo l'altro lungo lasse di propagazione del fascio di fotoni. Le coppie sono controllate separatamente, ma lavorano in parallelo. Il sistema è dunque modulare e ciascun modulo è basato sugli ASIC MYTHEN II ed un controller con embedded Linux, una workstation (scientific Linux) controlla quindi lacquisizione dallintero detector. L'architettura di sistema sviluppata in questo lavoro di tesi e le sue caratteristiche sono presentate e discusse in dettaglio. Inoltre vengono presentati i risultati dei primi test di imaging: sono stati studiati oggetti test mammografici e sono state ottenute immagini di buona qualit a dosi paragonabili a quelle depositate con i sistemi mammografici convenzionali. L'intero sistema è in grado di sostenere un'alta velocita di aquisizione fino a 10 *ms/frame* e permette quindi di acquisire in scansione immagini di oggetti delle dimensioni richieste in mammografia. Il ritardo tra due acquisizioni (frame) successive è di 150μs ed il ritardo tra i due controller è di circa 750μs.

L'imaging a contrasto di fase ha rivoluzionato la mammografia con luce di sincrotrone negli ultimi dieci anni, ed il primo studio clinico è stato realizzato con successo presso la linea di luce SYRMEP. In questa fase iniziale è stato usato un sistema schermo-pellicola commerciale con risultati promettenti. Grazie alla coerenza e monocromaticità della luce di sincrotrone le mammografie ottenute sono caratterizzate dagli effetti di fase che migliorano la visibilità di dettagli altrimenti poco visibili. La compatibilità del rivelatore PICASSO con le tecniche di imaging in contrasto di fase è stata verificata con successo e ci si aspetta quindi di poterlo utilizzare presto per gli studi clinici.

Introduction

Breast cancer remains to be the one of the most frequently diagnosed cancer and leading cause of deaths among females across the globe representing 23% of the total cancer cases and 14% of the cancer mortalities [1]. In various races, ethnicities, population structures, socioeconimic circumstances, quality of healthcare services and access to treatment, the global burden on the incidence of breast cancer over the years have not differed noticably. Albeit the decrease in mortality rate from this malignancy across many populations, survival rates remained a challenge to address [2, 3, 4, 5]. In a country like the United States that has a multi-ethnic and multi-race population for instance [6], incidence rates of breast cancer remained high in the past three decades. Much of the historic increase in the incidence of this disease was attributed to reproductive patterns. Some of the noted ones are delayed child-bearing and having less children, which are recognised risk factors for breast cancer. Towards the end of the past centrury, mortality rate has declined thanks to the improvements in breast cancer treatment and early detection. See Figure 1.

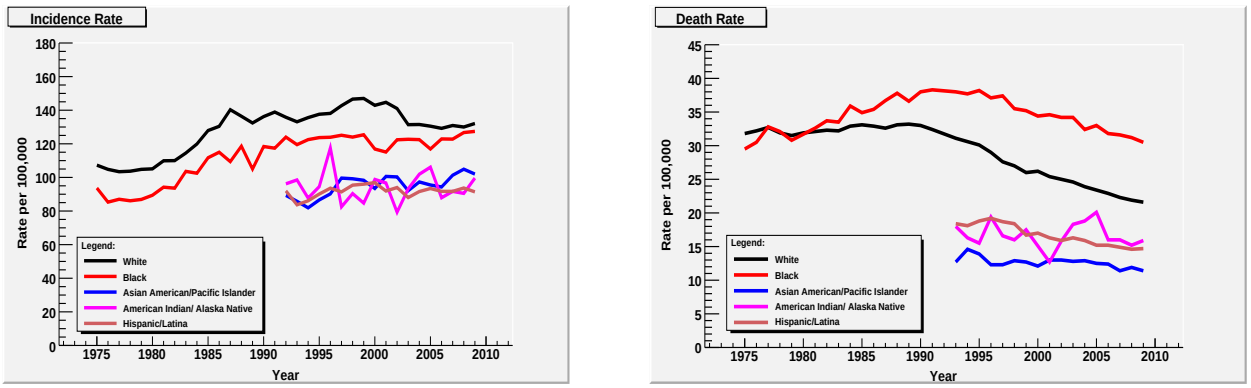

Figure 1: Trends in Female Breast Cancer by Race and Ethnicity, US, 1975-2009[6]

With the current medicine practice, mammography with the use of X-rays is one of the standard and most powerful tool for breast cancer detection and population screening. Big masses and nodules having the size of a few millimeters with almost the same absorption properties as the neighboring structures, and small microcalcifications of high contrast are among the structures that need to be well studied as they are two important indicators of breast cancer. In addition, distortion and assymetry of certain patterns in the breast are good measures of the pathology that may warrant the need for assessment using this tool. In the present routine examination with use of X-ray mammography, the radiation is normally produced by x-ray tubes usually with fine-focus Molybdenum or Rhodium targets. Sources of this kind emit photons with energies on a very wide spectrum, having its low energy end only being absorbed by the tissue consequently contributing less in the formation of good quality in the image, and contributing only to an increase in the absorbed dose to the patient. The use of mochromatic beams presents a very good promise in breast imaging, thanks to synchrotron sources that produce light that may be monchromatised and is characterised by high intensity properties. Since the brilliance of the light is so high, it is possible to position the detector in a significantly large distance comparared to that of conventional mammographic units so that phase-contrast techniques may be employed. In this case, the phase shifts of the wave passing through a sample may be detected.

The SYRMEP team in Trieste (Italy) has been actively involved in imaging activities since the mid-1990s after the proposal to build a beamline dedicated to medical physics and imaging in 1986. They have been involved with the development of novel imaging techniques, particularly phase-contrast imaging. The methods developed seem to have a good potential in mammography that the construction of a clinical station

dedicated for breast imaging was realised. The clinical mammography project at the SYRMEP beamline started in 2006 and has successfuly admitted 71 patients in a span of three years using an area detector commercially sold screen-film system used in a scan mode. A full description of the facility will be described in Chapter 1.

Many mammography systems usually have an area detector that covers the whole image field. Usually there are two standard sizes for film screen : 18 cm x 24cm and 24cm x 30cm where the longer dimension is positoined parallel to the chest wall. These would also be the typical areas for digital mammography, however maybe somewhat different. The area detetor may be made as a single continuous piece or aggregate of several parts.

X-ray interactions that dominate inside the breast is photoelectric effect, but Compton scattering and coherent scattering do play important roles. In the energy range useful for mammography, cross-sections for photoabsorption in general decrease with E^{-3}, energy to the minus three, the cross-section for Compton is essentially not variable while coherent scattering goes down with $E^{1.5}$. All the photon energy is transfered to the breast with photoelectric effect. Compton scattering transfers only a fraction of the energy while the rest constitutes a photon scattered relative to the beam propagation direction described by the Klein-Nishina formulation

$$E_s = \frac{E}{1 + \frac{E}{m_e c^2}(1 - \cos\theta)}. \tag{1}$$

E_s is the scattered photon energy, θ is the scattering angle, m_e is the electron mass and c is the speed of light. These scattered radiation from the breast are detected and will appear as noise in the detector, hench Bucky grids are usually used for conventional area detectors. Scanning devices also exists that would usually have sensors with small areas and that they are moved accross the object during acquisition. The beam has to be collimated to match the detector area before passing the sample Also, since the detector is small, the probability of the scatterd radiation interacting with the pixel is low. Already because of this inherent rejection, scanning system are not built with grids

In conventional radiography, the signal that reaches the readout electronics (also in films) is generally proportional to its energy. In a digital system, the signals generated by the interacting photons in a pixel are integrated and then digitized to form a pixel value. Screen-film systems also do the same, although the blackening is a logarithmic function of the total energy. Counting individual photons is actually more efficient treatment of information compared to just recording the total deposited energy. This is done by recording the number of pulses above an electronic threshold level, given that the noise from the detector and the front-end electronics is smaller than the least energetic photons. A direct convesion such as Silicon is used to ensure sufficient signal-to-noise ratio. One advantage of photon-counting systems is that the detector and electronic noise do not appear in the image as they do in integrating systems. There is a fundamental limit in the signal-to-noise ratio of a pixel value and it is given by the statistical distribution that photons passing through the breast follow. This is called quantum noise, and a system performing in this limit is said to be quantum limited. In this sense, noise rejection provides photon counting systems the potential of being quantum limited. For this reason, the detector of choise to be developed for the mammography project at our beamline is a *single-photon counting detector*.

Performing mammography, especially with the use of scanning systems, poses several strict requirements on its detection systems. Typically, one would require that the detector is fast in terms of rate and readout as patient imaging has to be perfomed in a matter of seconds. Discomfort causes voluntary and involuntary movement from the subject, as a consequence motion artifacts impairs the image.

Mammographic studies often would deal with microcalcifications and nodules. Ductal carcinoma *in situ*, a malignant tumor, normally shows calcifications. Metastases from non-breast primary tumor should be suspected when a patient has a known primary tumor and there are multiple bilateral, mostly circumscribed nodules without associated suspect microcalcifications [7]. Therefore, a good detector must offer high spatial and contrast resolution. In addition for our case, it should aslo be capable of detecting phase effects. And ultimately a detector with high efficiency is favored so that the dose delivered to the patient is as low as reasonable as possible.

In the following chapters, a brief overview of synchrotron radiation in relation to medical imaging will be introduced. In particular, the SYRMEP (SYnchrotron Radiation for MEdical Physics) beamline [8] where all of the imaging activities involved in this project will be presented. Summary on silicon detectors will

also be layed out.

The core of this thesis is the work done with the PICASSO (Phase Imaging for Clinical Application with Silicon detecor and Synchrotron radiatiOn) detector. This digital detector has been developed primarily to supply an in-house development to address the imaging needs of the SYRMA, a clinical mammography research study with the use of synchrotron radiation at Elettra. Mainly, much of the work was on the development of a new read-out system for the four layers of the Picasso detector. This system is based on an embedded linux system that is compact, fast, low in noise and reliable for clinical research. The details of the detector archietcture are presented in Chapter 3.

Chapter 4 and Chapter 5 deals mainly with the imaging tests involving the detector. Work on detector characterization will be discussed, and initial results using the readout electronics will be presented. Chapter 5 is devoted to phase-contrast imaging activities performed at the Syrmep beamline using this detector. The compatibility of the detector has been evaluated with novel imaging techniques. The final chapter concludes with the tests perfomed with the completed assembly.

Chapter 1

Synchrotron Radiation and the SYRMEP Mammography Station

The discovery of X-rays by Röntgen has a profound effect on the history of medicine with the first images he produced in 1895 by then some unknown rays [9]. Within a few weeks of discovery, X-rays has been applied to diagnosis, and shortly after, to therapy. In the present, it is virtually unimaginanble for medicine without X-rays. For several decades, they were generated solely by X-ray tubes, until machines in confined near-circular paths generated these photons from accelerated charged-particles (electrons and protons) travelling the speed of light thereafter called synchrotron radiation. When these charged-particles travel in relativistic speeds, such the one travelling on a curved trajectory, will emit radiation [11]. The first observation was noted at General Electric Reseach Laboratory in the middle part of the 20th centiry, which led to the construction of synchrotron radiation facilities because of the its interesting characteristics that first appealed to the high energy physics community. Eventually, these facilities have evolved and were built many scientific reseach that embarked a new face in X-ray science. These include physics, material science, crystallography, nanotechnology, medicine, health care, and biological science to name a few.

In medicine, the advent of synchrotron radiation stimulated many areas of diagnosis and therapeutics. In 1986, angiographic research on patients using KES (k-edge subtraction) technique with synchrotron radiation [12] gained attention. Thereafter, a number of medical research involving this peculiar beam were developed.

In this chapter, fundamental properties of synchrotron radiation will be discused. The synchrotron radiation facility where this reserach activity moved about will be described, giving focus on the SYRMEP beam line and its clinical facility, which has been the motivation why the PICASSO detector has been built.

1.1 Synchrtron Radiation

Historicallly, synchrotron radiation was first noted as lost energy from electron storage rings. These first generation synchrotron accelerators were not dedicated for "probing" as it is today, however it was used in a parasitic way alongside with high energy physics experiments. Over time, dedicated synchrotron sources for has been built with the use of bending magnets.

Synchrotron radiation gave an imporant contribution in interdisciplinary science and has been tremendously successful with the influx of third generation synchrotron facilities. These structures were composed of many straight structures optimised for insertion devices that can produce very bright light. This revolution leaped forward in the 1990s when the first batch of these sources started to become available providing extremely brilliant beams in the 100 nm to 1 μm range that benefitted not only physicists, but also various sectors in structural biology [13, 14], chemistry, materials science and crystallography [15], medicine [16] and many others.

1.1.1 Generation of Synchrotron Radiation

Synchrotron radiation is generated from accelerated chared particles (electrons, for instance) travellling at relativistic speeds traversing a curved track in a magnetic field. At this speed, the radiation is emitted

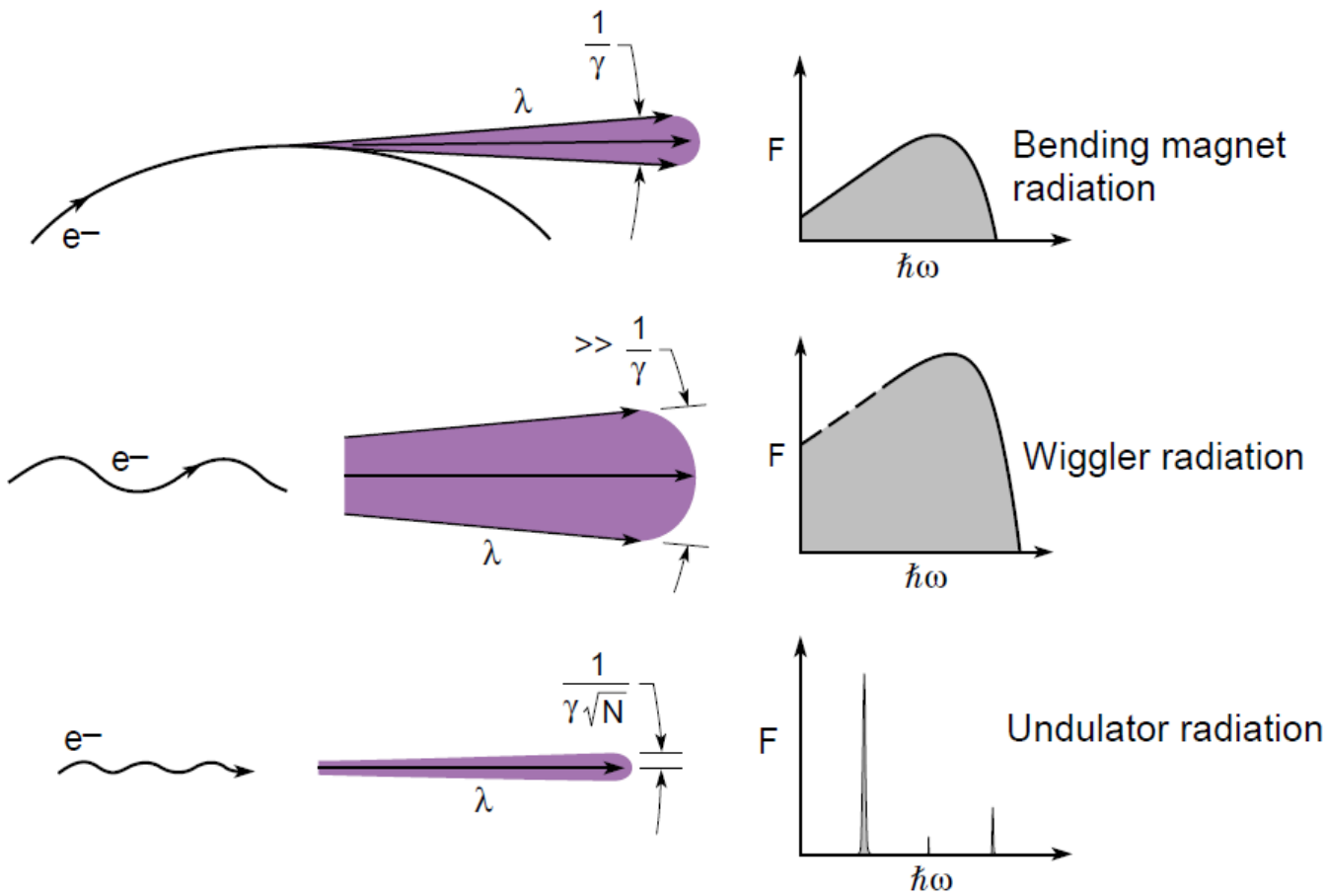

Figure 1.1: Radiation occurs when a relativistic particle, here electron for instance, travels in a uniform magnetic field. It is pointed tangentially outward in a narrow cone [17]

as a narrow cone tangent to the path of the particle as seen in Figure 1.1. The electrons may be further accelerated at higher energies by using radiofrequency electric fields. When these particles reach the expected energy, they are in quasi-stationary situation. They are forced to follow circular paths by a magnetic field and consequently they loose during each turn a fraction of their energy by emitting synchrotron radiation [18].

For third generation synchrotrons, there are generally three types of magnetic structures used to produce synchrotron ligth: bending magnets, and insertion devices such as undulators and wigglers. Bending magnets creates a single curved trajectory characterised by a sweeping "searchligh", which is a general manifestation of radiation generated from accelerating particles travelling in relativistic speeds. A particle that encounters radial acceleration as it traverses a circular path emits radiation through a broad angular pattern as observed in its frame of reference. Due to Lorentz transformation, the angular pattern is compressed from the moving particle's frame to the laboratory frame[19]. The angular distribution of the generated light is towards the forward direction, and the Lorentz contraction factor, γ, is expressed in terms of the energy of the electron E_e and the electron rest energy, mc^2 [11]. That is,

$$\gamma = \frac{E_e}{mc^2}, \tag{1.1}$$

and the emission cone narrows with the increase in energy. The white light from a bending magnet is characterised by a critical energy ε_c, which divides the power spectrum into two equal parts [20]. This critical energy rises with E_e and inversely with the curvature of the trajectory.

Inserion devices are periodic magnetic structures installed in the straight sections of the storage ring. Their primary role is to increase the spectral brilliance with respect to what is achievable with bending magnets. Electron bunch allowed to travel in periodic magnet structures "wiggle" or oscillate at an angle.

A deflection parameter, K, for the electron e, may characterised as a function of the magnetic field stregnth and can be defined as

$$K \equiv \frac{eB_0\lambda_u}{2\pi mc}, \tag{1.2}$$

where B_0 is the magnetic field strength, λ_u is the period of the magnet, m is the particle mass and c is the speed of light. We can also say that

$$K \backsimeq \gamma|\theta_e|, \tag{1.3}$$

where θ_e is the excursion angle. For strong fields as in the case of wigglers, the transverse oscillations are huge and the angle of the trajectory is larger than the emission radiation, or $K \gg 1$. For medium to modereately low field strengths as for undulators, $K \leq 1$. The electron's angular width is small relative to the natural radiation width. The wavelength of the produced light is much smaller than the period of the magnet due to Lorentz contraction and relativistic Doppler shift by a factor of $2\gamma^2$. The radiation cone has an emission solid angle reduced by 1/N of oscillation periods that highly affect brightness and coherence of the synchrotron beam. There is interference between the radiation emitted by the same electron at different points along the path on this narrow angular distribution producung sharp energy peaks. The spectrum of the photon is given by the harmonic wavelengths that is proportional to the square of the energy of the electron and inversely to the period length of he magnet. The angular distribution θ_{cen}, of the *n-th* harmonic is condensed in the narrow cone, and its half width is given by [19]

$$\theta_{cen} \approx \frac{1}{\gamma}\frac{1}{\sqrt{N}}, \tag{1.4}$$

which is smaller than the emission cone, $1/\gamma$, of a bending magnet by the square root of the number of poles, N. This narrow distribution and the N dependence explains why a high spectral brillliance is achievable with undulators over bending magnets and and wigglers.

Fourth generation synchrotron facilities capable of providing highly brilliant light have also started to peaking up the past 10 years. Free electron lasers they are called, these powerful sources also have the ability to provide XUV to the hard X-ray photons. XFEL in DESY [21] and LCLS at Stanford [22] operate on self amplification of spontaneous emission, SASE while FERMI@Elettra in Italy [23] and the future Swiss-FEL [24] are based on seeding methods. Both techniques can produce light that share the same optical properties of conventional lasers such as coherence in a wide frequency range that is widely tunable. The brilliance of the radiation produced from these sources are quasi-monochromatic, but several orders of magnitude higher compared to third generation sources, and offers good prospects to user communities. Details on the operation of these sources are not described here and the reader is referred to [21, 22, 23, 24].

1.1.2 Properties of Synchrotron Radiation

Synchrotron light is attarctive to many scientific communities as it gives the opportunity to study matter in micro and macro scale because of its high brilliance. At Elettra, bending magnets and insertion devices are available, making it feasible to perform studies in a wide array of disciplines.

The impotrant highlights of synchrotron radiation are outlined in the following:

1. **Brilliance.** Also called brightness, it is defined here as the radiated power per unit area per unit solid angle at the source It is generally more convenient to consider various differential fluxes in a small bandwidth around a given energy, hence we use the word *"spectral"* brightness. It is the brightness per unit relative spectral bandwidth. Traditionally in the synchrotron community, it is expressed in terms of photon flux rather than power and finally express the result in 0.1% bandwidth. This parameter finds its relevance where the needed amount of photons is focused to the desired area. In the synchtron regime, typical brilliance ranges from 10^{14} to 10^{20} $photons/s/mrad^2/mm^2/0.01\%bw$. See Figure 1.2. The density of the photon flux in phase-space plays an important role. It may be characterised as the phase-space of the photon flux. Kim [25] showed that the propagation of the photons in an optical medium composing free space and lenses can be easily described by a linear coordinate transformation. The brilliance at the phase-base origin is invariant and thus a true descrisption of the source strength. Taking the integral of the brightness over all angles and positions, one determines the angular density and spatial density of the flux, respectively. The flux may easily derived from the double integral of the brilliance as a function of angle or position.

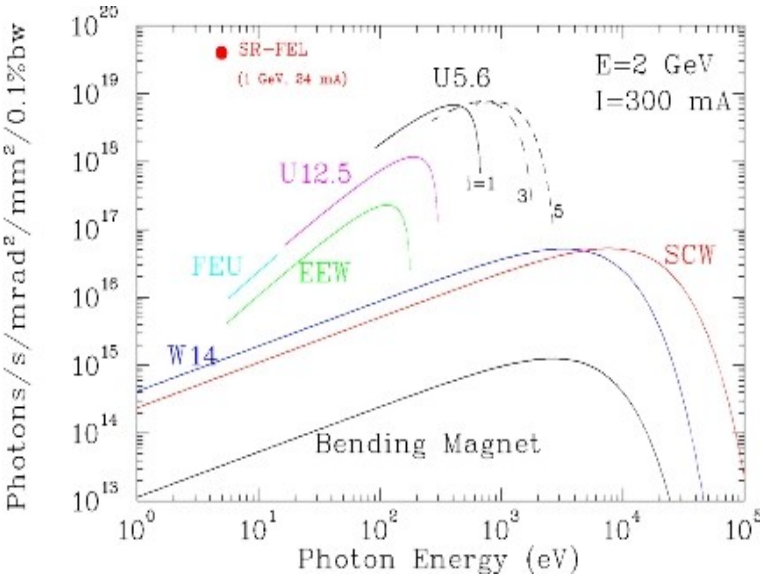

Figure 1.2: Brightness of the synchrotron radiation for various insertion device and bending magnets as a function of photon energy at ELETTRA[28]

2. **Monochromaticity.** Monochromaticity is easily satisfied in synchrotron radiation facilities by using perfect crystal monochromators.

3. **High coherence.** It is the degree to which the radiation can exhibit interference patterns [25]. This is achieved because of the small size of the sources and they are given by the transverse size of the electron beam and the narrow emission cone of the photon. Temporal coherence condition, *ie* $\frac{\Delta\lambda}{\lambda} \ll 1$, is usually a strong requirement of analyzer-based imaging techniques. On the other hand, spatial coherence is much more imposed by propagation-based imaging. The degree of coherence is related to the lateral (transverse) length that is described by the source-to-object distance and the source dimensions. The long and source-to-object distance in combination with the small dimensions of the source leads to highly coherent beam that has been taken advantage by experiements using phase sensitive techniques [26, 27]. Our bending magnet at the SYRMEP beamline measures 0.135 mm x 0.080 mm [10].

4. **Narrow emmission angle** The narrow cone emitted from the magnetic sources, as described previous in the previous subsection, does not exceed $\frac{1}{\gamma}$ for bending magnets and further reduced by $\frac{1}{N}$. It acts as a natural collimation, adds to the intensity of the synchrotron light. In the case of SYRMEP, the horizontal beam divergence is 7 mrad [10].

5. **Polarization of Radiation.** Synchrotron radiation produced by bending magnet, wiggler and undulator sources are linearly polarised in the plane of orbit. This property meets some of the demands of experiments involving magnetic scattering and magnetic dichroism. One may use single crystals of C or Si or phase retarding optics [20] to convert linearly polarised beams to circularly polarised radiation that is demanded by spin-resolved experiments [29].

6. **Time structure.** The electron beam in the sorage ring is not a continuous stream, but rather a highly modulated density funtion of axial bunches that are dictated by the a radiofrequency used to restore power to electrons. Therefore, it consists of light and dark pulses that is useful for time-resolved experiements. Each bunch decays over time as it travels along the the storage ring.

7. **Top-up mode.** When Elettra delivered its first beam to the users in 1993, it operated in the ramping and decay mode. Its injector was providing 1 GeV to the storage ring that were futher accelerated, *ramping* the storage ring to its full operational energy of 2.0/2.4 GeV. In 2007, it comissioned a full energy electron injector and full energy booster that led to the implementtaion of *top-up mode* three

years later [30]. Today, it is becoming the standard mode of operation in most of the advanced third generation light sources. The basic goal of *top-up* is to provide practically a constant beam intensity in the storage ring. The method is to define a beam current threshold (300 mA in Elettra) and a dead band (1 mA for instance) and then control the whole injection and extraction process. To achieve this, a precise timing system but flexible control must be implemented [31]. In broad terms, this modality leads to a better quality of beam for some users and better experimental results.

1.1.3 The SYRMEP beamline

SYRMEP is one of the beamlines of Elettra that is equipped with a bending magnet. The structure is divided into three sections, in the following sequence from the storage ring: the optical hutch, the experiemntal hutch and the clinical hutch and is lay-out is summarized in Figure 1.3. Since the magnetic source still emits a polychromatic beam, its optical hutch has been equipped with a double Si (1,1,1) monochromator crystal to produce monochromatic light. These crystals cover the beam's horizontal divergence of $7rad$ [10]. The desired energy is set by tilting the crystals with high precision motors according to the Bragg configuration and the second crystal can be further translated with respect to the first in order to obtain the the same position across all useful energies. At SYRMEP, the photon energy may be tuned to 8-35 keV range.

1. **The optical hutch.** The first section is separated by a Berylium window with the rest of the set-up. A series of thin Aluminum filters are installed in front of this window, giving the users the opportunity to vary the intensity of the monochromatic beam according to their needs. Air-slit systems are provided in front of the filters, ultimately to shape the beam to reduce scattered radiation originating from the precedent parts of the chain.

2. **The experimental hutch.** The experimental room is the second section of the beamline and it is positioned 23 m away from the source. It is equipped with high precision motors to move the samples and detectors with respect to the stationary beam. The sample holder is a five-axis stage that can be moved for planar and tomographic imaging. It is coupled with a two-axis detector stage mounted to a sliding rail to vary the detector distance, giving the users the possiblity to perform absorption and phase contrast imaging. The photon flux is monitored by customised air-filled ionization chambers positioned prior to the sample position. At 17 keV, photon counts are about 1.6 x $10^8 \frac{ph}{mm^2 s}$ at 2 GeV

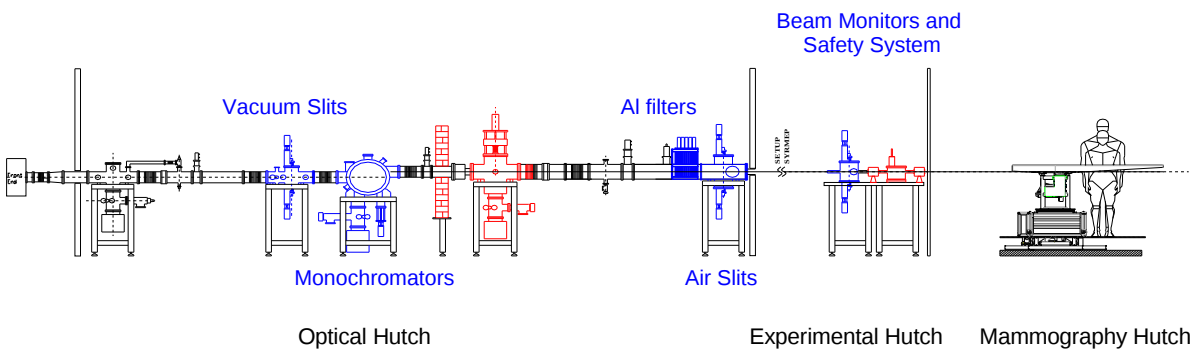

Figure 1.3: The SYRMEP beamline. The beamline is divided into three important sections: the oprical hutch, the experimental hutch and the mammography hutch.

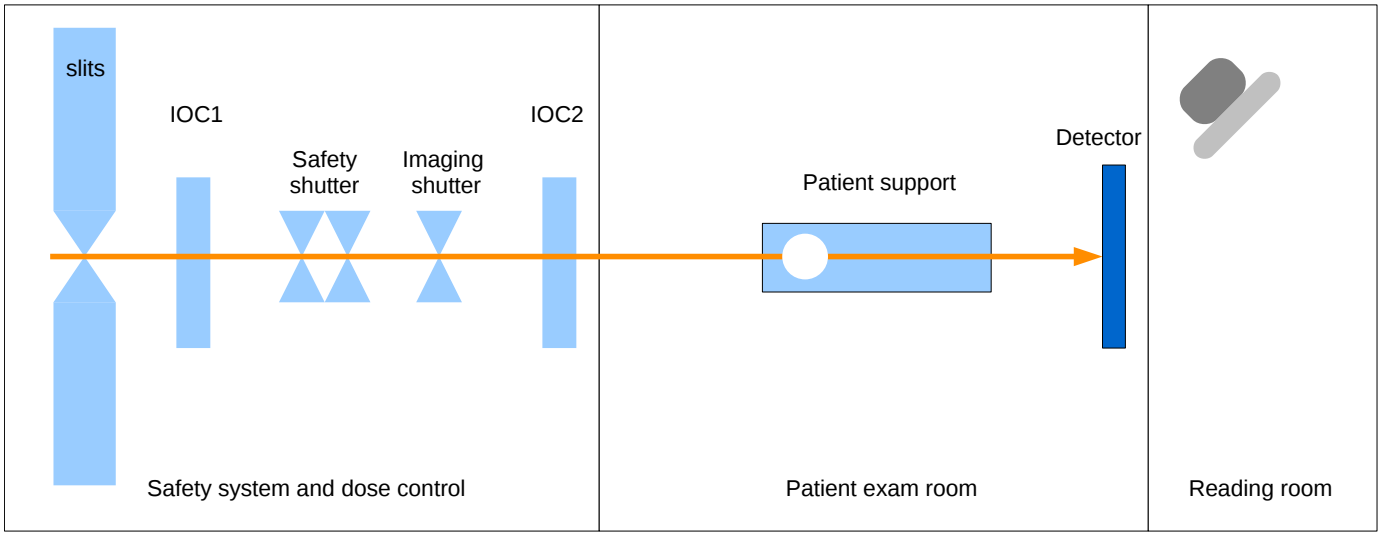

Figure 1.4: The layout of the mammography station of the SYRMEP beamline

electron energy and 300 mA electron curent operation while 5.9 x $10^8 \frac{ph}{mm^2 s}$ 2.4 GeV electron energy and 140 mA electron current operation [8].

3. **The mammography station** The end station of SYRMEP beamline is the facility dedicated to clinical mammography studies now operating with the use of phase-contrast imaging techniques. It is mainly composed of a patient examination room and a radiologist room plus a safety and dose control system. The layout of the station is presented in Figure 1.4. The beam dimensions at this station are defined by fixed vertical 3 mm aperture and a motorised slit with absolute encoders that delimimits the width of the beam. At the breast position, the beam cross-section measures about 3.4 mm x 210 mm.

   (a) **Security and dose control**
   In order to ensure safety to the patient, a safety and dose control system positioned at the nearby experimental room monitor the beam prior to its entry into the patient room. Shutters allow entry of the beam only when the patient is on position for examination. The transmission type, air-filled ionization chambers, calibrated againts a secondary standard chamber from the Italian Istituto Nazionale di Metrologia delle Radiazioni Ionizzanti of ENEA (INMRI-ENEA) [32], are meant to do continous monitoring of the beam. Also, the dose received by the patient at the breast position is estimated from the read-out of these instruments. The system also has system shutters. They halt the entire procedure in case beam, bed and/or radiation safety parameters are not met.

   (b) **Patient support and allignment**
   The patient support and scanning system for the patient consists of an ergonomically designed bed where the patient lies in prone position during the examination with breast pendulously hanging in a hole with a size consistent with the chest anatomy (Figure 1.5). Underneath is a breast compressor that works similarly as conventional compressors that aims to equalize the tickness and stretch the breast tissue. The compression paddles are motorised, and also has the possibility to be positioned manually. The breast and the compression system is 30 m away from the source.

   (c) **Detector holder**
   The first clinical mammography run with synchrotron radiation initiated by the SYRMEP collaboration in 2006 [33] used a commercial film screen system that was positioned 2 m away from the breast compressor in able to achieve phase contrast effects. The holder of the film casette moves simultaneously with the support system and the patient as the breast is scanned againts

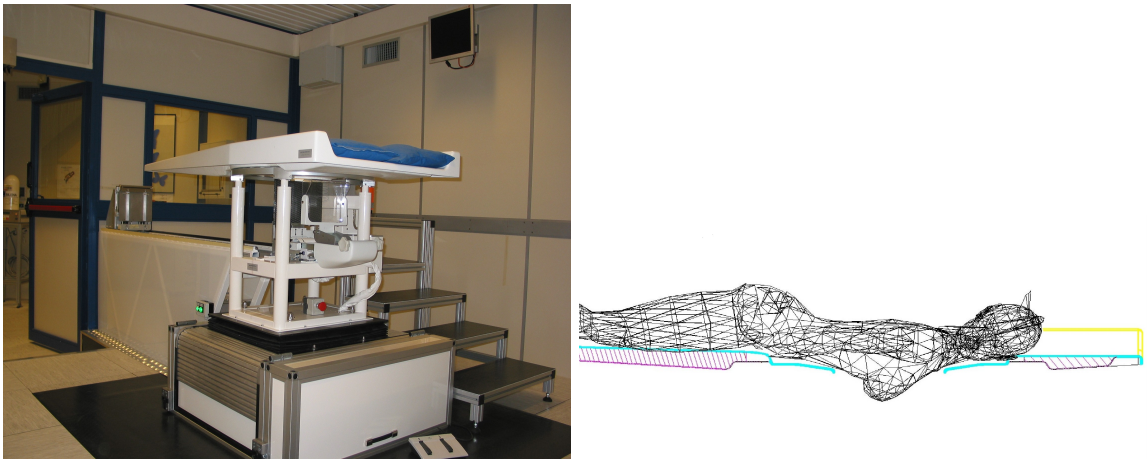

(a) SYRMEP patient support (b) Patient position during examination

Figure 1.5: The patient support system. On the left, the motorised patient bed is presented while on the right the image shows the patient position during the procedure. The patient lies prone with breast hangs pendulously while the motor of the bed moves vertically.

the stationary beam to produce a planar image. It also houses an array of four photodiodes that are used to determine the exposure parameters through a short low-dose pre-scan. The breast attenuation is determined by the thickness provided by the compressor by comparing the signal from the ionization chambers mentioned in the security and dose control section and the diodes embedded in the detector holder. Today a second phase of this clinical study is being undertaken with the use of photostimulated plates as the receptor, and the same holder is being utilised to image the patient.

(d) **Radiologist room** At the end of the mammography station, a room is dedicated to the radiologist who is assigned to make a clinical score on the images is provided. It is also the same room where the initial instructions are givien to the patient prior the administration of the the diagnostic procedure using synchrotron radiation.

A full technical presentation of the clinical facility as well as its fail-safe system is presented in more detail in [34, 35].

1.2 Perspective

For what concerns the SYRMEP mammography project, the monochromatic beam with synchrotron radiation and the design of the beamline makes a good method to perform phase-contrast imaging. Particularly, these allows the enhancement of image quality by application of innovative techniques in order to observe radiation phase-shift after traversing the object that is being imaged. In line with these aims, a digital detector was developed to complement these efforts.

Chapter 2

Silicon Detectors and Photon Counting Systems

2.1 Fundamental properties of Semiconductors

Semiconductors are characterised by a small gap between the electronic band the conduction band. For silicon, an electron needs only an excitation energy of $E_g = 1.12\ eV$ to bring it from the valence band to the conduction band. This leap of the electrons from the valence to the conduction band generates holes moving into the valence band in an opposite direction to that of the movement electrons in the conduction band. As a consequence a current of holes is generated in the valence band and a current of electrons is generated in the conduction band. Charges and holes flowing in a semiconductor that is under the influence of an electric field , E, gain a velocity v given by

$$v_e = \mu_e E, \tag{2.1}$$

for the moving charge and

$$v_h = \mu_h E, \tag{2.2}$$

for the hole. μ_e and μ_h is the mobility of the electron and hole respectively, that defines the current. At a given temperature T, electon mobility is greater than hole mobility because the effective mass of electrons is less compared to holes [36]. For n electrons and h holes, a current density J_c, may be decribed by

$$J_c = e(n\mu_e + h\mu_h)E \tag{2.3}$$

where e is the electronic charge. We also say that $J{=}\sigma E$, where σ is the conductivity and gives the relation

$$\sigma = e(n\mu_e + h\mu_h) \tag{2.4}$$

and the resistivity may derived just by taking its inverse.

2.1.1 The PN Juction

Pure semiconductors have equal number amounts of electrons and holes in the conduction band. Introducing a small amount of donor or acceptor impurities to intrinsic semiconductors modulates its electrical properties. These impurities integrate themselves into the crystal lattice resulting to n-type and p-type conductors, resulting from the introduction of electrically active donor and acceptor impurity atoms, respectively. In n-type material, there are electron energy levels near the top of the band gap so that they can be easily excited into the conduction band. In p-type material, extra holes in the band gap allow excitation of valence band electrons, leaving mobile holes in the valence band. Semiconductors doped with donors have excess electrons as carriers while excess holes if doped with acceptors.

A pn-junction is created when the n-type semiconductor and the p-type semiconductor are put into abutment (Figure 2.1a). This junction may be abrupt if the passage from the n-type layer to the p-type layer is just a step, else the junction is linearly degraded if the passage is through a gradual change in doping

density. It is formed from the diffusion of acceptors to the n-type or donors to the p-type region caused by the difference in the Fermi levels of these two layers. The diffusion is created by a space charge with two zones, a first zone of non-zero electric charge, made of filled electron acceptor sites not compensated by holes and a second zone, again of non-zero electric charge made of positively charged empty donor sites not compensated by electrons (Figure 2.1b). The space charge is a consequence of this is the *"depletion region"*. It has a property of having devoid of mobile charge carriers. The charge distribution generates an "in-house" electric field hence a reference V_o, known as the *contact potential* is defined. For Silicon, it is 0.3 to 0.6 V at T=300 K [37].

Charges passing through the region is swept by the field inside the region (Figure 2.1) and if the distribution of the charge density $\rho(x)$ is known, the width of the depletion zone may be easily determined from

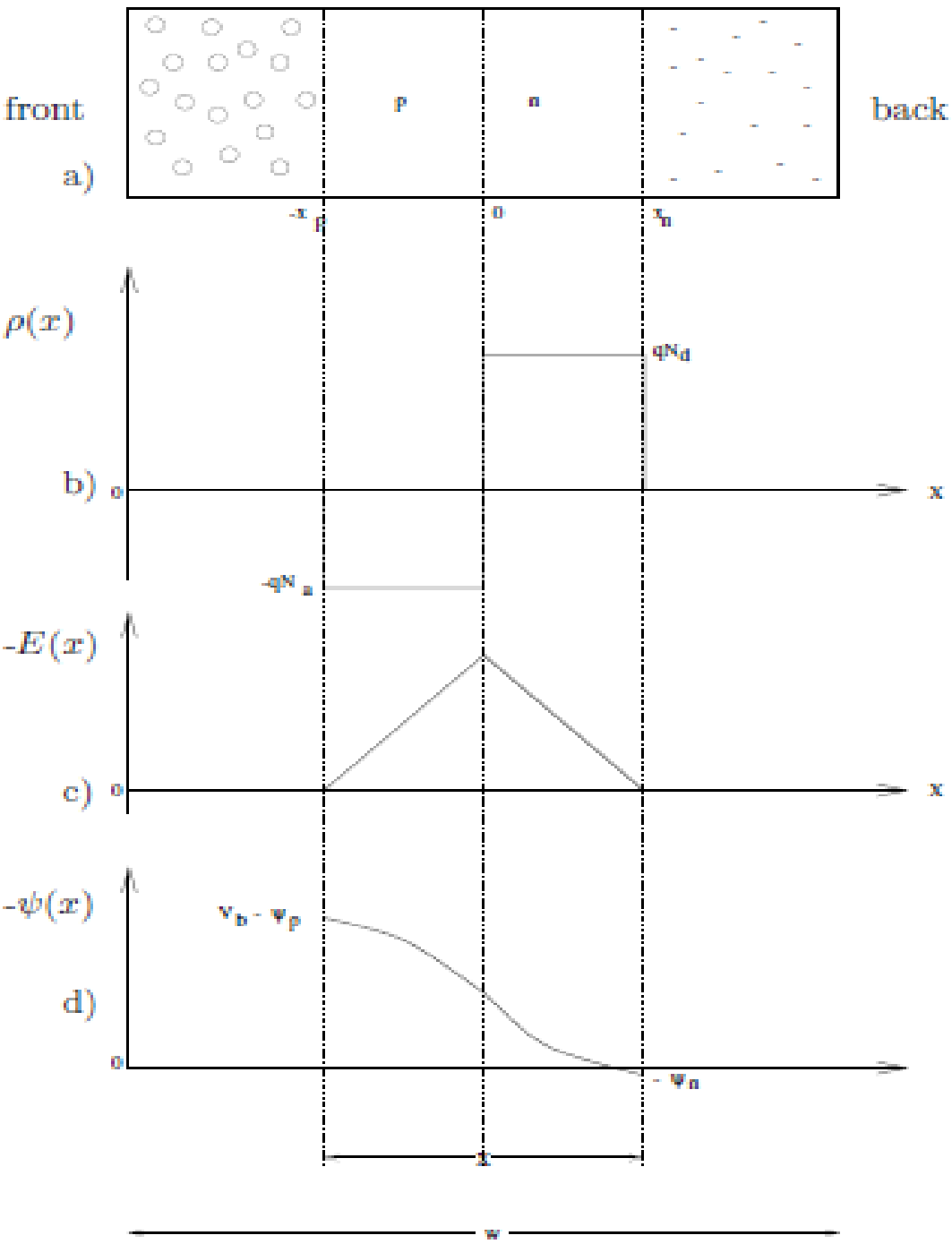

Figure 2.1: Schematic reperentation of an unpolzarised pn-junction of thickness w [37].

the Poissonian equation

$$\frac{d\Psi^2}{dx^2} = -\frac{\rho(x)}{\varepsilon}, \tag{2.5}$$

and is presented in Figure 2.1d. Here, ε is the dielectric constant.

The depletion depth may be varied by inducing an external potential to the sides of the junction. If the applied potential is higher at the p-type side, the depletion region size shrinks and its behavior is like that of a conductor. This case called direct biasing. If the vias voltage were reversed, the depletion region increases. Potential difference becomes the sum of the contact potential and the applied reverse bias, V_b its square-root is proportinal to the depletion depth. The depletion layer is also described by some capacitance, which is proportional to the depth and inversely with V_b.

2.2 Silicon Microstrip Detectors

The strength of Silicon detectors over other detectors is the small average energy required to produce ionization, *ie.*, ion-hole pair. For Si, the required energy is only 3.6 eV. They also offer good spatial resolution so far achieved in large detector systems which has been one of their principal attraction to physicists for instance, who have been devising experiments to search for, and measure the properties of the rare decays of short lived exotic particles [38, 39].

It has encouraged ingenious and creative individuals to conceive novel and complex devices, and the fast and progressive development has stimulated interest in the possible advancement by exploiting the good characteristics of Si, one of them are microstrip sensors. Microstrip sensors are extensively used in many areas from very large scale research like the ATLAS tracker [40], to intermediate scale research like powder diffraction [41] and to the more tangible application like tomography research in medical physics [42]. Here in Trieste, Italy, several generations of detectors of this kind has been studied for mammography research [43, 45, 44].

2.2.1 Silicon Microstrip Structure

This section reviews the general properties of silicon trip detectors as they are typically made today. The characteristics they carry provide boundary conditions imposed by physicists and detector manufacturers that should be considered in the design. A schematic of the cross-section of a Silicon microstrip sensor is depicted in Figure 2.2

Si microstrip sensors are fabricated based on a few hundred microns thick high resistivity wafers, usually 5-10 kΩ-cm. Its active volume has the strips on the front side, confined by a guard ring structure that secures it from leakage currents from imperfect cut at the edge of the detector. Each of the strips forms a reversed biased diode with the sensor backplane and they detect radiation interactions in the volume.

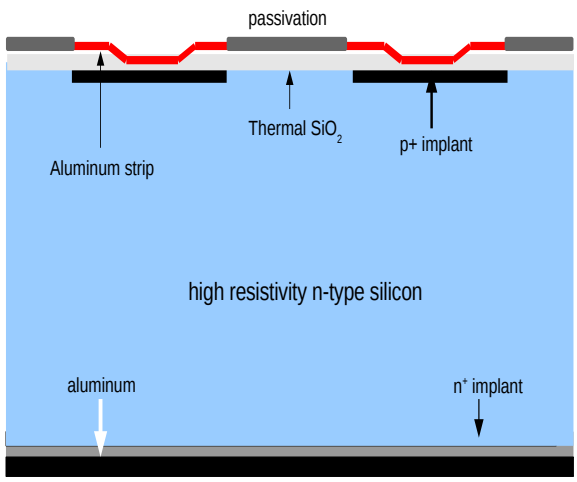

Figure 2.2: Cross-section of a normal to the back-plane of a Silicon microstrip detector. A passivation layer is usually put to add extra-protection to the bulk.

The strips and the guard rings are near ground potential while the back electrode is usually kept at high voltage to sufficiently achieve full depletion so that the detector is active in the entire thickness. Therefore, the detector gathers the holes on the strips and electrons on the backside. The backside consists a thin Aluminum layer over an n^+ phosphor-doped layer in the Silicon. The n^+ layer takes off harmful impurities during fabrication. These imperfections create deep-energy states near the center of the band gap that will generate leakage current.

The face of the sensor consists of thin strips of Aluminum with diffused p^+ implants. Both are in direct contact for a DC-coupled detector while separated by an insulator for an AC-coupled detector. The front-side area is covered with SiO_2 with contact holes for the Aluminum strips. The detector may be further added with a passivation layer above the oxide to increase protection. One strip has a bond pad where a very fine wire is connected to an individual channel of the read-out chip.

2.2.2 Noise Sources in Microstrip Systems

In any physical system, measurable quantities come with unavoidable fluctuations due to discrete nature of matter, the quantity itself or randomness of the process. These fluctuation take the name *"noise"*, a property of the system that can be estimated or measured. In microstrip detectors, the noise come mainly from *"white"* noise that do not depend on frequency and will be summarized in the following:

1. **Shot Noise.** Noise of this type is a result of the discrete nature of electric charge and it represents the statistical fluctuation in the number of charge carriers [46]. Charges may flow from the juction as a form of leakage current in the detector [47]. Imperfections in the fabrication technology employed on the sensor as noted in the so-called "panettone effect", where low current at the first and last few stips are noted, and high current in the strips in between. It could be that high generation rate are present at the surface due to stress as a consequence of simultaneous presence of certain nitrides and oxides; or the low current suggest a problem in the strips in very close proximity to the bias ring [48]. Maintaining a low leakage current is a key point in microstrip detectors in order to achieve a good signal to noise ratio. Hole diffuion from the undepleted volume increases the current and degrades the signal. An appropreate bias voltage may help address this, at it affects the size of the depleted volume [49].

   Imperfections in the bulk also provides unwanted noise. Bulk damage has two effects: a change in the effective carrier density causing the depeltion voltage to change and an increase in the leakage current due to the creation of deep traps which enhance the the generation of current [50].

2. **Thermal Noise.** The basic reason for this noise is the thermal fluctuations of the electron distribution in the conductor [46]. This phenomenon is referenced back in 1928 on Johnson's work on thermal motion on electric charges in a conductor[51] and at the same year with Nyquist's derivation of noise properties on the basis of the second law of thermodynamics [52]. The noise voltage power spectral density is flat, and is proportional to the effective resistance (to the amplifier) [53].

3. **Series Noise.** Ultimately, the largest source of noise is dominated by the strip capacitance and the total resistance. The spectral power density is proportional to the interstip capacitance and to the square-root of the resistance. The noise may be reduced by choosing an appropreate width and/or thickness of aluminum strips bring down the resistance per unit length [47, 54].

2.2.3 Absorption Efficiency

While the overall quantum efficiency of an imaging system is also dependent on the chain of read-out electronics (most heavily in the threshold or discriminator), an important contribution also comes from the sensor on how well it transforms photons to usable signals. For what concerns the sensor, we will now present the absorption efficiency: the fraction of photons that impinges the detector that will generate a detectable pulse on the collecting ends, or the fraction of photons that are absorbed in the active volume of the detector.

When the detector is derived from the silicon wafer, defects near the edge produce unwanted dark current. These currents must not reach the active region of the sensor beacuse they induce noise that completely

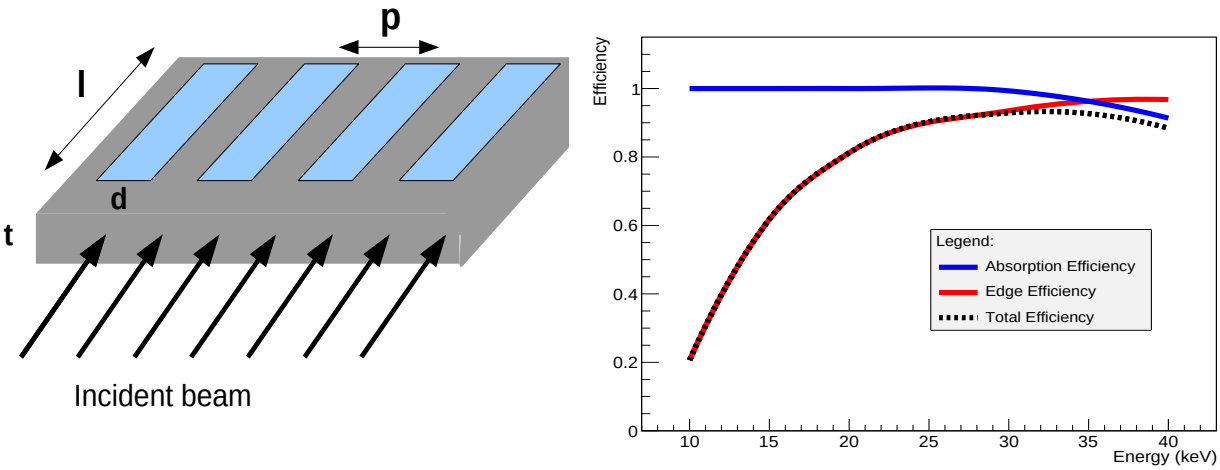

Figure 2.3: Schematic representation of a microstrip sensor on *edge-on* configuration. The strip length is indicated by l and the cutting distance is represented by d. (b) Efficiency of a silicon microstrip sensor with strip length = 1.5 cm with a dead zone depth of 200 microns. Data for absorption length as a function of photon energy was obtained form Ref. [55]

ruin the signals form the photons. Guard ring electrodes similar to the strips are implanted on the front and side edges of the detector to collect leakage current caused by the edge deffects. Moreover it also collects signals form the fraction of photons while traversing the guard structure thereby introducing a dead zone that reduces the efficiency. The edges are frail to radiation damage, and its size must consider the amount of current it is expected to collect on a long term use. To this day in the era of sensor fabrication, a battle remains if edgeless sensors would really benefit detector developers in terms of noise and radiation damage versus a large dead-region in the edges to meet the constrains.

2.2.4 Edge-on Detectors

Edge-on detectors using mircostrip sensors, with schematic shown in Fugure 2.3, were proposed by the SYRMEP collaboration in the 1990s for imaging research. In this configuration, the sensor is irradiated in the longtitudinal direction, parallel to the readout strips. The pitch, p, defines the pixel size in one direction, while the thickness t, determines the pixel size in the other direction. For radiological examinations with photons, a high effiency is a requirement imposing several millimeters of sensor for absorption. Edge-on orientation removes practically any limitation on the absorption efficiency, as the full length, l, of the strip absorbs almost completely the interacting photons resulting to a reduced dosed to the patient. One limitation of this system is the existence of a dead reagion, d, that brings down the efficiency because photons in this region are not counted. This cutting distance is often necessary to reduce leakage current [56] and moreover may still be improved with various sensor fabrication techniques [57, 58, 59, 60, 61].

Apart from SYRMEP, several experiments have tried to exploit this property for medicial imaging applications. A collaboration in Korea [62] uses Si microstrip sensors that is 0.095 mm wide, 0.5 mm high and 10 mm long positioned in *edge-on* geometry with a tilting angle of 5 degrees to the normal direction of the incident beam. This configuration results to a 5.7 mm absorption depth. In this way, one tries to evade the dead zone to improve the absorption efficiency. Similarly in a collaboration in Stockholm, Sweden [63], the sensor is oriented almost *edge-on* to maximise the efficiency. Their system uses a fan-beam source with the incident beam entering the sensor just after the guard ring. In the initial phase of their study, the collaboration was able to show that the guard rings increases the effective width of the dead layer which futher brings down the number of photons registered [64]. Thier current system's Silicon detector thickness is 500 μm, with the strips pointing back to the x-ray source. With this configuration, the attenuation length of the x-rays is 3.6 mm. This techique is particularly useful for systems employing X-ray tubes with polychromatic sources where one side of the tail of the spectrum is low-energy. With optimisation of the sensor angle, the efficiency is about 92 % at 28 kVp.

Silicon microstrips of 100 μm pitch and length of 10 mm on *edge-on* design based on RX64 readout [65]

was also tested with angiographic test objects [66] using a conventional hospital iodate contrast medium (usually 370 mg/ml) using 31 and 35 keV settings of the beam taken separately. The final image was obtained by taking a pixel by pixel logarithmic subtraction of the images obtained at the two energies.

Chapter 3

The PICASSO detector

The PICASSO (Phase Imaging for Clinical Application with Silicon detector and Synchrotron radiatiOn) project, funded by the Istituto Nazionale di Fisica Nucleare, aimed to contribute to the needs of the mammography project now running at the SYRMEP beamline at Elettra. One of its fundamental aims is to provide a digital detector, tailored to address the demanding requirements of the clinical study. It is intended to be used with synchrotron beam with unique features that allows phase-contrast imaging. This modality relies not only on the source and set-up characteristics, but also detectors that are fast that can provide high spatial resolution. This project is an evolution of the INFN MATISSE project, in collaboration with the Detector Group of the Swiss Light Source [44].

3.1 The Detector

The detector is based on silicon microstrip sensors manufactured by Hamamatsu (Hamamatsu Photonics KK, Hamamatsu City Japan) on high resistivity wafers. It has a strip pitch 50 μm and has a thickness of 300 μm. The strip length varies from 15 mm and 20mm. The sensor widths used in this study was 2cm, 9 cm, and 12 cm. Since the width of the beam is 21 cm at the detector position, the sensors were tiled in such a way that the either 9cm plus 12cm Silicon sensors, or 9cm plus 9cm plus 2cm Silicon sensors are in abutment to accomodate the active area needed at the detector region at the mammography hutch. The assembly will compose of stacks of detectors which we will call *layers*, and the lay-out of one layer is exemplified in Figure 3.1.

The beam geometry at the SYRMEP beamline is thin and laminar so that the detector is oriented *edge-on* configuration. That is, the strips are oriented parallel to the incoming beam. The main advantage of X-ray side illumination is the capability of almost 100% X-ray absorption. The PICASSO detector has been designed so that the undepleted region at the entrance window of the sensors is minimum. The detector was operated at full depeletion at 120 V. The sensors has a guard ring only on the three sides. The cutting edge is 200 microns from the guard ring.

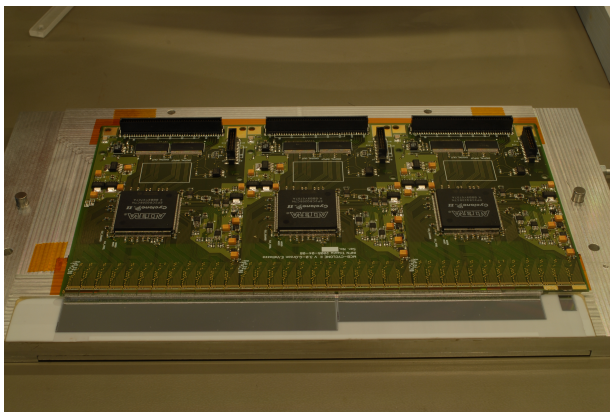

Figure 3.1: Layer configuration of the PICASSO detector

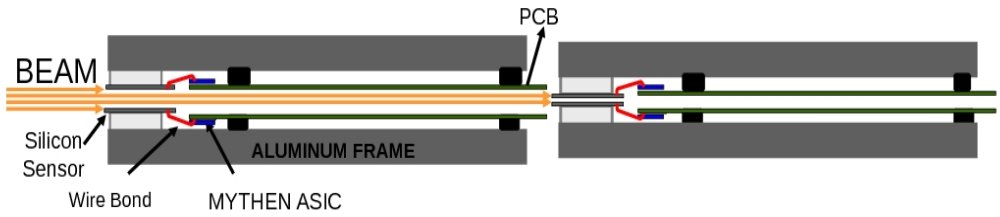

(a)

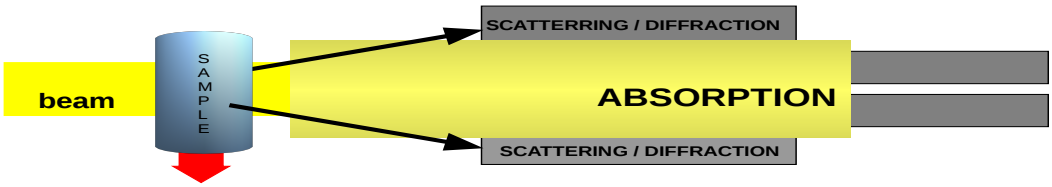

(b)

Figure 3.2: (a) Schematic representation of the arrangement of the PICASSO detector. (b) The versatile detector configuration permits several experiments apart from phase-contrast imaging such as absorption, scattering and diffaction studies

The detector in its final configuration is composed of four layers containing three modules each. These layers are arranged so that two layers comprises one couple of detector, with which two couples are separated along the beam propagation. A schematic picture is given in Figure 3.2a. The sensors in the front detector couple is separated in parallel by $0.8mm$ while its back detector sensor counterpart is separated by $0.1mm$. Part of the beam that travels through the front detector reaches the back detector. This design efficiently allows absorption, as well as scatting and/or diffaction imaging studies (Figure 3.2b).

The detector is held by a mechanical frame based on Aluminum which holds both the printed circuit boards and the Silicon microstrip sensors. To ensure planarity, the sensors are mounted further in a glassbar support, also held by the Aluminum frame support [44]. Figure 3.3 shows the mechanical support structure for two layers of the detector.

In the very preliminary version of the readout system of the Picasso detector, a VME-based electronics

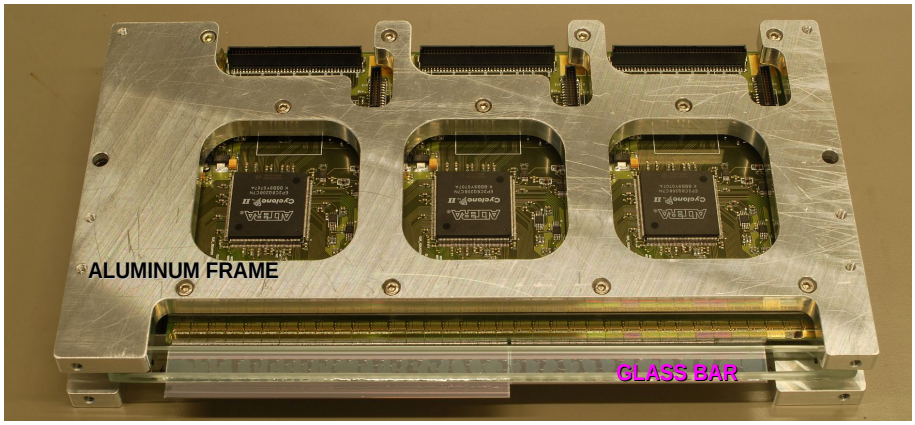

Figure 3.3: Mechanical support for the detector. The printed circuit boards are fixed into Aluminum frames for support. The sensors glued to glassbars not only to reinforce the support, as well as maintain planarity along its length.

was used. The system produced very good results in imaging [68], but was challenged with the speed of the acquisition system beween two frames due to the load of data it has to transfer. For this reason, the readout electronics was upgraded to meet the issues on speed. The core of this thesis is focused on the development of a readout system to meet this demanding need of the mammography project of the SYRMEP beamline. The Mythen detector system prototype used for materials science studies [41] however with a controller for 6 modules was adopted. Six modules, a Picasso controller board and acquisition PC forms a stand-alone PICASSO Detector System [69] and is presented in Figure 3.4. The readout developed for the system will be presented in detail, including with the different subsections of its components.

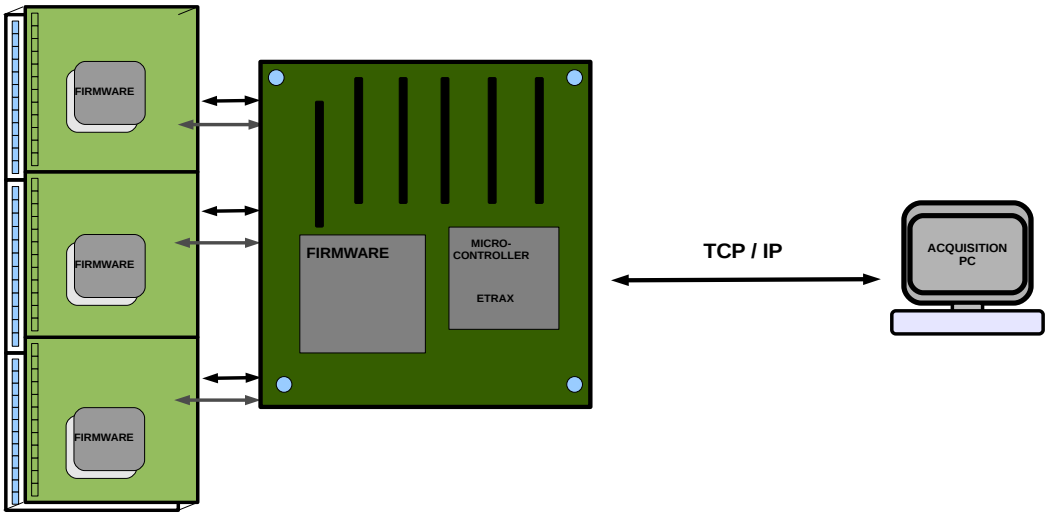

Figure 3.4: The PICASSO-detector stand-alone architecture. It is mainly composed of 6 detector modules and a controller board connected to an acquisition PC via TCP/IP.

3.1.1 MYTHEN-II ASIC

The front-end electronics of the PICASSO detector is based on single photon counting MYTHEN-II (Microstrip sYstem for Time-rEsolved experimeNts) ASIC that was developed at Paul Scherrer Institut, Switzerland mainly for time-resolved powder diffraction experiments [67]. This chip is designed in UMC 0.25μm technology that contains 128 channels at 50μm pitch. Each of the channel of the ASIC is directly wirebonded to the sensor strips. See Figure 3.5.

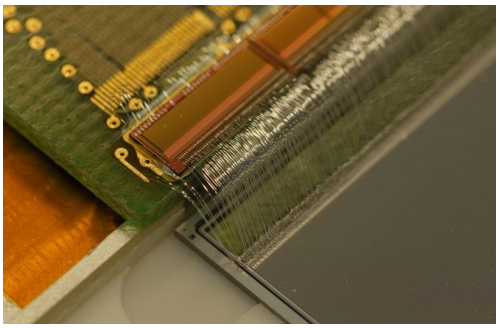

Figure 3.5: The MYTHEN chip and the microstrp sensor connected together with wirebonds.

A schemeatic block of a single channel is shown in Figure 3.6. It consists of a low noise charge-sensitive amplifier that magnifies the analog signal from the detector. The amplifier is AC-coupled to two shaping gain stages with tunable shaping times. The gain is influenced by the shaping parameters and may be

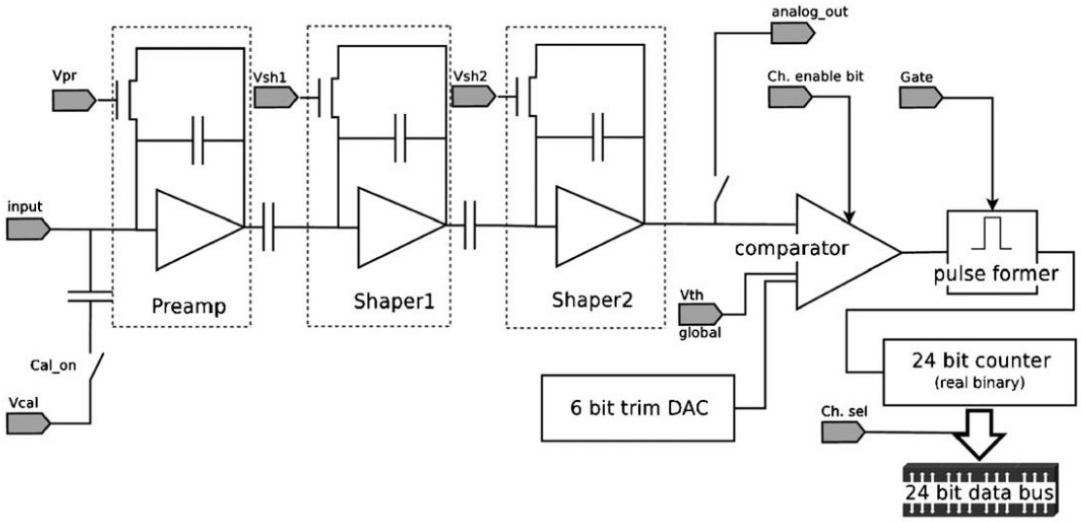

Figure 3.6: MYTHEN II single channel architecture. The principal parts of the chip charge are the sensitive amplifier and shapers that define the input from the detector, a comparator to discriminate signals with amplitude lower than a set reference, and a 24-bit counter enabled by a global gate signal [67].

increased or lowered by tuning the voltages at its feedback transistors to achieve the desired speed and noise levels required. Only the standard setting of the MYTHEN-II chip was used in this work.

The output of the shaping procedure is compared with a defined global threshold in the comparator. Only signals higher than this threshold are counted as photons by the internal 24-bit binary counter, hence the intrinsic noise is rejected. The comparator threshold can also be trimmed on a channel-by-channel basis via an internal 6-bit DAC which adds to the globally adjustable threshold prior to the signal being fed to the counter. Between the comparator and the counter is a gatable pulse former which provides a digital signal to the counter which is activated by a gate signal. This means that the period at which the detector counts is defined by a signal which acts like a shutter.

The control logic allows the retrieval of any bits per channel, nominally set to 16-bit dynamic range which is sufficient for our applications.

The MYTHEN-II ASIC has input lines dedicated to receive pre-amplifier, shaper, comparator, trim and calibration voltages as well as lines to receive signals for clocks, sets and resets, modal signals, plus signals to activate the chip and its channels. Data coming from the detector, once multiplexed may be routed to any of its four output lines with an appropreate modal signal and number of clock cycles. Data transport will be discussed in detail in Section 3.2.1. Figure 3.7 presents the layout of the input and output lines of the chip.

3.2 The PICASSO module

PICASSO has adopted the MYTHEN detector modular system, wherein the read-out is sub-sectioned into modules. The MYTHEN design has 10 MYTHEN-II ASICs, while PICASSO houses 2 more additinal ASICs per board to cover the required active area of the mammography project. Each PICASSO layer has 3 modules tiled together side by side, nominally containing 12 ASICs each. To meet the 21-cm requirement of the mammography set-up at the SYRMEP beamline, removing 3-4 chips in last module of each layer sufficiently covers the required width.

3.2.1 Signals to the readout chip

Each readout chip embedded on the Picasso Circuit Board (PCB) receives signals in two sections: the analog and digital component.

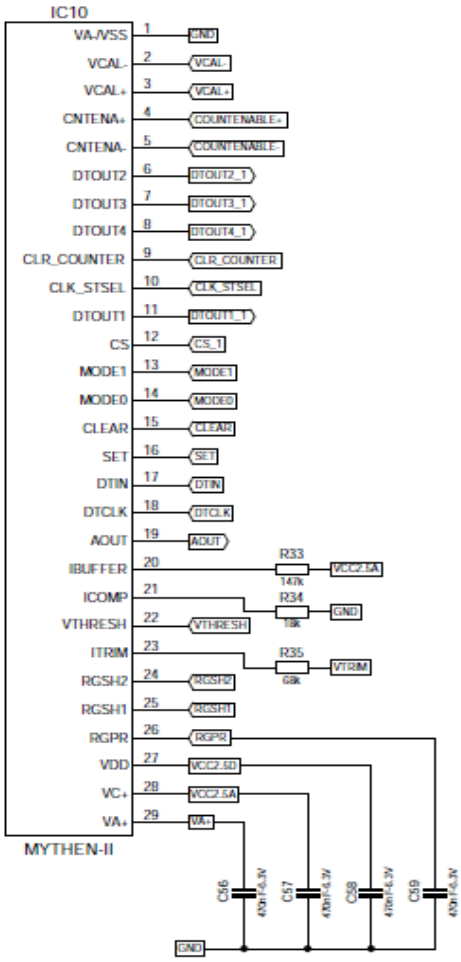

Figure 3.7: The different input and output lines of the MYTHEN-II chips (*drawn by Erik Vallazza).*

The Analog Component

The analog part is further subdivided into two major components: a well-defined power supply for the ASIC and adjustable voltage supplies. Each Mythen-II ASIC is supplied with a 1.1 V analog supply (V_{A+}), 2.5 V ASIC digital supply (V_{DD}) and 2.5 V (V_{C+}) clean for the DAC and comparator. The current drawn by each chip is 2 mA, 3 mA and 15 mA due to the ASIC analog supply, ASIC digital supply, and comparator, respectively.

The adjustable level supplies to the chip are the voltage adjusters to the pre-amplifier V_{Rgpr} feedback, first $V_{Rgsh1}$and second V_{Rgsh2} shaper feedback, comparator voltage V_{thresh} global to all strips bonded to the chip, the calibration pulse V_{cal}, the trim voltage $Vtrim$ (controller for trim) output, the input current to the comparator and the current for the chip buffer controlled by V_c. The amplitude of these signals may be altered to achieve the desired noise or speed.

The Digital Component and the signals to the chip: the firmware to the modules

The input and output signals to the readout chip are highly based on transistor-transistor logic (TTL) programmed via Cyclone II programmable logic device (PLD) from ALTERA [70] coupled with *erasable programmable read only memory* (EPROM) for ease of debugging. The logic was structured with *VHSIC hardware description language* (VHDL). Several registers and counters were created to temporarily store data that are eventually used to set commands in the different blocks of the design. The different components are presented in Figure 3.8. Both the pinout and the logic are managed via 12 control signals. The bits from each chip in the chip_out array is represented by one bit, and the output may be traced from which output line of the chip it originated from.

Each Mythen-II chip in a module is activated via parallel-out shift in register, as depicted in Figure 3.9.

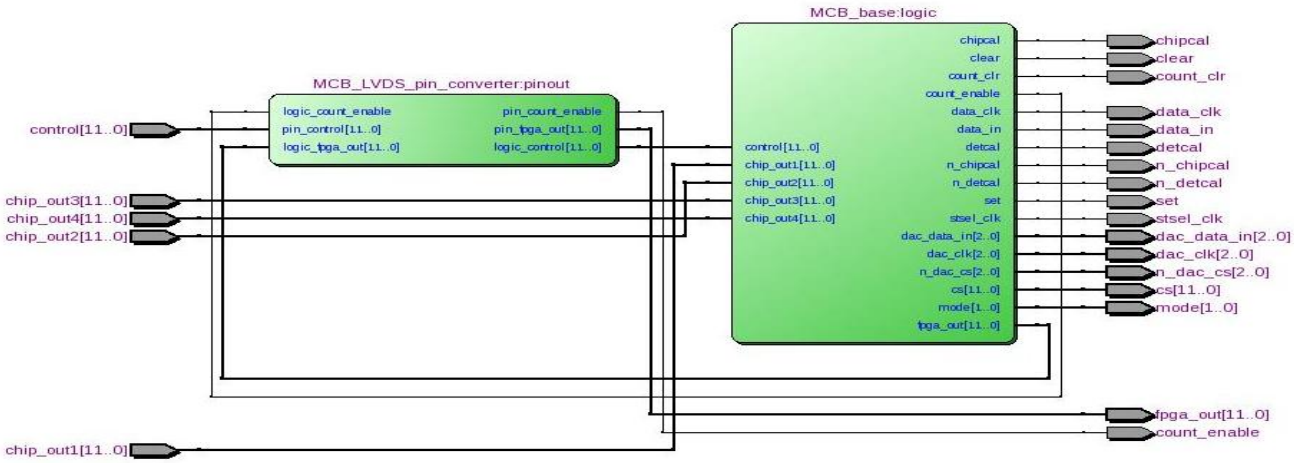

Figure 3.8: The block diagram of the MYTHEN-based detector where the PICASSO firmware was developed.

Once all the bits for each chips are high after 12 clock pulses, all the ASICs are activated.

Only when the chips are selected that the voltage data are routed to the pre-amplifier, shapers, and to the lines for the comparator threshold, trim and calibration pulse. That is, only when the data-in and the data-clock for the digital-to-analog converter (DAC) are on both logical high , the logic of chip is enabled to receive these data.

For the DAC chip feeding the voltage for the global threshold and the trim , the data is transfered to the ASIC only when the clock is high. In Figure 3.10 as an example, the data for the trim and the threshold are set by the *dac_cs* signal instantenously. The same is true for the upload of the calibration and pre-amplifier data, as well as *shaper1* and *shaper2* data. Initialization of the DAC may be done only once until a reset is called, making the user load less parameters, hence a faster acquisition.

The calibration pulse is routed to the the detector or to the chip via a counter. Once counter output is released, the calibration pulse to the detector is given with one clock pulse, else instead the calibration pulse to the chip is called. See Figure 3.11

One of the important things successfuly implemented in this design was availability to the user an increased flexibility in terms of the dynamic range. It permits a limited readout per channel and 4, 8, 16 or 24 bits may be chosen. This is achieved by setting a mode signal to a multiplexer that selects which data bits are routed in the data output pads, *DTOUT*, as presented in Figure 3.7. The module has 34-bit input shift register, of which bits 20 to 23 are used to achieve the purpose described.

As shown in Figure 3.12, the parallel output from this shift register may be altered so that the one can readout a limited number of bits with a combination of reduced number of clock cycles in the input shift regiter. For a 24-bit readout, bits 20 to 23 of the shiftin register must be set to 0001 for 24-bit readout, 16-bit readout to 0100, 8-bit readout to 0100 and 4-bit readout to 1000 before clearing the contents of the

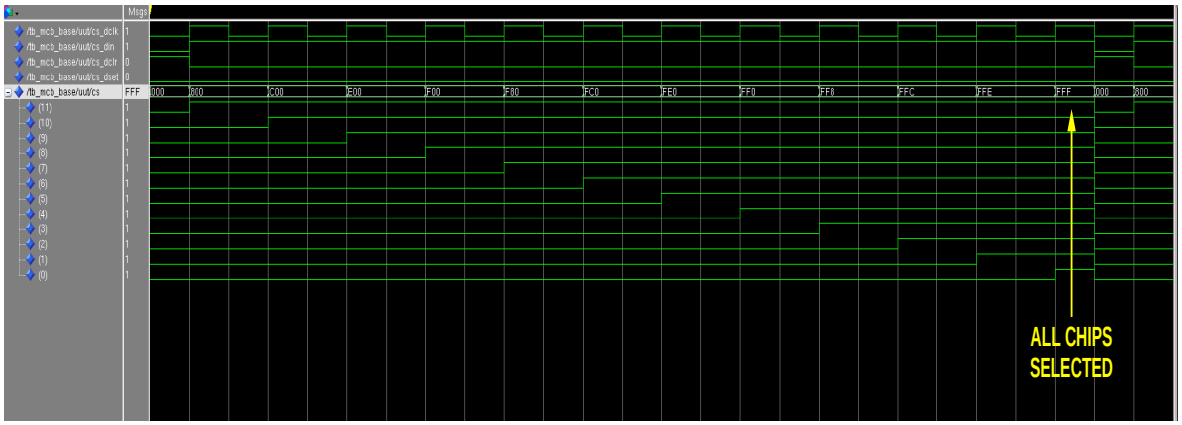

Figure 3.9: The chips in each module are activated via a parallel out shift register.

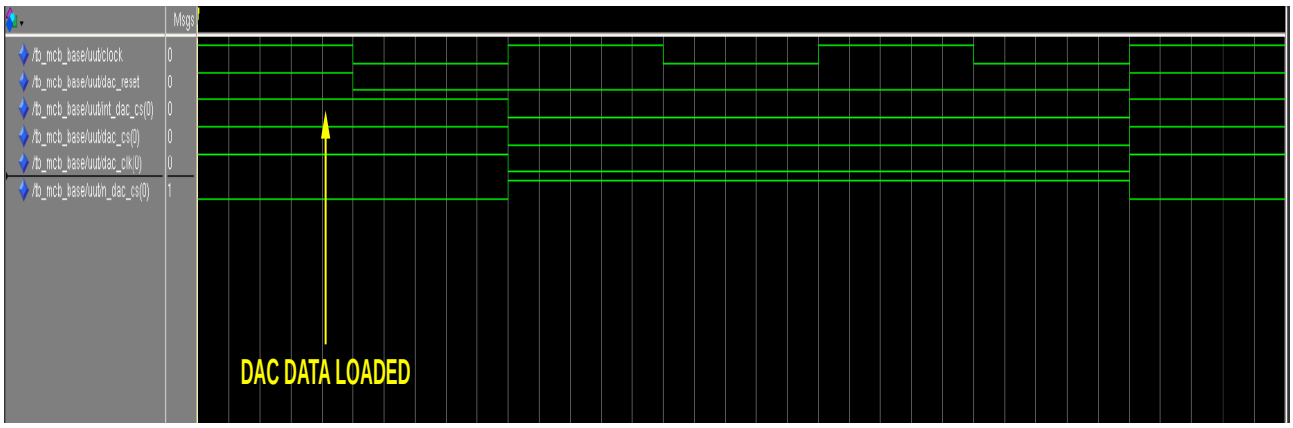

Figure 3.10: The DAC data values are fed to the chip when the clock is high and remains at such value until a call for a reset.

register.Thereafter, with these conditions imposed and with the appropreate number of clock cyles, the data from the detector are flushed out from the FPGA in serialised data with serial width equal to the number of chips per module. For intance as shown in Figure 3.13, the serial data (*eg. fpga_out* are flushed from the FPGA for 16-bit dynamic range after the data is unloaded from the shift register. Outputs for the different dynamic range have chip_out assignments. *chip_out2* is assigned for 16-bits, and copied exactle to fpga_out.

A channel has a 4-bit configuration register that allows various functions of the chip to be enabled : *CALENABLE* enables the calibration input, *N_ANENABLE* routes the analog output of the output buffer, *COUNT_ENABLE* that enables the comparator output and *COMPOUTENABLE* that routes the comparator output to the buffer. In addition, each pixel has a 6-bit DAC for trim register to reduce the threshold dispersion. This selects the trim threshold value. The DAC is linear and its value sums to the global chip threshold, *V_threshold*. The least significant bit (LSB) is defined by the value at the *ITRIM* in Figure 3.7. The bits of the configuration register and trim register compose bits 0-9 of the input shift register. These bits are loaded to the configuration register of all the selected channels.

Each channel features a 24-bit assynchronous counter that are enabled by counter modal signals. On counting mode, the value stored in bits 10 to 33 of the 34-bit register are loaded to the counter for the selected channel and the incoming X-rays are read in parallel. At this point, no pixel (channel) is selected, and the the comparator output, if enabled, is routed by the output buffer by bit 9 *COMPOUTENABLE* of the register to the counter input.

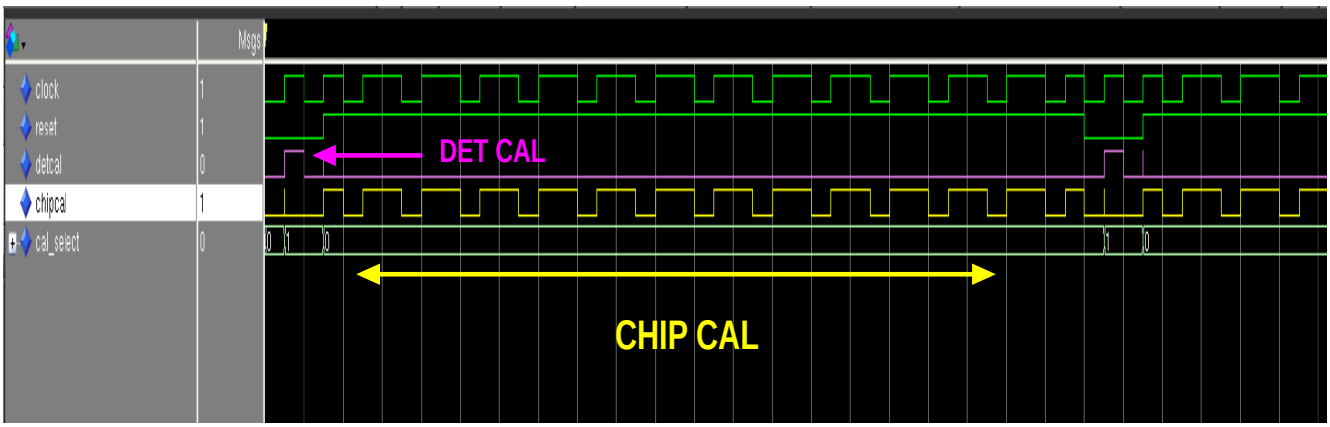

Figure 3.11: The calibration pulse is given to the detector via a counter in one clock pulse (signaled by the clock), otherwise the calibration pulse to the chip is called to calibrate each chip of the module.

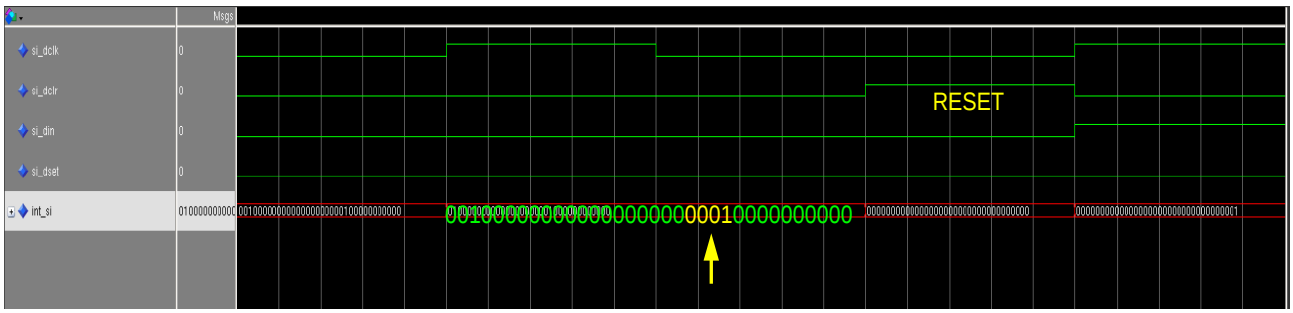

(a) 24-bit

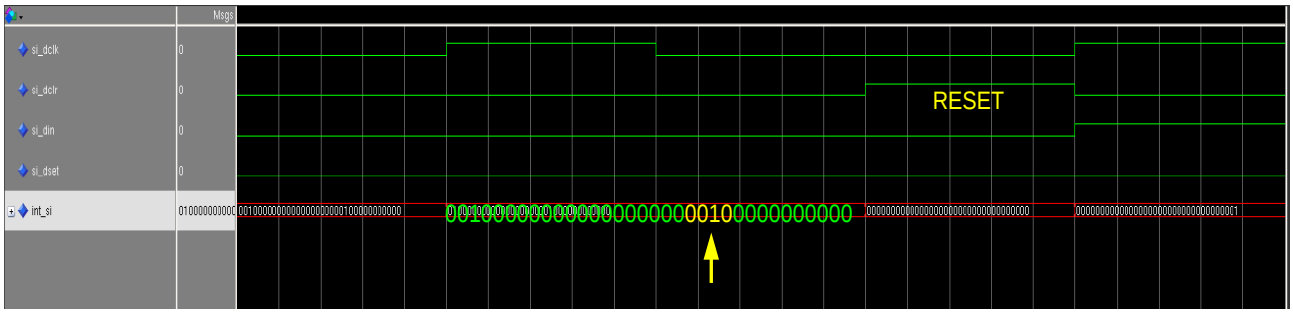

(b) 16-bit

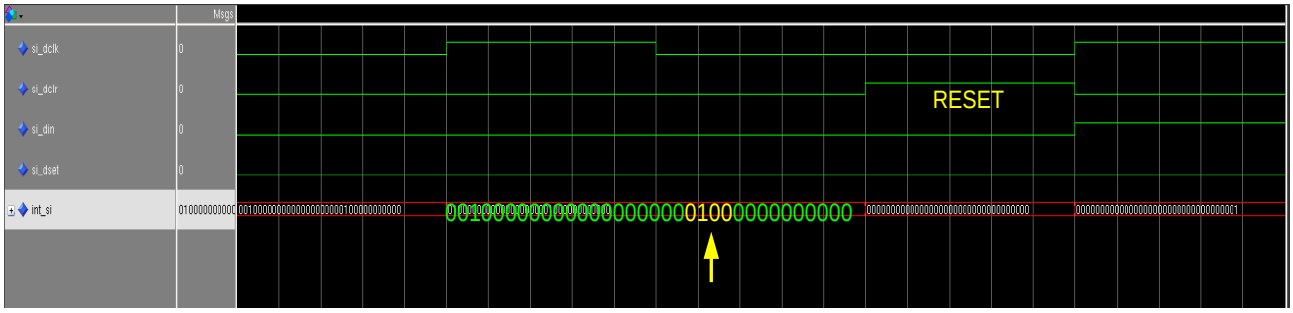

(c) 8 bit

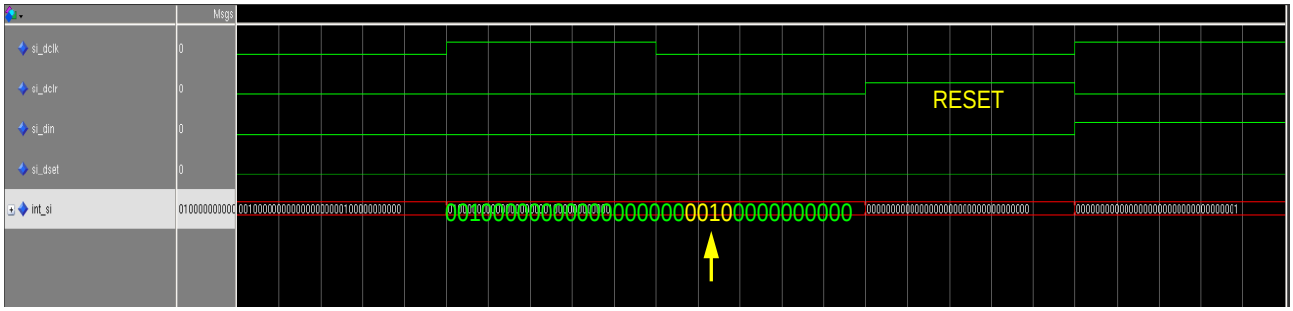

(d) 4 bit

Figure 3.12: The input shiftin register. Bits 20 to 23 of the shiftin register is used as a modal signal to select the dynamic range of the readout. This output selects which are routed to the output lines of the chip. Before clearing the contents of this register, the contents of register must be (b) 0001 for 24-bit readout, (c) 0010 for a 16-bit readout, (d) 0100 for a 8-bit readout and (e)1000 for a 4-bit readout. The data coming from the counter are outputed in the in lines $DTOUT$ shown in Figure 3.7.

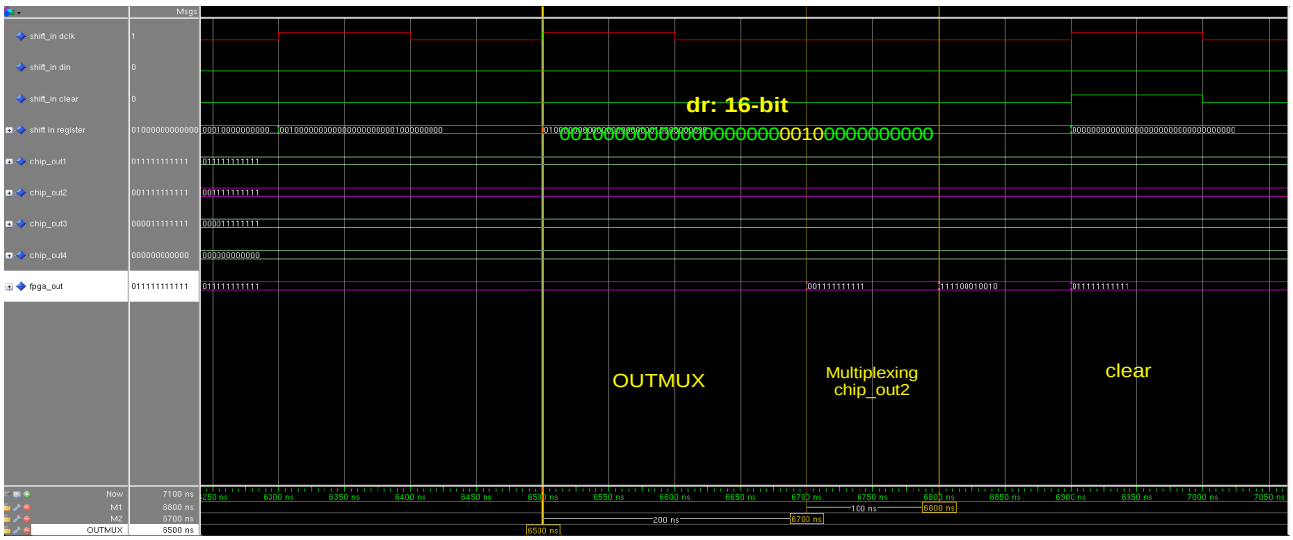

Figure 3.13: An example of serialised signal fo 16-bit dynamic range, after a the modal signals have been defined the iput shift register. *chip_out2* is assigned to 16-bits and copied exactly to *eg. fpga_out*

3.3 PICASSO Detector Control Board

The PICASSO controll board, shown in Figure 3.14, can control up to six detector modules. It is based on MCS6 (Mythen Control System - 6) designed at Paul Scherrer Institut in Switzerland. It has 5 lemo connectors where input/output signals can be coursed through. Enumerated below are the list of lemos and their descriptions:

1. *Gate in*

   Input to the gate signal that can be utilized for synchronization with other instruments.

2. *Gate out*

   Output for a gate signal generated internally in the board that can be provided for other instruments for synchronization. It is active when the detector is counting.

3. *Trigger in*

   Intput for the trigger signal that can be utilized for synchronization with other instruments.

4. *Trigger out*

   Output for the trigger generated internally in the board that can be provided for other instruments for synchronization. It gives a clock signal when the detector is finished counting a frame and is read-out.

5. *HV*

   Input that can be used to provide high voltage to the detector.

The lemo lines for the gates and trigger have a 3.3V LVTTL logic standard.

3.3.1 The microcontroller

The PICASSO detector control board is based on an embeded linux system microcontroller (AXIS Communications [71]) which directs the FPGA controlling the detector. It interacts with the acquisition PC via a server-client architecture over a 100 Mbit Ethernet standard network (compatible with IEEE 802.3 and Fast Ethernet standards). The network parameters may be reconfigured using its *http* interface or remotely and manually by *telnet* or *ssh*. The controller has a RISC CPU with a 32-bit data and address format that runs at 100-MHz clock. It makes use of a highly optimised CRIS (Code Reduced Instruction Set) compiler and typically gives less code then the i386 instruction set.

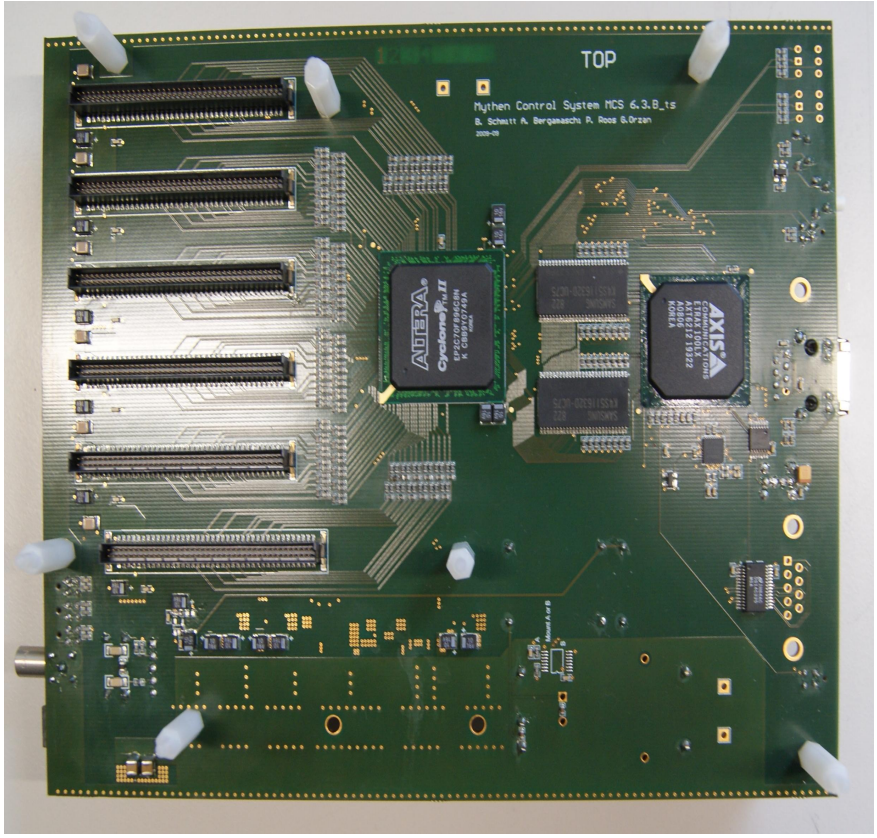

Figure 3.14: The PICASSO detector control board.

3.4 The PICASSO Software

The actual software for PICASSO is highly based on the MYTHEN II system (Mythen Control System 1 to Mythen Control System 24) also developed by the Swiss Light Source Detector Group. The version for PICASSO has been tested on a 32-bit (i386) SL-5 [72], a linux release based on Enterprise Linux primarily put together by CERN and FERMILAB. It has been tested with gcc version 4.1.2 [73] but higher versions are not critical.

3.4.1 The text client

While it is much convenient to initialize the detector, configure the measurement parameters and then perform the acquisition with a graphical user interface (GUI), it also posisble to integrate the detector in situations where integration with other controls (such as detector sample holder controls and related accessories) in the development phase. The text client does not have the ability to post process the acquired data, with such operations performed offline. The text client has been extensively tested only for data acquisition and not for more complicated procedures such as trimming and flat field normalizations.

3.4.2 Configuration

The system is configured first before running an acquisition. Several variables need to be defined:

1. **hostname**

   The hostname or IP address of the controller. The controller IP address and static computer hostnames and also *aliases* properly mapped to the controller's IP address that are previously defined in the network configuration of the acqusition computer may be used. In the case of the whole Picasso system, each control system has its unique address. The *alias* index associated with the addresss are always started with ''0", with ''0" acting as *master* if triggering is applied. Henceforth, data coming from the controller with alias index = 1 will be appended with data from the *master*.

2. **nmod**

   The number of modules connected to the Picasso Control System (PCS). The user defines a number for this that should be less than the maxumim allowable modules a PCS can hold.

3. **dr**

   The detector dynamic range. For the PICASSO system, it is possible to set to 4-bit, 8-bit, 16-bit and 24-bit dynamic range, 16-bit used as default for imaging acquisitions performed at the SYRMEP beamline.

4. **settingsdir**

   As for the MYTHEN-II chip, several default settings are routinely used for several applications. The *standard* DAC settings of the chip is treated as default for the PICASSO system. *settingsdir* is called in order to assign global values for the DAC chips in each of the PICASSO modules. Assigned here are the pre-amplifier voltage, shaper voltage, calibration pulse, global threshold and the count adjustment voltage. This is also the location where the default (all trimbits set to zero) and processed trim files are stored. Each module is assigned with a trim file, and such is identified with the module serial number. This identification is matched with strings provided in the firmware of the individual modules. In case that the interface ports were interchanged for all 12 modules of the PICASSO detector, this proper matching maintains the trimbit assignment for each channel of the module.

5. **caldir**

   The users supply here the calibration files where the average gain and offset for each Picasso module.

3.5 Detector Characterization

3.5.1 Detector energy calibration

Single photon counting detectors are sensitive to single photons and in pprinciple only the Poisson-like behavior of X-rays provides the constraint in detector response. The signal carried by the detector does not provide information on the energy of the interacting photon, *ie.*, no information on the signal amplitude, and all X-rays having energy larger than the imposed threshold in the comparator are counted and will carry 1 bit. Therefore, the choice of a threshold to be set in the comparator is crucial in order that a good quality data is collected.

The number of counts, N_0, as a function of the threshold energy for a monochromatic X-ray is often described by an S-curve that can be explained as the sum of the signal spectrum from the set threshold to infinity. Figure 3.15 shows the number of counts as a function of threshold for photons of 17 keV. The red curve is a step function that presents the characteristics of an ideal photon counting detector that is devoid of noise from the electronic readout chain and in the absence of charge sharing, while the actual behavior of the detector, presented in the black curve, deviates from the ideal curve because of charge sharing that adds a slope to the plateau and electronic noise that is presented as an abrupt rise in counts after the slope.

The response of the detector, $\mathrm{S}(E_t)$, as a function of the threshold energy E_t at photon energy E_0, may be approximated as the composite contribution of the sum counts due to the noise, N_n, and the counts due to the photons, N_{ph}. That is,

$$S(E_t) = N_n + N_{ph}. \tag{3.1}$$

The noise and photon contributions [41] are given by

$$N_n \simeq \frac{T}{\tau_s}\mathrm{D}\left(\frac{-E_t}{ENC}\right) \tag{3.2}$$

and

$$N_{ph} = \frac{N_0}{2}\left(1 + C_s\frac{E_0 - 2E_t}{E_0}\right)\mathrm{D}\left(\frac{E_0 - 2E_t}{E_0}\right), \tag{3.3}$$

respectively. T is the acquisition time, τ_s is the shaping time. The noise coming from the electronics is given by the electronic noise charge (ENC) that describes the noise in terms of the charge at the detector input needed to create the same output at the end of the analog chain [74]. ENC is dependent of the the shaper settings, and it increases with short shaping time. ENC is normally expressed in electrons and may be converted into energy units, *ie.* 1 e^- = 3.6 eV for Silicon.

The optimal threshold setting for energy E_0 is the threshold level at half of E_0, *ie.*, $E_t = E_0/2$. It means that if the threshold is lower than E_t, there appears to be a charge enchancement as two neighboring strips encodes independently a single charge that has been generated in an interaction point in the sensor. Since the charge is recorded twice, this implies that the spatial resolution is degraded as well as increased fluctuation in the number of photons due to cascades because of Compton effect, (ie.) charge multiplicity [75] . Conversely, when the set threshold is higher than E_t, the charge may not be detected at all, thus bringing down the efficiency of the detector.

The slope in the black curve in Figure 3.15 is a consequence of charge sharing. There is partial collection of charge liberated by radiation at an interaction point between two strips. The rise due to this phenomenon has been modelled elsewhere [76, 77] and the fraction of the shared charge is denoted by C_{shared} given by

$$C_{shared} = \frac{N_{shared}}{N_0}. \tag{3.4}$$

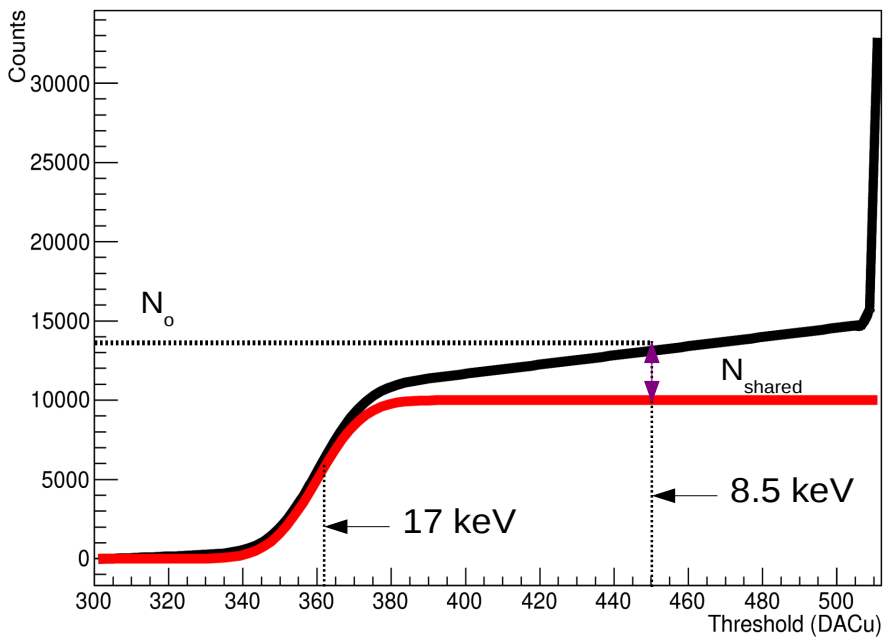

Figure 3.15: The expected count behavior for a 17 keV monochromatic photon beam with and without noise as a function of threshold. The red line represents an ideal case without intrinsic noise and charge sharing. In black is the physical case with C_{shared}=38% charge sharing. N_{shared} is the photons shared between to adjacent strips, while N_0 is the number of photons collected at the optimum threshold setting.

The resultant signal, S, from the detector is a convolution of the noise and the radiation spectrum. For a monochromatic source, it follows a Gaussian cumulative distribution D, and will evetually rise with the increase of threshold as a consequence of the baseline noise.

Considering both signal amplification and the comparator are linear, it is important to calibrate the detetcor gain G and offset O to properly set the comparator threshold V_{thresh} at the desired energy E_t. This was done by collecting threshold scans at different photon energies. The experimental data per channel has been fitted againts equation (3.3), and the median inflexion point among the channels in each module i has been calculated. A linear relation results between the x-ray energy and the median comparator voltage with the slope as G and y-intercept as O. They act as conversion factors between the threshold level and the energy.

Settings	Gain (mv keV^{-1})	Offset (mV)	ENC (e^-)
Standard	4.5±0.05	294.6±9	227±13

Table 3.1: Calibration Results

Presented in Figure 3.16 is the calibration curve derived from four modules of the of the PICASSO detector as described above with error bars indicating differences among the modules.

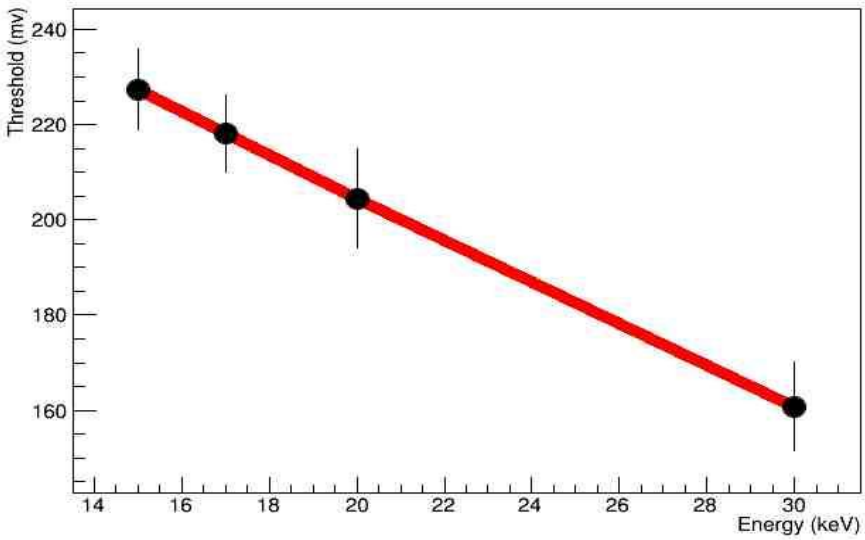

Figure 3.16: The position of the inflection points as a function of the beam energy

3.5.2 Trimming

The choise of the level of the comparator is important in photon-counting systems because it plays an impact not only on the detector efficiency, but also on the spatial resolution as described in the preceeding section. The resposnse of each channel in a module may not be uniform. The threshold dispersion in the module may originate from fabrication inhomogeneities and voltage drops along the power distribution lines in the read out chip [78]. Uniformity in the threshold is especially important in mammography applications because of the low variation in the attenuation characteristics of breast tissues, and phase contrast imaging because of the involvement of wave shifts. Data quality however may be improved if the threshold will be set high enough so that low level signals due to noise that do not contribute to the image quality may be discarded, in addition to low variation among channel counts.

One speacial feature of the Mythen-II chip is the possibility of trim the detector so that the channels are forced to respond uniformly to a flat field. Six bits in the 32-bit input shift resgiter, described above, are assigned for comparator threshold adjustment. The comparator threshold is provided on a global level that is set on a module-by-module basis in the readout system. Optimization on the detector response may be done by setting some adjustment on the pixels by bringing each count around the median count of the channels in the module. The readout system permits two triming modes: with *(1.)* noise and with *(2)* X-rays.

1. **Noise** This procedure is performed without X-rays. The trimbit correction for each channel are so chosen so that all channels in a module have the same number of counts at some defined thereshold, *Vthresh* usually defined around 500 DACu (425 mV) where the baseline noise is about to start. This threshold may be altered to achieve a satisfactory trimbit distribution in the active channels of the module, however avoiding too much the steep rise in the noise. The user has the freedom to set the number of counts in a given time interval, and the correction is limited within 2σ. The trimbit distribution for one module with 1536 channels would normally appear as a Gaussian centered around

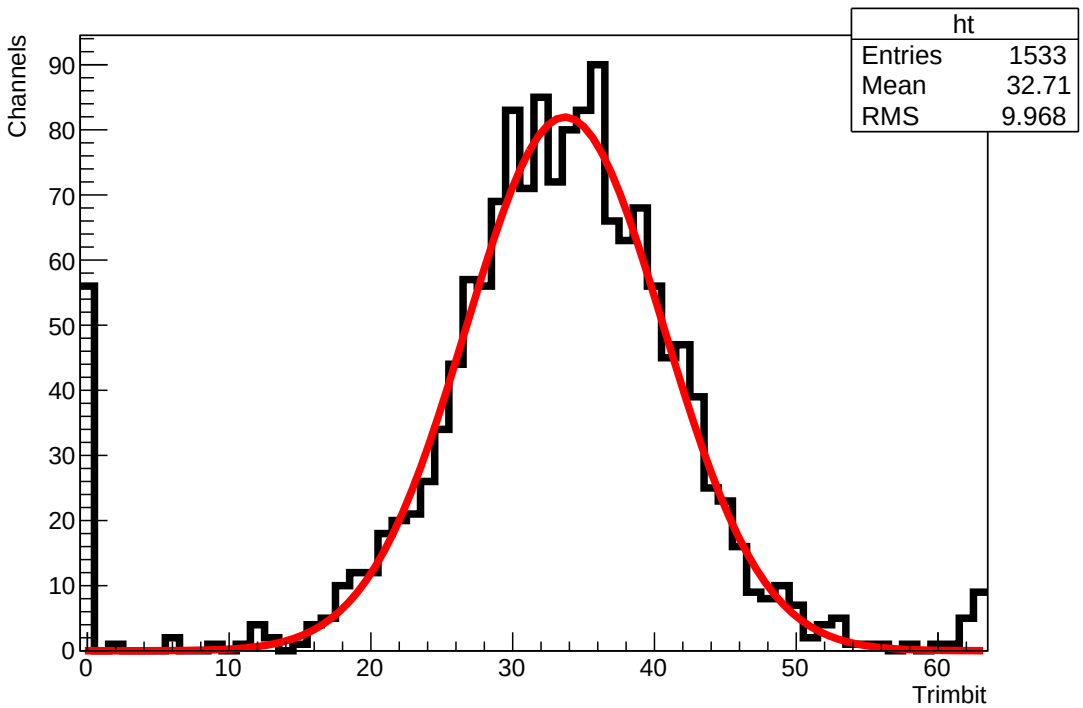

Figure 3.17: Trimbit distribution of among channels from one PICASSO module.

trimbit 32 as depicted in Figure 3.17. The trimbit assignment for one channel is calibrated with respect with the median counts from the noise acquisition, with the lowest count assigned to the least significant bit (LSB) and the highest count to the most significant bit (MSB). For this example, poorly undbonded channels are discarded and are not included in the trimming procedure hence less channels are reported.

2. **Trimming with X-rays** While *noise trimming* as above is enough for our applications as flat field correction would usually suffice to gain uniformity for the images, the detector may also be trimmed with the use of x-rays. The size of the trimbits are calibrated in terms of global threshold, V_{thresh} using threshold scans at trimbit 0 and Vtrim scan at trimbit 63. The former defines comparator threshold global to the channels in the module, while the latter defines the size of the LSB of the trim DAC.

   V_{thresh} is defined at threshold 10% of E_t of the threshold scan described above, while V_{trim} is defined at 10% of the V_{trim}'s S-curve. See Figure 3.18. 10% window is set at both sides to account for chip response uncertainties.

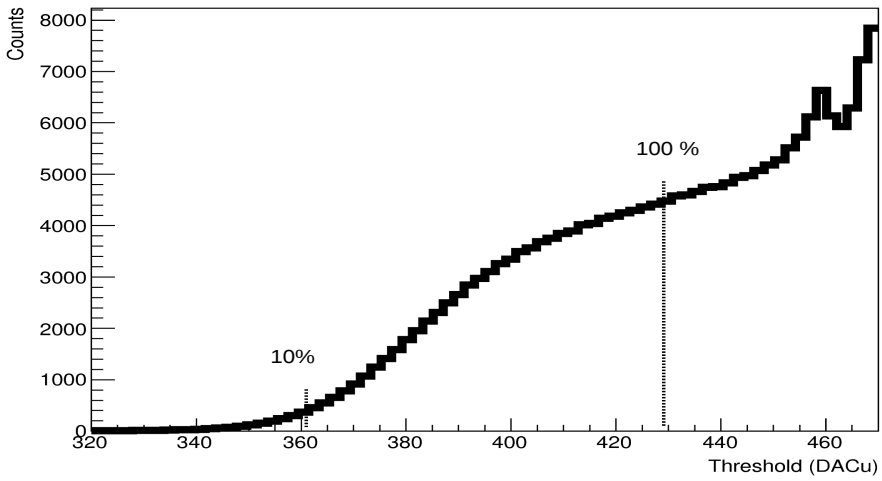

(a) V_{thresh} scan with trimbit 0

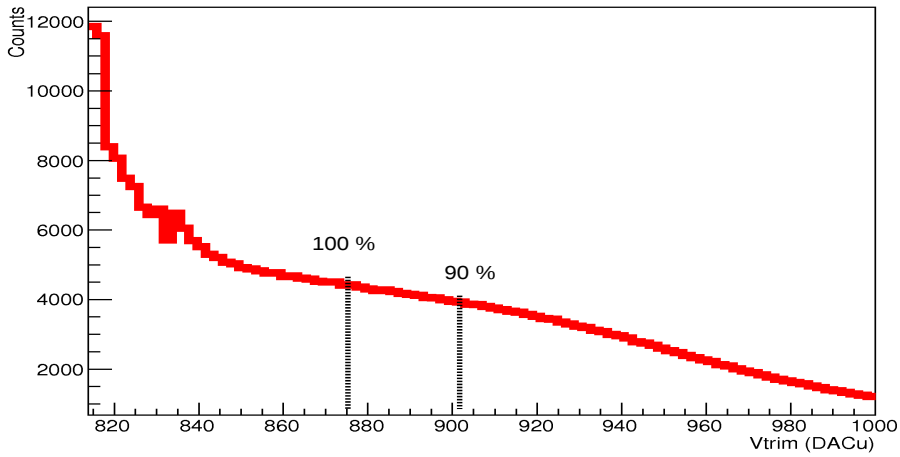

(b)V_{trim} scan with trimbit 63

Figure 3.18: (a)V_{thresh} has been determined from the 10% of the S-curve of a threshold scan and (b)V_{trim} has been determined from the 90% of the inverted S-curve from a Vtrim Scan.

3.5.3 Maximum count rate

Deviation from the linearity of counts with respect to the number of x-rays absorbed in the detector happens at high fluxes for photon-counting systems due to pile up of the analog signal [36]. For PICASSO, it follows a paralyzable behavior

$$\varepsilon = exp(-\tau_d \Phi), \tag{3.5}$$

where Φ = N(E)/T is the photon flux absorbed by the detector while τ_d is the deadtime. τ_d rises with the shaping time, and is approximates the width of the signal at the chosen threshold. The efficiency of the detector with respect ot the count rate has been determined for PICASSO accorfing to equation (3.5) by illuminating the detector with monochromatic X-rays modulated by different Aluminum filtration to vary the number of photons reaching the detector. The measurements were performed with standard top-up operation mode at Elettra Synchrotron at ring energy of 2.0 GeV and ring current of around 300 mA. The measurements has been performed at 19 keV photon energy and the τ_d over several channels for the detector is 410±13 ns.

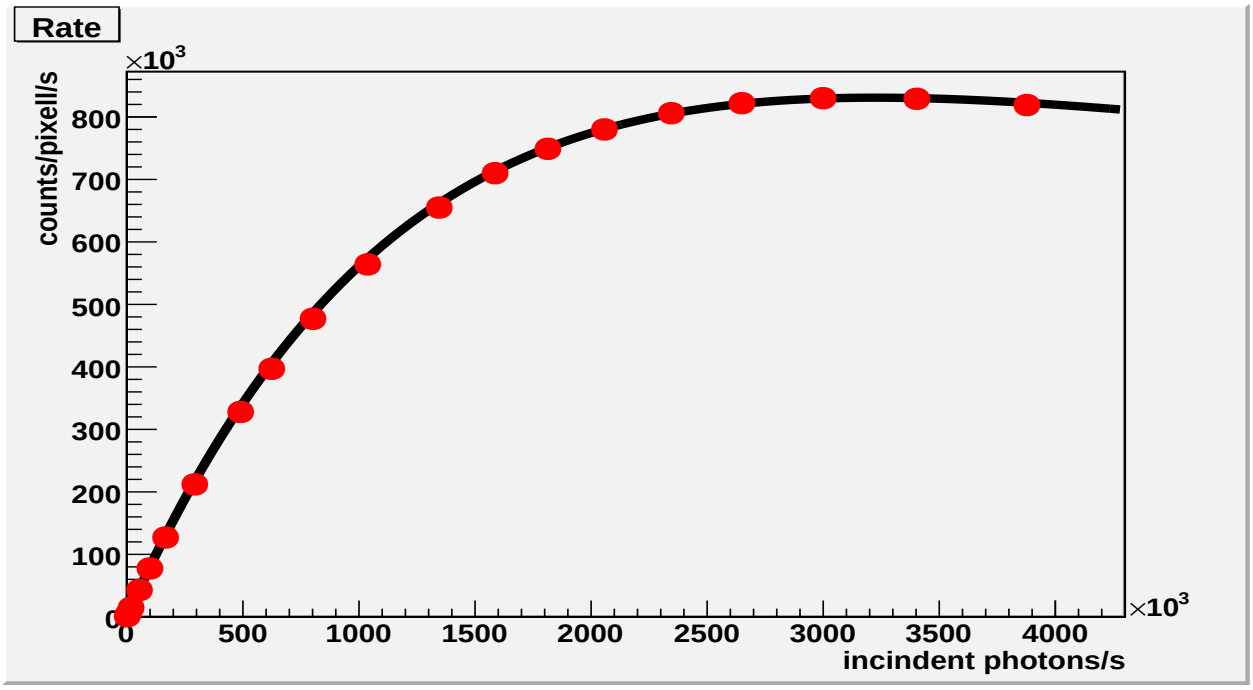

Figure 3.19: PICASSO detector efficiency at 19 keV at the standard settings of the read-out chip. The efficiency was modelled according to the paralyzable behavior of detectors. The deadtime, τ_d, is 410±13 ns

Chapter 4

Performace evaluation of the Picasso detector

The presently biomedical synchrotron radiation (SR) imaging techniques (see next chapter) require a detector of sufficient field of view, with a pixel size suitable for resolution imaging (50 μm or smaller). *In-vivo* projection and tomographic studies require a low noise and a fast readout system adapted to laminar beam. Moreover, the detetor must maintain a high efficiency over a wide energy range to minimize the dose delivered to the sample and to minimize the acquisition time. Wide detectors specifically developed for SR imaging are exteremely rare [79, 80, 81, 82, 83]. Many commercial X-ray detectors for medical imaging are present in the market featuring one or several of the characteristics above but unfortunately do not spotlight all at the same time. For wide active area mammography operation, a group in Sweden has been actively improving their detector which is also based on Silicon, but theirs has been limited to conventional X-ray sources so far [84]. In the case detectors for mammography with synchrotron sources, none apart from our group has put effort in building a wide silicon-based detector operating in *edge-on* configuration.

Alongside the creation of a new readout system for the upgraded Picasso electronics is the need to evaluate its electronic performance and imaging capabilites. In this chapter, we present the first imaging results obtained with the detector. More focus is given to absorption imaging as activities with phase-contrast imaging will be detailed in the succeding chapter. Evaluation of the imaging performance of the system will also be presented in terms of contrast, signal-to-noise ratio spatial resolution and framing rate.

4.1 First results with the new readout electronics

The ability of the detector to scan huge samples and the first results obtained with the 2-layer Picasso prototype with the new electronics will be presented. This is to demonstate that the system is capable of managing huge data transfer from 9216 channels with high stability.

In order to evaluate the capability of the PICASSO detector to scan breast-size samples, a TORMAX (Leeds Test Objects, Ltd, Boroughbridge, UK) mammographic phantom was scanned. It has a diameter of 22 cm, thickness of 1 cm and it contains several details designed for image evaluation [85]. Phantom was sandwiched between 1.5 *cm* perspex slabs so that the composite thickness simulates an average woman's breast. The object was scanned continously across the beam at a velocity of 4 *mm/s* in front of the stationary detector. The image of the phantom was acquired at a frame rate of 33 *Hz* at 24-bit dynamic range with data directly transfered to the PC resulting to a total scan time of 28.8 *s*. The beam energy was 20 keV and the delivered air entrance dose was 3.7 *mGy* that is comparable to the entrance dose delivered in conventional mammography.

In mammography, the contrast between masses and background structures are fairly small [86] and such presents a challenge in lesion detection. In order to to evaluate the low-contrast sensitivity of the PICASSO system, the twelve low contrast details of the TORMAX phantom, labelled as *(a)* in Figure 4.1a has been evaluated. The details are 5.6 *mm* in diameter forming a series of diminishing contrast. Contrast, defined here as

$$C = \frac{\Delta I}{I_o} \tag{4.1}$$

where ΔI is the difference between the signals from the detail and the background, I_b. The target signal was obtained as the average counts over a 0.082 cm^2 region of interest (ROI) in the middle of the circular region, while the mean surrounding background was estimated by averaging four regions of the same size located at positions around the target. The data are reported in Table 4.2. The lowest visible contrast is 0.4%.

(a) TORMAX phantom

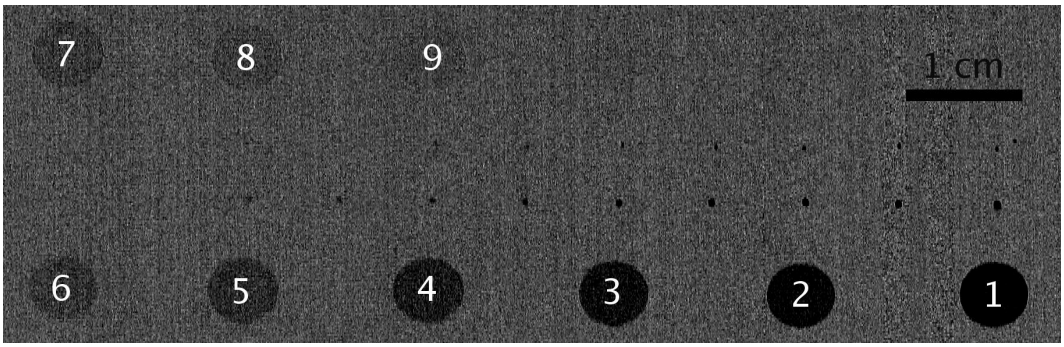

(b) Low contrast details of the TORMAX phantom.

Figure 4.1: TORMAX phantom imaged at 20 keV (a) Details labelled as *(a)*, *(b)*, and *(c)* are low contrast details, high resolution gratings perpendicular and parallel to the scanning direction, respectively. (b) Low contrast details of the TORMAX phantom and the visibility metrix used to evaluate the performance of the PICASSO system. The labels in the image correspond to the detail number presented in Table **??**

The contrast is not affected by the image noise but the detail visibility depends on the noise. For each detectable detail in the low contrast detail region in the TORMAX phantom, the signal-to-noise ratio (SNR) was evaluated. It is defined as

$$SNR = \frac{\Delta I \sqrt{A}}{\sigma_b} \tag{4.2}$$

where A is the area of the ROI, ΔI as previously defined and $\sigma_b$is the background standard deviation. The image presented in Figure 4.4 shows good visibility of 9 out of 12 disks in the phantom and it is a fulfillment of the Rose criterion where the SNR must be at the neighborhood of 5 for a detail to be visible [87, 88]. In conventional radiology, contrast lower that 2% is difficult to be detected [89]. The image was acquired at a dose comparable to the dose delivered in clinical mammography, the visibility threshold is below the contrast of 0.5%.

Picasso's pixel dimensions are defined by the strip pitch (horizontally) and by the wafer thickness of the sensor (vertically). To characterize the spatial resolution of the system, the two high resolution gratings

Detail Number	Contrast(%)	SNR
1	6.72	80.46
2	4.48	53.10
3	3.27	40.50
4	2.40	30.06
5	1.51	19.08
6	1.17	14.58
7	0.86	10.80
8	0.68	8.46
9	0.44	5.40

Table 4.1: Contrast and signal-to-noise ratio of the different low contrast details labelled in Figure 4.4

of the TORMAX phantom was used. These gratings have spatial frequencies from 1 to 20 *lp/mm* and are positioned perpendicular to each other. The resolution gratings labeled as (b) in Figure 4.4 have line patters perpendicular to the scan direction, while (c) have line patterns parallel to the scan direction. The modulation as a function of spatial frequency n, was experimentally estimated from the image of the bar patterns using the following formula [90] :

$$MTF = \frac{I_{max} - I_{min}}{I_{max} + I_{min}}. \tag{4.3}$$

I_{max} and I_{min} are the maximum and minimum counts along the average profile of the pattern group, respectively. At 50% modulation, the fringes were resolvable at 1.8 *lp/mm* at the perpendicular oriented gratings while 11.2 *lp/mm* at the parallel-oriented gratings. Differences are due to both the asymmetry of the pixel size and the continuous scan during acquisition, necessary to match the acquisition time constrain of mammography. However, the spatial resolution along the scanning direction can be improved by *dithering* or by using horizontal slits to shape the beam [91].

4.2 Rate and contrast

One of the advantages of photon counting systems is the possibility to maximize contrast. Low energy photons which carry contrast information about the detail have the same weight from the high energy photons (that in integrating system degrade image quality).

In photon counting systems, the loss in efficiency at high rates is mainly dictated by the signal pile-up and baseline shift. A loss in efficiency can be observed at low threshold when the signals pile-up in the region around the peak of the signal. While for high threshold, a second signal at a later time spikes upon the undershoot of a first signal leading to loss of efficiency. The pile up determines a paralyzable model [36] as described in the previous chapter, with the deadtime related to the shaping time. Rate response of counting systems has been simulated by Bergamaschi [92]. With an increased rate, the counts generated per photon are low at low threshold and high at high threshold signals. Signal pile-up results to a loss of counts at low threshold, however increases the counts at thresholds higher the signal amplitude. The contrast is flat at low rates then makes a sharp fall off at high rates. It is therefore important to choose a threshold discriminator setting so that pile up is not introduced to the system to maintain the contrast of a detail at varous rates.

Evaluation of the contrast as a function of rate taken with of the contrast detail cluster of the TORMAX phantom is presented in Figure 4.2. This cluster consists disks of varied thickness. This image was acquired by scanning the object in front of a 22 *keV* beam at average count rates 120 *kHz* and 580 *kHz*. The object was imaged in continuous scan mode at the detectors fastest framing rate and at a scanning resolution that mimics the detectors pixel width. Increasing the flux did not affect significantly the image quality. With low contrast details however, a loss in contrast is expected at high count rates as exemplified by Disk 5.

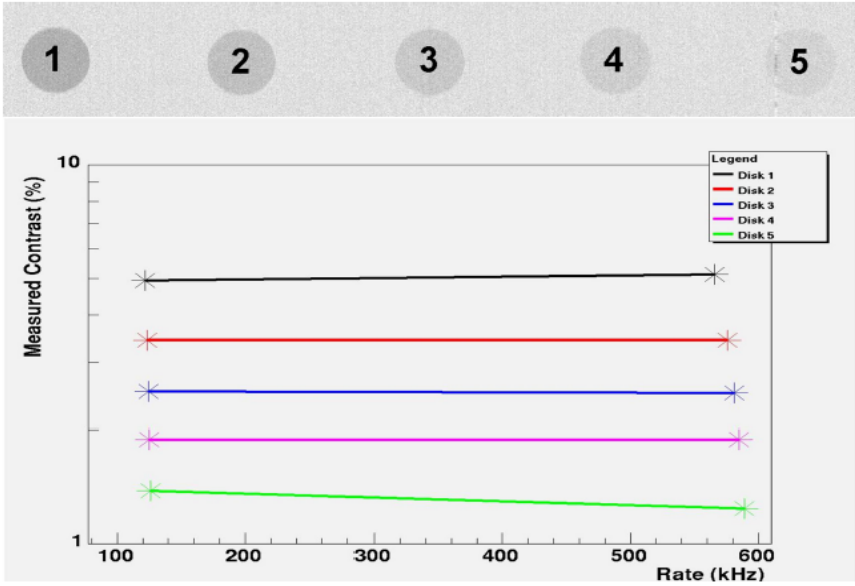

Figure 4.2: A fraction of the Tormax phantom (Leeds Test Objects Ltd) with disks of decreasing thickness and measured contrast at 120 kHz and 580kHz.

4.3 Picasso imaging at the patient room of the SYRMEP beamline

As mentioned in the previous chapter, Picasso was developed aiming to supply a digital detector to patient hutch of the SYRMEP beamlline. The detector, with the new readout electronics, was tested for the first time at this end station and the results are herein presented. The set-up for this preliminary run is illustrated in Figure 4.3. A thin laminar beam was utilized measuring approximately 200 mm in width and 3.4 mm in height at the position where the breast is usually situated. The detector was at a stationary position 32 m away from the source while the object being imaged was positioned at the breast compressor 2 m upstream and just underneath an ergonomically shaped patient support.

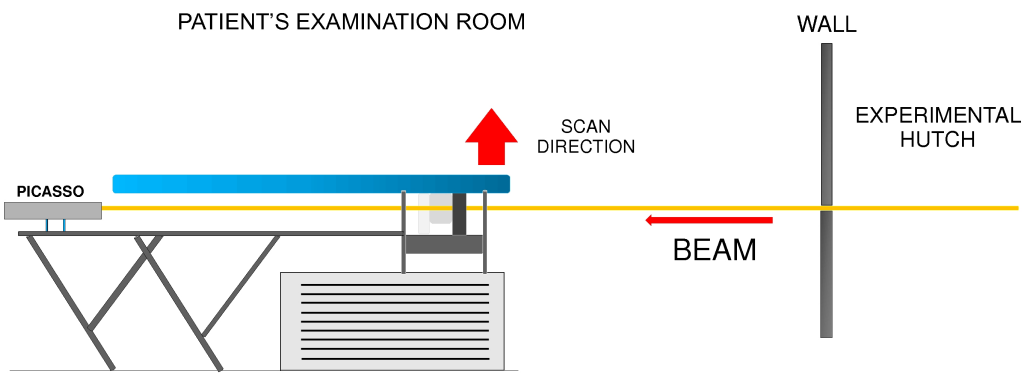

Figure 4.3: Experimental set-up employed with the Picasso detector at the SYRMEP beamline.

The object was scanned continuously at different travel speeds of the support system at a constant exposure time of 10 ms giving us different effective resolutions and delivered doses. At this run, ELETTRA storage ring energy was 2.4 GeV. This permitted us to evaluate the detector at the maximum possible flux at our beamline.

The new PICASSO read-out system was tested for the first time at the radiological hutch of SYRMEP using $19keV$, $22keV$ and $24keV$ photon energies with the use of American College of Radiology (ACR) mammographic accreditation phantom. This phantom has a thickness that approximates a $4.5cm$ breast.

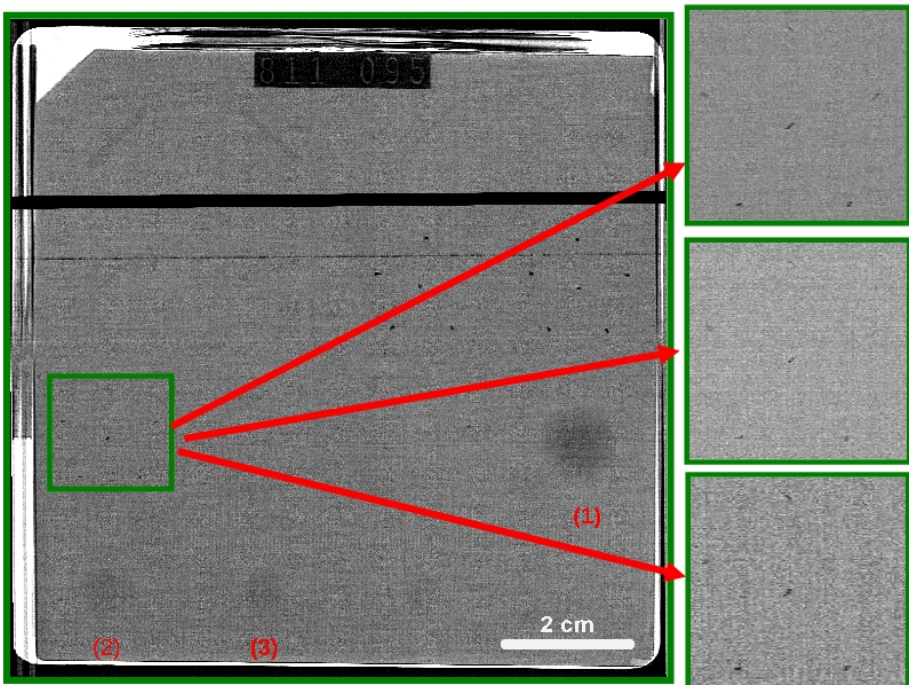

.

Figure 4.4: Image of the whole ACR mammographic phantom (left). The phantom was scanned at different effective resolution. To its right are magnified images of Al_2O_3 details sized $0.32mm$ taken at different travel speeds. Details of the scan and mean gladular dose are provided in Table 4.2

	TOP	MIDDLE	BOTTOM
Scan speed (mm/s)	5	10	15
Effective resolution (μm)	50	100	200
Mean glandular dose (mGy)	0.49	0.43	0.39

Table 4.2: Scan details performed on the ACR phantom in Figure 4.4. Top, middle and bottom represents the images in the left of Figure 4.4.

The mean glandular dose delivered to the phantom was calculated using Boones approximation [93] on normalized glandular dose. The test object was scanned at difterent speeds, and the enlarged image of the 0.32 mm Al_2O_3 spekcs that are emebedded to the sample are presented in Figure 4.4.

At 50μm resolution, the time required to finish the acquisition took only around 20 seconds. Mean glandular dose delivered to the phantom is up to 10 times lower compared to what is delivered by standard mammographic units.

The dose is reduced by a factor of 2 and 3 when the patient support speed was increased two and three times, respectively since the acquisition time was maintained. However, the increased scan velocity degrades the visibility of small details.

Visibility was evaluated using contrast and signal-to-noise ratio with the detector set to 16 - bit dynamic range. Resolvable masses represented by labels (1), (2) and (3) in Figure 4.4 were assessed. Given in Table 4.3 are the SNR and contrast for each of the resolvable details for different energies. SNR and contrast increases with the detail thickness, hence better visibility, while contrast degrades with the increase in energy.

Resolution (μm)	Energy (keV)	Thickness (mm)**	SNR	Contrast (%)
50	19	0.75	21.40	1.72
		1.0	30.25	2.44
		2.0	73.11	5.77
	22	0.75	20.35	1.22
		1.0	37.79	1.67
		2.0	69.40	4.15
	24	0.75	17.59	1.07
		1.0	21.12	1.25
		2.0	64.90	3.30

Table 4.3: Signal-to-noise ratio and contrast achieved with the PICASSO detector at 50-micron effective resolution and different photon energies. **The tumor-like details are labelled accordingly at the ACR phantom image in Figure 4.4. (1), (2) and (3) corresponds to 2 mm, 1 mm and 0.75 mm thickness, respectively

Chapter 5

Phase Contrast Imaging with the PICASSO Detector

The PICASSO detector has been developed by our collaboration mainly to be used for imaging research with phase contrast imaging. Along with the tests performed with the PICASSO detector are preliminary imaging experiments not only aimed to evaluate its imaging performance, but also to evaluate its compatibility with novel imaging techniques. In this chapter, the first imaging results taken with excised beast samples acquired with the upgraded readout electronics will be presented. Moreover, planar imaging with phase-contrast techniques will be reported. In particular, results with non-interferometric coded-aperture phase-contrast imaging with synchrotron radiation will be shown [94]. The details of the method and experimental set-up will be detailed here, as well the images generated using the technique will be presented.

5.1 Phase Contrast Imaging

Among the list of limitations in various clinical imaging methods inlcude insufficient spatial resolution, contrast and quantitative scaling [95]. In the case of X-rays, delivered dose to the object being imaged also adds to the constraints. The use of synchrotron sources allows new solutions to these issues, as it also permits novel techniques to be performed such as *phase-contrast imaging*. At this point, we briefly describe the physical foundations that governs X-ray phase-contrast imaging, and highlight several techniques employing this method.

X-ray interaction with target materials can lead to various processes such as absorption, excitation and ionization. These processes can bring about several types of X-ray scattering that carry valuable information about the structures they come across during their flight towards the detector. These information may be exploited for medical imaging and briefly we layout the physics governing the process.

X-ray phase-contrast imaging makes use of wavefront changes that are produced when the photons traverses the object. The transmitted wave is a consequence of the incoming beam being attenuated and scattered elastically by the sample. In the wave formalism, an electromagnetic X-ray propagating in the z-direction, can be expressed as

$$\Psi = \Psi_0 e^{ikz} \tag{5.1}$$

where Ψ_0 is the wave amplitude, and k $= \frac{2\pi}{\lambda}$ is the wave number. Let us say the wave travels in a homogenous medium, k may be re-written as $k_{medium} = nk$, with n as the index of refraction. The resultant wave emerging from the sample Ψ_{out} is the product of the incident wave and a transmission function *T(x,y)* [96].

$$\Psi_{out}\left(x,y\right) = T\left(x,y\right)\Psi_0 e^{ikz}. \tag{5.2}$$

T(x,y) is a complex function and can be written as

$$T\left(x,y\right) = A\left(x,y\right)e^{i\phi(x,y)} \tag{5.3}$$

where

$$A\left(x,y\right) = e^{-k\int\beta(x,y,z)dz} \tag{5.4}$$

$$\phi(x,y) = -k \int \delta(x,y,z)\, dz \tag{5.5}$$

with integrals evaluated at full extension of the object along the *z-direction*. Therefore, crossing the object affects in wave both in the amplitude and phase. One also anticipates a reduction in amplitude that is well accounted for by the so-called Beer-Lambert law:

$$I = I_0 e^{\mu(x,y,z)dz}. \tag{5.6}$$

The attenuation component given by equation (5.4) is a statement of the reduction intensity A_2 (x,y)= $e^{-2k\int \beta(x,y,z)dz}$ is equivalent to (5.6) given by the linear attenuation coefficient and the imaginary part of the index of refraction, such that:

$$\mu(x,y,z) = \frac{4\pi\beta(x,y,z)}{\lambda}, \tag{5.7}$$

while the phase shift indicated in (5.5) may be obtained with X-rays as waves and not considered in the particle model. Using the small-angle approximation expressed as

$$|\nabla_{(x,y)}| \ll k \tag{5.8}$$

it is possible to express the local vector of propagation $\rho_k(x,y,z)$, as a function of the phase gradient in the direction perpendicular to the incident wave vector:

$$k'(x,y,z) = \left(\frac{\partial\phi}{\partial x}, \frac{\partial\phi}{\partial y}, k\right) = \nabla_{x,y}\phi + k_z. \tag{5.9}$$

With simple geometric considerations [97], the angle of defelection with respect to z is

$$\theta(x,y,z,k) = \frac{1}{k}|\nabla_{x,y}\,\phi(x,y,z,k)|. \tag{5.10}$$

In the X-ray regime, the index of refraction is usually written as

$$n = 1 - \delta(x,y,z) + i\beta(x,y,z), \tag{5.11}$$

δ is the decrement of the real part of the refractive index, characterizing the phase shifting property, while the imaginary part β describes the absorbtion properties of the material. These coefficients may approximated in classical terms as

$$\delta = \frac{r_e \rho_e \lambda^2}{2\pi} \tag{5.12}$$

$$\beta = \frac{r_e \rho_e \lambda^3}{4\pi^2 c} \sum_i \frac{f_i \gamma_i}{Z} \tag{5.13}$$

where λ is wavelength of the X-ray, r_e is the classical electron radius, ρ_e is the electron density of the material, c is the speed of light in vacuum, f is the number of electrons per molecule at a damping constant γ_i, and Z is the atomic number. Both δ and β are very small for hard X-rays incident on light materials such as biological samples, but the value of δ can be several orders or magnitude higher than β. In the energy range used mammography (15-25 keV), the values of β are around 10^{-8} - 10^{-10} while δ are typically in the range 10^{-6} - 10^{-7} [98]. The real and imaginary parts rely quite differenly on the energy of the incident photon, consequently giving numerical values that are so different the for light elements in the human body. This implies that the effects due to the phase term can be 2-3 orders of magnitue higher than the absorption term. Therefore, variations in soft tissue density provies stronger phase contrast effects than absorption contrast, notably after 10 keV [99]. The sensitivity of X-ray imaging can be strongly enhanced, especially when the absorption contrast is not adequate to differentiate small details embedded in a similar background which can be the case, for instance, of a breast malignancy in a health gladular tissue. Likewise, phase-sensitive techniques could provide high quality images also when there is low absorption of X-rays and therefore low dose administered to the subject. This could be exploited with X-ray energies that are normally higher than those used in medical imaging. Both δ and β decrease when moving towards high

X-ray energies, but while β decreases with the third power of energy, δ decreases with the second power, as shown in equations (5.13) and (5.12), respectively.

The transmitted beam from an object is a result of the attenuated beam and the forward scattered beam. If δ has a lateral gradient, the phase front is deviated (the x-ray wave is refracted). A simple schmatic is shown in Figure 5.1. The angle of refraction, θ can be calculated from Snell's law at an interface where the refractive index changes by $\Delta\delta$:

$$\theta = \Delta\delta \tan\alpha. \tag{5.14}$$

This angle is the same as described in equation (5.9) with vlaues in the order of microradians in the case of biological samples. α is the angle between the gradient and the incident beam and tan $\alpha = \frac{dz}{dy}$.

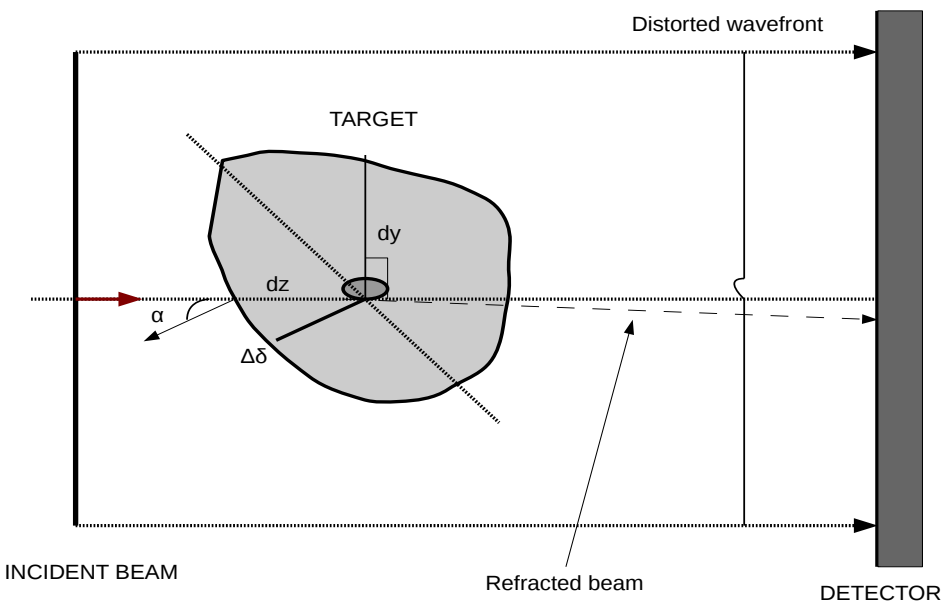

Figure 5.1: Illustration of the refraction of a photon in a sample.

Several phase sensitive techniques has been developed over the past 20 years. As it is an fast evolving field, new approaches continue to be developed at an increasingly rapid pace often keyed with technological developments.In the next subsections, we will present these approaches namely : Propagation-based phase contrast imaging, Analyzer-based imaging and Interferometry.

5.1.1 Propagation-based phase-contrast imaging

The first group and the simplest in terms of instrumentation may be grouped as *Propagation-Based Phase-Contrast Imaging (PPCI)*, also known as *Free-Space Propagation*, or *In-line holography*. This method requires a source of high spatial(lateral) coherence.

Considering a coherent source from a point (x_0, y_0) placed on a plane normal to the z-axis and consider here a spherical incident wave. Invoking Maxwell's principles, this radiation in free space can be described as

$$E_0(x_1, y_1) = \frac{1}{r} exp\left[\frac{2\pi i}{\lambda}\left(r + \frac{(x_1 - x0)^2}{2r} + \frac{(y_1 - y0)^2}{2r}\right)\right] \tag{5.15}$$

Here, x_1 and y_1 are point coordinates in the image receptor place and r is the separation between the source and the detector, while λ is the wavelength. If an object is positioned in between the source and the detector, one has to account for the phase shift in the field. Using Snigirev's [100] example for instance where the change front takes place in the x-direction, and let us say that the image of finite size in the range -R<x<R, we should rewrite eqiation (5.15) as

$$E(x_1, y_1) = E_0(x_1, y_1)\left[1 + c\left(x_1\right)\right]. \tag{5.16}$$

where the second coefficient is the propagator that is responsible for the image formation that takes the form

$$\begin{aligned} c(x_1) &= \sqrt{\frac{r}{i\lambda r_0 r_1}} exp\left[\frac{2\pi i}{\lambda}\left(-\frac{(x_1-x_0)^2}{2r}\right)\right] \\ &\times \int_{-R}^{R} dx\, exp\left[\frac{2\pi i}{\lambda}\left(\frac{(x-x_0)^2}{2r_0}+\frac{(x_1-x)^2}{2r_1}\right)\right] \\ &\times \{exp[i\phi(x)]-1\} \end{aligned} \tag{5.17}$$

where r_0 and r_1 are the source-object and object-image distance, respectively. In the case of synchrotron beamline set-up such that of SYRMEP, r_0 is large with respect to the the distance allocated for object-image distance, *ie* $r_0 \gg r_1$ and with the assumption that r=r_0= ∞ making equation (5.17) a simpler expression

$$c(x_1) \approx \frac{1}{\sqrt{i\lambda r_1}} \int_{-R}^{R} dx\, exp\left[\frac{2\pi i}{\lambda}\frac{(x_1-x)^2}{2r_1}\right] \times \{exp[i\varphi(x)]-1\}. \tag{5.18}$$

An example of an image taken taken with the Picasso detector employing propagation-based phase contrast imaging is shown in Figure 5.2. It is a set of wires with diameter = 0.4 mm obtained at a distance of 135 cm from the detector. The image was acquired at an acquisition time of 500 ms. The edge-enhancement, as seen in Figure 5.2a is a typical PPCI effect due to the phase shift $\phi(x,y)$ described in equation (5.12) and the contrast is proportional to the Laplacian of the phase shift with calculated with respect to the transverse coordinates, *ie.* $\left(\frac{\partial^2}{\partial x^2}+\frac{\partial^2}{\partial y^2}\right)\phi(x,y)$. Figure 5.2b is the extracted intensity profile of second wire from the bottom. Both edges of the wires show more or less symmetrical contrast with contiguous positive and negative peaks.

This modality has shown great potential in the field of biomedical imaging with the latest and most detailed account is in the article by Bravin *et al.* [101]. A relevant application of PPCI has been realised in mammography. Mammography by far is the golden standard in breast cancer diagnosis and also the key element in many breast screening programs that aref conducted worldwide. However, a challenge remains with the linear attenuation of breast cancer that is very similar to that of healthy structures in the breast (*ie.* glandular tissue) [86] that hinders its detection among dense breasts. With the powerful offer of PPCI to highlight breast cancer especially in the borders because of its phase shift properties, the technique appealed many to invesigate this capability. The SYRMEP collaboration here in Trieste, Italy extesively studied this modality and have demostrated the validity on test objects and excised breast tissue samples [26, 102]. The results were so encouraging that a mammography facility was built at Elettra (see Chapter 1). A clinical trial was concducted from 2006-2009, where 71 patients have undergone mammography with PPCI technique [33] with the use of screen-screen system.

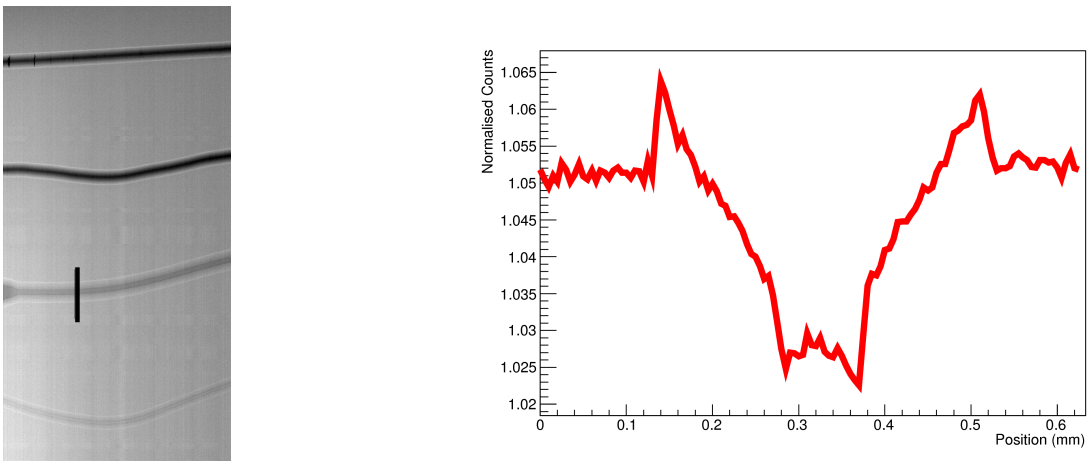

(a) (b)

Figure 5.2: Phase contrast example

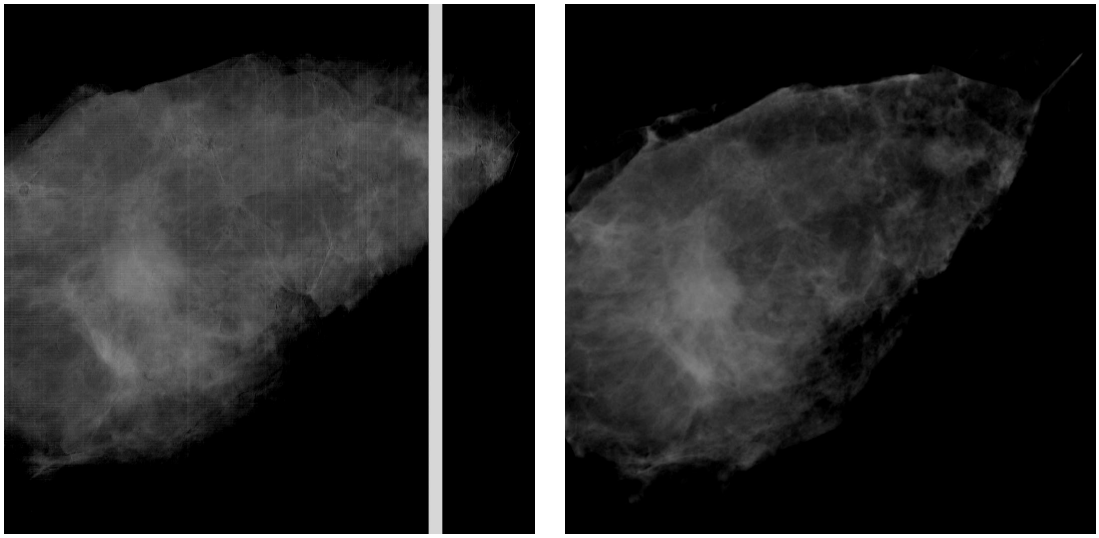

(a) (b)

Figure 5.3: Two mammograms from the same breast sample. On the left : Phase-contrast image with synchrotron radiation. On the right: conventional digital mammography from a GE Senograph unit.

The technique has proven well with the detector used in this work on breast tissue samples as exemplified in Figure 5.3. On the left is an image of a breast tissue obtained with a single layer of PICASSO at the SYRMEP beamline. The image was acquired by scanning the sample across a stationaty beam at a speed of 5 mm/s an acquisition time of 30ms/frame using 19 keV photon energy. While on the right is an image of the same sample acquired using one of the conventional mammography units of our university hospital using a 28 kV_p polychromatic source from a Mo-Mo target. Enclosed in the box in both images are fibrous tissue that is better enchanced in the image with phase-contrast.

5.1.2 Analyzer-based imaging

Another class of methods employing phase contrast involves the use of perfect crystal analyzers with quasi parallel and monochromatic X-ray beams. An example set-up of which is presented in Figure 5.4. The analyzer acts as a very narrow angular slit, reflecting only the rays that make the correct Bragg angle with the atomic planes of the crystal. This modulates the intensity of the beam reaching the detector. The fundamental idea with this technique is that if the crystal, when perfectly tuned at the peak of its reflectivity curve (the so-called *rocking curve* in the figure's inset), could serve as a selective anti-scattering grid. The reflectivity curve in the figure's inset is obtained by measuring the intensity transmitted by the analyzer towards the detector as a function of the misalignment angle.

Esentially, the X-rays traversing the sample postioned between the monochormator and the analyzer crystal can be transmitted, scattered or refracted. Refraction occurs at the boundary of the material with diffferent δ at angles in the order of milliradians. It is possible to extract additional phase from refraction by tuning the analyzer at different positions on the rocking curve. When the analyzer is tuned to reflect at the peak position, any x-ray that is deviated by refraction or scattering is reflected less efficiently. Moreover, scatter from object internal structures in the range of hundreds of nanometers up to micrometers and which occurs at angles of several *microradians* (ultra-small angle X-ray scattering, USAXS) is rejected, and highlights the so-called *extinction contrast* [103], similarly for slightly larger structures with respect to USAX, small-angle X-ray scattering (SAXS) charatectized by angles in the *milliradian* range.

As contrast in the image is a combination of all the many physical factors mentioned above, several algorithms have been developed to elucidate these information from the different contributions and they are well described in the literature. Listed below are different techniques involving analyzer crystals.

1. *Diffaction Encahned Imaging* method The measured rocking curve is linearly approximated at the positive and negative slope, and its second derivative is zero. When the object is into the beam, two

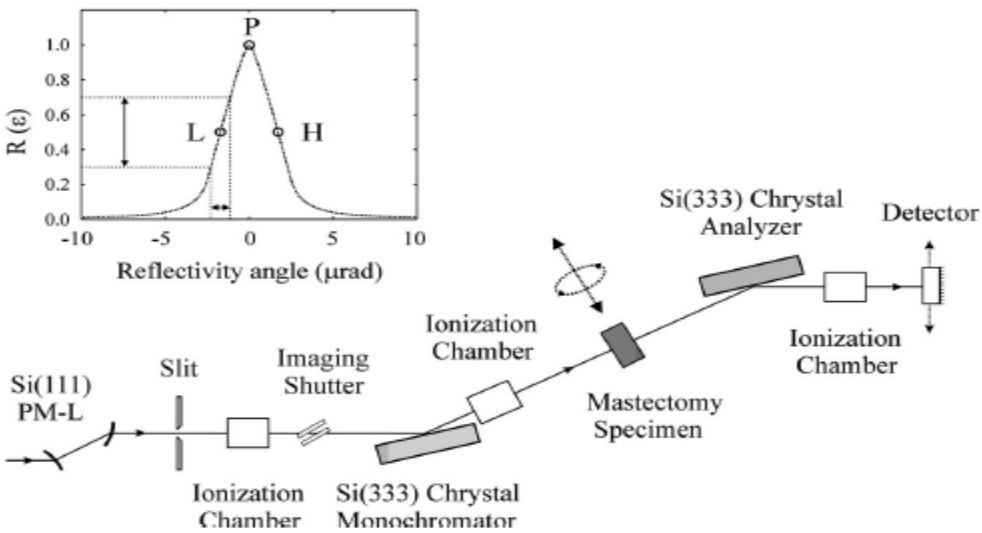

Figure 5.4: Simplified schematic representation of an analyzer-based set-up. It presents the principle of analizer-based imaging method that is mainly composed of monochromator and an analyzer crystal. The inset shows the relectivity curve, R(ε) of Silicon(3,3,3) at 33 keV. The reflectivity curve demonstates the conversion of the angular x-ray deviations. L, P and H represents the left-angle, peak and high-angle positions of the curve [104].

images are acquired with the analyzer: one at the positive and the other at the negative slope of the rocking curve [103].

2. *Generalzed diffraction-enhanced imaging* It is based on a second-order taylor approximation of the rocking curve. From the three points indicated in Figure 5.4, three images are generated : absorption, refraction and USAXS is analitically determined [105].

3. *Extended diffraction-enhanced imaging* It is based on fitting the rocking curve measured without the object with a Gaussian function and using the calculated expression to analytically extract absorption and refraction images from two images acquired at two arbitrary positions along the rocking curve. It is applicable to a wider range of angles because no linear approximation of the rocking curve is perfomred, and USAXS is not measured [106].

4. *Multiple-image radiography* The object rocking curve and the reference rocking curve is sampled at n$\geq$3 positions on the zeroth-, first- and second-order moments of the measured object and reference rocking curves to calculate the integrated absorption, refraction and USAXS images [107]. Since many images are needed to be obtained at several postions of the rocking curve, *ie.* n$\geq$3, the overall duration of the image aquisition and dose increase.

5. *Gaussian curve fitting* The rocking curve sampling is similar to *multiple-image radiograph*, *ie.* n$\geq$3, but also in fitting a Gaussian function on the measurement points. Abosrption, refraction and USAXS are calculated based on the area under the curve, the peak and the sigma [108].

Diemoz and co-workers [109, 110] did an extensive comparison on the above ABI extract algorithms on plastic phantoms and biological samples, and have noted that absorption, refraction and scattering signals vary tremendously especially at large refraction angles.

5.1.3 Interferomotry

The third method, known as *X-ray interfemometry*, was introduced by Bonse and Hart [111] in 1965, and is basically composed of thre parallel silicon wafers (see Figure 5.5) which stick out from monolithic perfect crystal ingots. The incoming beam is diffracted and split in two coherent wavefronts in the first wafer called splitter, S by means of amplitude division. These beams are split again by the second wafer called mirror, M. The inner beams join in the third wafer called analyzer, A. The interference pattern caused by the

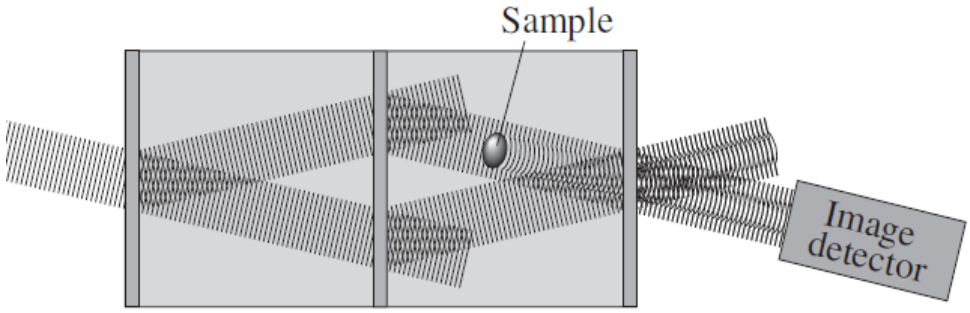

Figure 5.5: Schematic representation of the crystal interferometer reported by Bonse and Hart in the 1960s [112]

sample placed in one arm of the interferomenter is observed downstream the analyzer. The beauty of X-ray interferometry is it allows to access directly the phase shift (see equation (5.5)) introduced to the object rather than spatial derivatives. For propagation-based and diffraction-enhanced imaging methods, stronger contrast is generated at structural boundaries where variation of the refractive index are larger for steeper phase gradients. For shallower gradients, propagation-based and diffraction-enhanced imaging approach are not effective. Interferometric methods are suitable for this situation because the interference fringe patterns becomes larger for shallower phase gradients [113]. The system for biomedical imaging was first constructed by Momose in the mid-90s [114].

One big challenge with posed by crystal interferometry is in its instrumentation. The crystals used in this configuration must be perfectly aligned with each other due to the short wavelength of the X-rays, and means that the construction precision is in the order of atomic distance precision. Moreover, the size of the field of view is limited by the diameter of the crystal ingot from which the interferometer is fabricated. For instance, a floating zone (FZ) silicon ingot is prefered to ensure its performance as an like that of Bonse and Hart LLL interferometer, for instance. However the maximum diameter of commercially available FZ ingots is 15 cm, the maximum field of view available. In addition, imaging a human body gives problems to the crystals because the radiated heat from ths body deforms them [113]. Being a crystal method, X-ray interferometry has strict requirements on monochomaticity and beam collimation.

To overcome the limitations stated above, a new approach to interferometry has been used recently which based on the use of gratings (*grating interferometry*). This method usually employs two or three gratings and Talbot self imaging. The first grating positioned after the sample splits the incident beam essentially into two diffaction orders which generates a periodic interference pattern in the plane of the second grating positioned in front of the detector. The image of the first grating is repeated at regular distances behind the grating. A sample's phase and absorption information are encoded in the relative shift in the amplitude of fringes formed by self-imaging.

This method is quite robust, and it has been used in many laboratory settings. It has been applied in SR sources [115, 116], and high power rotating anode tubes [117, 118].

5.1.4 Coded-aperture X-ray phase contrast imaging

As mentioned in section 5.1.2, high quality images can be produced due to high scatter rejection and sensitivity to very small angular deviation from milliradians to microradians. The crystal approach provides excellent image quality over a wide array of samples but their implementation outside synchrotron radiation facilities is made extremely difficult as they require parallel monochromatic radiation.

Yet another technique with synchrotron radiation that can be used to extract phase-effects is known as *coded-aperture x-ray phase contrast imaging* first introduced by Olivo, *et al.* more than a decade ago [91]. This method can achieve a similar effect as that of the ABI imaging technique. In the ABI technique, an analyzer crystal is placed between the sample and detector and the narrow reflectivity curve of the crystal is used to discriminate diffracted and undiffracted photons. In the case of coded-aperture technique, narrowing the beam and shifting it with respect to the center of the detector pixel realizes the same. One can percieve

an entity (or a function) that can separate the photons that are detected and are not detected based on the diffraction angle after they emerge from the sample. The relative shift between a narow beam and pixel center defines the position of the entity (function) along the angle axis while the sample to detector distance and the pixel height defines the width. The smaller the pixel, the smaller the entity becomes. The behavior based on the width of this entity to some extent, equivalent to the *rocking curve* in diffraction imaging.

Coded aperture technique also resembles grating interferometry because of the presence of two gratings. The technique is, however, non-interferometric since it does not employ Talbots self-imaging phenomenon [119].

Coded-aperture technique has been modified and improved since then by Olivo and Speller [120, 121] and transfered it to laboratory practice with the use of conventional X-ray sources emitting polychromatic beam. For what concerns our Picasso detector, we are interested to evaluate the modified set-up cited in [120, 121] designed to perform X-ray phase-contast designed for laboratory sources in an idealised monochromatic point source that can be approximated by a synchrotron X-ray source. In addition, we are interested to understand the separation of quantifed absorption and phase perturbation using the technique formulated by Munro *et al.* [94] using a linear array detector such that of Picasso that is operating at a sufficient frame rate [69] that remains stationary in front of a moving sample . The working principle of this technique for what concerns the arrangement of the apertures with respect with the Picasso will be briefly described. Wire images as well as images of excised mammographic tissues using this modality will be presented.

The principle behind this work, also called *edge-illumination X-ray phase contrast imaging, EIXPCI* is depicted in Figure 5.6. It is normally composed of two masks. One is placed before the object (here we will call *pre-sample aperture*) with dimensions put to scale according to beam divergence. Several of these openings creates a multiplicity of individual beams, each hitting the pixel edges of given by the succeding mask. The other mask is positioned in front of the detector (called the *detector aperture*) alligned with the pixel arrays of the PICASSO detector. This creates a intensive region in the detector element, and positioned in place in the entirety of the experiment. The system works by projecting the X-ray beam onto the edge of the of a sensitive part of the detector and will be sensitive to phase gradients in the vertical direction and to the direction with which the sample is scanned.

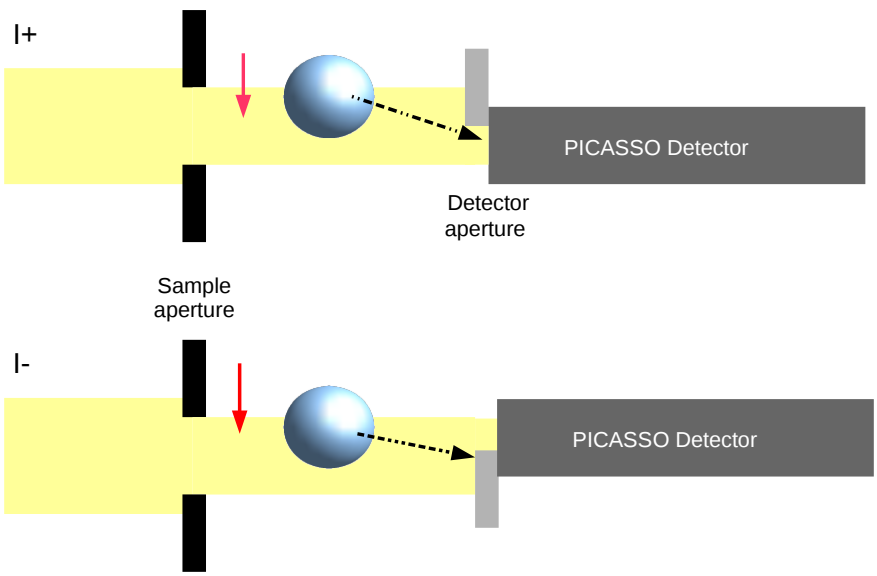

Figure 5.6: The beamlet given by the first aperture impinges the sensitive area of the pixel defined by the detector mask.

Edge-illumination formalism

In this section we will introduce here the formalism for edge-illumination following the algorithm written by Munro, *et al.* [94] where this work has been involved using the two apertures described above. The formalism assumes that the pitch of the apertures matches the size of the pixel. The key point here is

to illuminate the edge of a pixel by setting the two apertures depicted in Figure 5.6. The degree of pixel illumination called the *illuminated pixel fraction* accounts for the sum of the intensity normalised to its maximum [119]. The maximum is noted when the opening of the two masks are totally alligned.

As already been mentioned in Section 5.1, the index of refraction is expressed as n = 1 - δ +iβ, with δ and β as the refractive index decrements. We also mentioned that when a wavefront traverses a thin object, it will be perturbed by the sample's transmission function given by *T(x,y)* that may also be expressed in terms of A and ϕ previously defined. That is,

$$T(x,y) = exp\left(-\phi(x,y) - A(x,y)\right) \tag{5.19}$$

We will pressent the set-up in simple terms by limiting our attention to a pair of apertures as depicted in Figure 5.6, rather than a set of beamlets from multiple openings from the sample mask. We will evaluate edge-illumination by acquiring images of the same object at different detector mask configuration but maintaining an IPF = 50%. The configurations presented in the figure yields a contrast that is inverted. I_- and I_+ configurations will produce a signal produce less and greater than the flat field, respectively. also, let us say that the object in between the masks is low absorbing.

The formalism is going to be laid out assuming a monochroamatic point source. Let us say that our beam is travelling in the *z-direction*. In the small-angle approximation, the intensity of the photon is constant in the transverse direction (*y-direction*). If the detector response is uniform and the object is homogenous, then we say that the change in intensity is only in the *x-direction*. We assign the Ψ(x) as the complex amplitude of photons from the detector aperture incident on the pixel with height p. The intensities due to this complex function is given by

$$I_- = \int_0^p \int_{-K}^0 \Psi(x)|^2 dxdy \tag{5.20}$$

$$I_+ = \int_0^p \int_0^K |\Psi(x)|^2 dxdy. \tag{5.21}$$

The pre-sample aperture width, L, is magnified by a factor M is denoted by

$$M = \frac{(z_0 + z_1)}{z_0}, \tag{5.22}$$

where z_0 is the source-to-object distance, z_1 is the object-to-detector distance and K is given by the product of the sample aperture width and the magnification factor. Since we are neglecting the dependence from y, we rewrite equation (5.19) as *T(x)*. We introduce ξ as x-direction to mean that we are in the object-space, just to make a distinction with the detector-space. We assume that phase and absoption may be described by a linear function so that the transmission factor becomes

$$T(\xi + \xi_s; \xi_i) = exp\left(-\phi(\xi_s) - i\frac{\partial\phi}{\partial\xi}\bigg|^{\xi_s}(\xi - \xi_i) - A(\xi_s) - \frac{\partial A}{\partial\xi}\bigg|^{\xi_s}(\xi - \xi_i)\right), \tag{5.23}$$

where ξ_s is the shift of the sample with Taylor series taken about ξ =0 and ξ_i is used to shift the Taylor series representation of the transmission function. With ξ=0, they are coincicdent with the aperture before the object. Within small-angle approximation to the Fresnel-Kirchoff diffraction, the complex function reaching the detector mask is well described in detail by a previous work by Munro, *et al.* [119] and is given by

$$\Psi(z) = C\int_{-L/2}^{L/2} T(\xi - \xi_s; \xi_i)\, exp\left(ik\xi^2\frac{z_0 + z_1}{2z_0z_1}\right) exp\left(-ik\xi\frac{x}{z_1}\right) d\xi. \tag{5.24}$$

As previously mentioned the intensity at the transverse is constant and

$$C = \frac{\Psi_0}{\sqrt{i\lambda z_0 z_1 (z_0 + z_1)}} exp\left(ik(z_0 + z_1)\right) exp\left(ik\left(\frac{x^2}{2z_1}\right)\right). \tag{5.25}$$

Ψ_0 is the amplitude of the wave coming from the source and expressed as in [119] as

$$\Psi_0 \sim Cexp\left(i\left(\frac{\partial\phi}{\partial\xi}\bigg|^{\xi_s}\xi_i - \phi\left(\xi_s\right)\right)\right)exp\left(\frac{\partial A}{\partial\xi}\bigg|^{\xi_s}\xi_i - \mu\left(\xi_s\right)\right)\frac{i\lambda z_0 z_1}{z_0+z_1}$$
$$exp\left[-\frac{\partial A}{\partial\xi}\bigg|^{\xi_s}\frac{z_0 z_1}{z_0+z_1}\left(\frac{x}{z_1}+\frac{1}{k}\frac{\partial\phi}{\partial\xi}\bigg|^{\xi_s}\right)\right]exp\left[-\frac{ik}{2}\frac{z_0 z_1}{z_0+z_1}\left(\frac{x}{z_1}+\frac{1}{k}\frac{\partial\phi}{\partial\xi}\bigg|^{\xi_s}\right)^2\right] \tag{5.26}$$

which is acceptable in the range

$$x \in \left[-K - \frac{1}{k}\frac{\partial\phi}{\partial\xi}\bigg|^{\xi_s} z_1, K - \frac{1}{k}\frac{\partial\phi}{\partial\xi}\bigg|^{\xi_s} z_1\right] \tag{5.27}$$

and zero elsewhere. With equation (5.26) substituted in equations (5.20) and (5.21), we now present I_- and I_+

$$I_- = \mathscr{A}\left[exp\left(\frac{\partial A}{\partial\xi}\bigg|^{\xi_s} L\right) - \mathscr{B}\right] \tag{5.28}$$

$$I_+ = \mathscr{A}\left[-exp\left(-\frac{\partial A}{\partial\xi}\bigg|^{\xi_s} L\right) + \mathscr{B}\right], \tag{5.29}$$

respectively. $\mathscr{A}$ and $\mathscr{B}$ are expressed as

$$\mathscr{A} = \frac{|\Psi_0|^2 exp\left(2\frac{\partial A}{\partial\xi}\bigg|^{\xi_s}\xi_i - 2A\left(\xi_s\right)\right)}{2z_0\left(z_0+z_1\right)\frac{\partial A}{\partial\xi}\bigg|^{\xi_s}} \tag{5.30}$$

$$\mathscr{B} = exp\left(\frac{-2\frac{\partial A}{\partial\xi}\bigg|^{\xi_s} z_0 z_1 \frac{1}{k}\frac{\partial\phi}{\partial\xi}\bigg|^{\xi_s}}{z_0 z_1}\right). \tag{5.31}$$

Photons passing through the first aperture that has not traversed the sample but falls within the pixel sensitive region for both I_- and I_+ set-ups will be inlcuded. Taking the sum and difference of equations (5.28) and (5.29) yields

$$I_- + I_+ = 2\mathscr{A}\sinh\left(\frac{\partial A}{\partial\xi}\bigg|^{\xi_s} L\right) \tag{5.32}$$

$$I_- - I_+ = 2\mathscr{A}\left[\mathscr{B} - \cosh\left(\frac{\partial A}{\partial\xi}\bigg|^{\xi_s} L\right)\right] \tag{5.33}$$

For us to understand the phase-effects, we have to extract 1/k $\frac{\partial\phi}{\partial\xi}\Big|^{\xi_s}$ from the image. The image may be acquired through two means: (1) through periodic apertures with a flat panel detector or through (2) dithering where the sample is scanned with respect to the the detector. But since the Picasso detector is a linear array detector, we will proceed with the dithering approach with a single mask opening from the two apertures. From I_- and I_+ signals at positions ξ= -$\Delta\xi$, 0, $\Delta\xi$, we have

$$\frac{\partial A}{\partial\xi}\bigg|^{\xi_s} = \frac{1}{4\Delta\xi}log\left(\frac{\left(I_- + I_+\right)|^{\xi=\Delta\xi}}{\left(I_- + I_+\right)|^{\xi=-\Delta\xi}}\right) \tag{5.34}$$

Wire	Material	δ [122]	β [122]	Nominal diameter (μm)
A	*Titanium*	2.19×10^{-6}	3.46×10^{-8}	$250 \pm 10\%$
B	*Sapphire*	2.03×10^{-6}	3.97×10^{-9}	$250 \pm 10\%$
C	*Aluminum*	1.35×10^{-6}	4.22×10^{-9}	$250 \pm 10\%$
D	*PEEK*	7.15×10^{-7}	2.74×10^{-10}	$450 \pm 10\%$
E	*PEEK*	7.15×10^{-7}	2.74×10^{-10}	$200 \pm 20\%$
F	*Boron*	9.17×10^{-7}	2.29×10^{-10}	$200 \pm 10\%$

Table 5.1: Propertes of the wires making up the sample at an energy of 20 keV. PEEK stands for polyetheretherketone. δ and β were taken from were from [122]. The wires and their nominal diameters were obtained from Goodfellow (Goodfellow Cambridge Ltd., Huntington UK)

But for instance, with a limited acquisition time, we may only have access to postions ξ= -$\Delta\xi$, 0, equation (5.34) can be written as

$$\left.\frac{\partial A}{\partial \xi}\right|^{\xi_s} = \frac{1}{2\Delta\xi} log\left(\frac{(I_- + I_+)\,|^{\xi=0}}{(I_- + I_+)\,|^{\xi=-\Delta\xi}}\right). \tag{5.35}$$

The absorption component can be then extracted at ξ=0,

$$\begin{aligned} A(\xi_s) &= \frac{1}{2} log\left[\frac{I_0}{(I_- + I_+)\Big|^{\xi_i=0}} \frac{\sinh\left(\left.\frac{\partial A}{\partial \xi}\right|^{\xi_s} L\right)}{\left.\frac{\partial A}{\partial \xi}\right|^{\xi_s} L}\right] \\ &\approx \frac{1}{2} log\left[\frac{I_0}{(I_- + I_-)\,|^{\xi=0}}\right]. \end{aligned} \tag{5.36}$$

To deterimine the phase component,

$$\left.\frac{1}{k}\frac{\partial \phi}{\partial \xi}\right|^{\xi_s} = -log\left[\left.\frac{I_- - I_+}{I_- + I_+}\right|^{\xi_i=0} \sinh\left(\left.\frac{\partial A}{\partial \xi}\right|^{\xi_s} L\right) + \cosh\left(\left.\frac{\partial A}{\partial \xi}\right|^{\xi_s} L\right)\right] \frac{z_0 z_1}{2\frac{\partial A}{\partial \xi}|^{\xi_s} z_0 z_1}. \tag{5.37}$$

For small x, $\sinh(x) \approx x$, $\cosh(x) \approx 1 + \frac{x^2}{2}$, and $\log(1+x) \approx x$, equation (5.37) is reduced to

$$\left.\frac{1}{k}\frac{\partial \phi}{\partial \xi}\right|^{\xi_s} = -\left[\left.\frac{I_- - I_+}{I_- + I_+}\right|^{\xi_i=0} + \frac{1}{2}\left.\frac{\partial A}{\partial \xi}\right|^{\xi_s} L\right] \frac{L(z_0 + z_1)}{2 z_0 z_1} \tag{5.38}$$

as and is valid long as the terms inside the cosh and sinh functions are less than 0.5. If the absorption coefficient of the refractive index is zero (*ie.*, β=0), the above gradient of the phase equation comes is in the very simple form

$$\left.\frac{1}{k}\frac{\partial \phi}{\partial \xi}\right|^{\xi_s} = \left.\frac{I_- - I_+}{I_- + I_+}\right|^{\xi_i=0} \frac{L(z_0 + z_1)}{2 z_0 z_1}. \tag{5.39}$$

Experiments were performed at the SYRMEP beamline to validate this formalism following the schematics shown in Figure 5.6. The sample stage was approximately $22m$ from the apparent X-ray source. A 20-μm slit was used as a pre-sample aperture (L), and a single-edge for the detector aperture was translated to achieve I_- and I_+ configurations. With the edge in place in front of the detector, the Picasso pixel recorded around 4.5×10^4 cps. Data were acquired at 770 vertical scan positions for each configuration. A 10μm scan step was employed at 1 second per frame. Five wires made up of different materials as shown in Figure were imaged and their properties are outlined in Table 5.1.

The image in Figure 5.7 illustrates the data acquited during the experiment with wires arranged in the same succession as in Figure 5.8. One acquisition is represented by each pixel row for a vertical position in the sample. Each of the images were normalised by the mean pixel values from a flat field are taken from each boxed region indicated in blue. The image displays a transition from strong absorption to strong phase contrast *ie.* from Aluminum to Boron. Figure 5.9 presents intensity profiles along a single column from

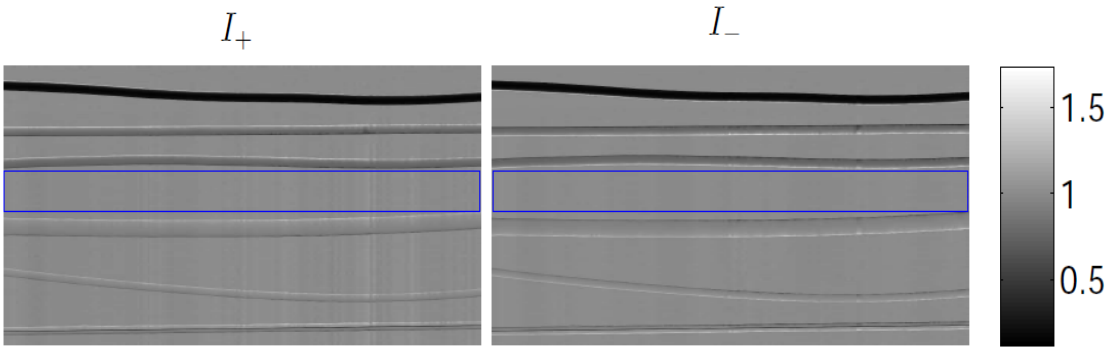

Figure 5.7: Images of the wire samples acquired in I_+ and I_- configurations. They are presented in the order according to Table 5.1, the topmost being wire A. See also Figure 5.8

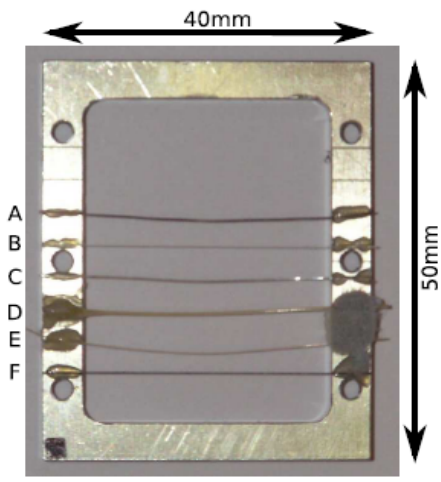

Figure 5.8: Photograph of the wires used in the experiment. They are labelled A-F with corresponding properties indicated in Table 5.1

both images and a plot of their sum. The absorption behavior of wires D, E, and F demonstrates anomalous behaviors as manifested by the peaks. The reason could be that a slight deviation in alignment existed as the two images were obtained in two different scans. This misleading absorption behavior however does not impact the phase properties given by I_- and I_+.

Figure 5.10 are images of A and $\frac{1}{k}\frac{\partial\phi}{\partial\xi}$ that were determined from datasets used for Figure 5.7 using equations 5.36 and 5.37. It shows that all wires are resolvable in the image with phase-effects while only wires A, B and C are resolvable in absorption image.

The extracted phase gradient is shown in Figure 5.11. The presence of a spike in the Boron filament's plot indicates the presence of an inner core of higher density. In fact, a 5-*micron* Tungsten core does exist inside the wire. The extracted values were compared with the analytic value for $\frac{\partial\phi}{\partial\xi}|^{\xi_s}$.

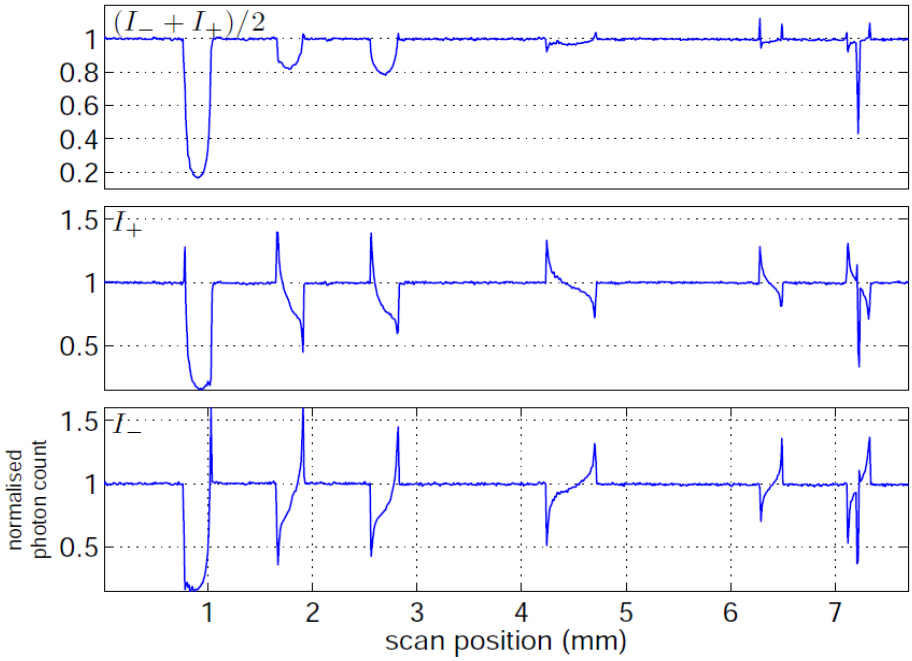

Figure 5.9: Vertical profile for one pixel column for $(I_- + I_+)/2$, I_+ and I_-

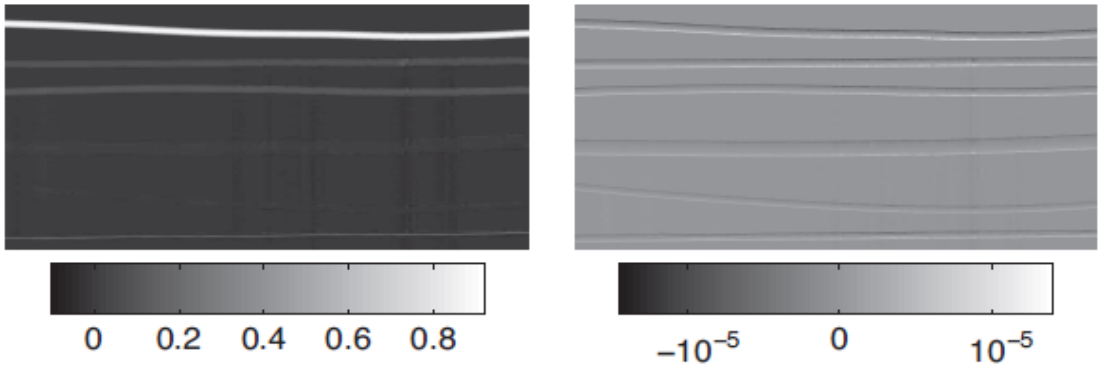

Figure 5.10: Absorption (left) and $\frac{1}{k}\frac{\partial\phi}{\partial\xi}$ (right) derived from Figure 5.7.

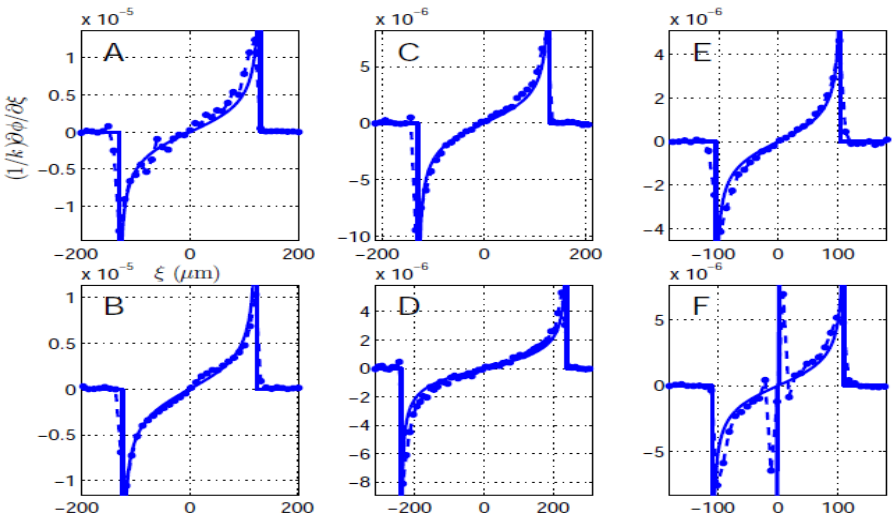

Figure 5.11: Extracted phase gradient(broken line) and the theoretical value(solid line for each line)

We have seen in the above example with wire filaments that edge-illumination technique is a powerful tool to describe not only absorption properties of a sample but also its phase properties. We have also seen that with the phase information, edge-enhancement is achieved. We also have attempted to test the protocol with the Picasso detector on mastectomy specimens. The studies presented here were performed at the SYRMEP beamline.

Longo [123] performed a simulation on the behavior of contrast as a function of pre-sample aperture opening (L) and of IPF (illuminated pixel fraction). The contrast decreases as L increases. Moreover, the contrast decreases as the IPF increases. The plot of the contrast behaviors for a 200-*micron* PEEK filament at $20keV$ at z_0=23 m and z_1=1.5 m are depicted in Figure 5.12.

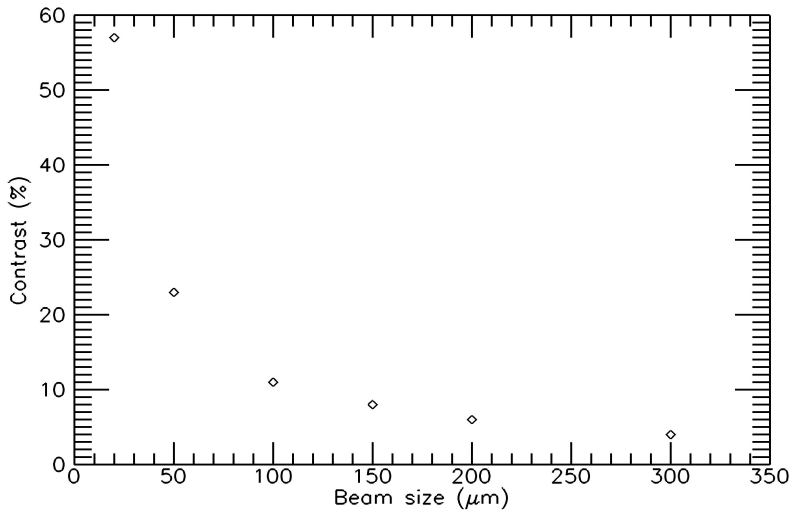

(a) Contrast as a function of pre-sample aperture

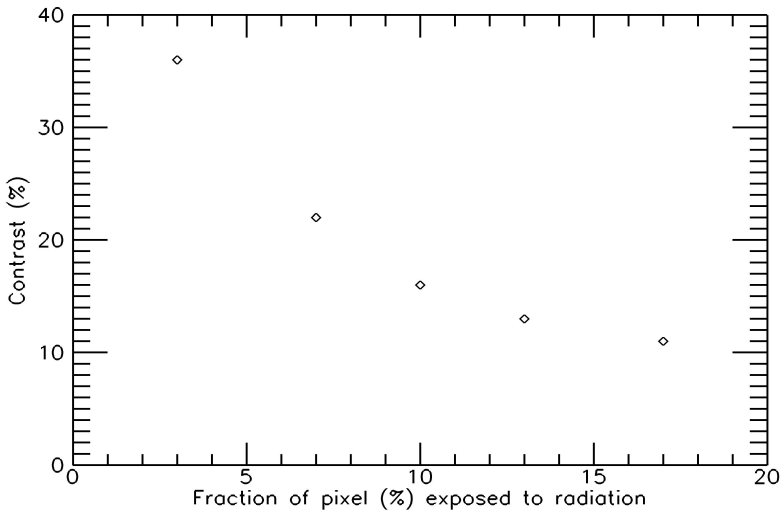

(b) Contrast as a function of illuminated pixel fraction

Figure 5.12: Influence of the size pre-sample aperture and IPF on the contrast [123]

To reach a clinical set-up that is physically reasonable in terms of contrast but also practical in terms of set-up allignment and complexity, a compromise has to be set. The size of the beam can not be brought down too low in order to have sufficent photons hitting the detector so that fast acquisition time maybe performed. Putting these considerations, we have set the vertical aperture of the pre-sample slit to 100 μm and half of this opening illumunates one pixel of the detector. This means that we have 17% IPF, considering that the Picasso sensor height is 300 μm. As with the wires discussed above, I_- and I_+ set-up was also employed in order to perform the phase-retrieval protocol.

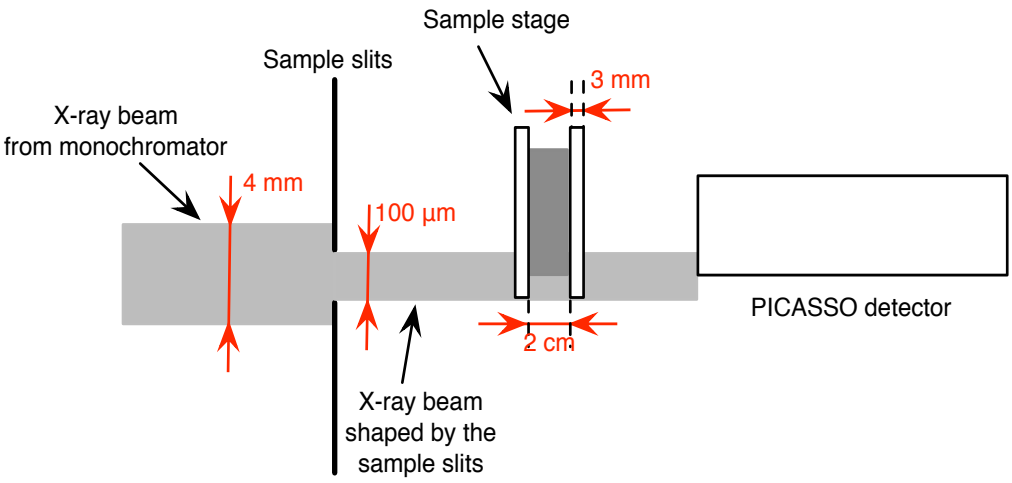

(a) I_+ configuration

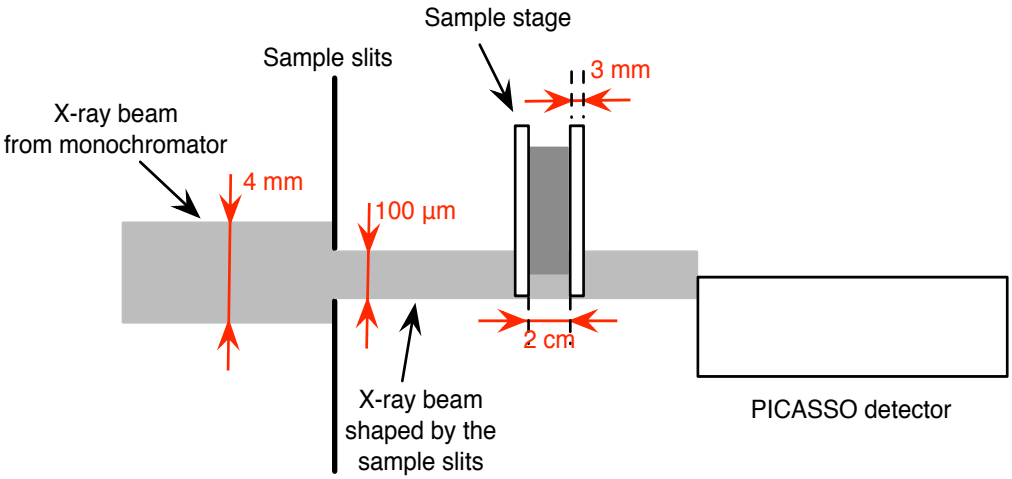

(b) I_-configuration

Figure 5.13: A simplified Coded-aperture phase contrast imaging set-up used for breast tissue imaging acquisition in the I_+ and I_- configuration

A schematic view of the set-up is presented in Figure 5.13 to describe the experimental set-up used for the edge-illumination imaging with breast tissues. In this set-up, z_0 is 23 m and z_1 is 1.5m. The slit opening is 100 μm as in the simulation by Longo [123], and the detector was put on *edge-on* configuration. The detector was shifted vertically to achieve I_- and I_+ as shown. For the absorption method, z_0 is 24 m and z_1 is 7 cm.

The breast samples were prepared from specimens of total mastectomy and were derived from surgical material sent to the Pathology Unit of the University Hospital of Trieste (Italy) according to local guidelines. One of the specimens was not fixed with formalin and immediately imaged at the SYRMEP beamline. This sample contained a ductal carcinoma, tumor grade G2. The other sample was fixed in formalin and stored at room temperatre. It contained an invasive ductal carcinoma with tumor grade G2-3. Both specimens were 2 cm in thickness and were sealed in vacuum bags mounted between two plexiglass supports. The unfixed sample was imaged with 20 keV while the formalin-fixed sample was imaged at 17 keV, 20 keV, 23 keV, and 26 keV. The samples were scaned across the beam at different energies maintaining a surface dose of 1mGy per exposure. This was done by modifying the scan velocity for each energy.

The images were acquired in I_- and I_+ configurations as well as retrieved images which maps the

absorption A integrated over the sample, and the differential phase $\frac{1}{k}\frac{\partial\phi}{\partial\xi}$ herein presented. Figure 5.14 lays out the images of the non-fixed specimen. Some artifacts may be noted, mostly due to the air bubbles trapped inside the bag enveloping the specimen.

Figures 5.15, 5.16, 5.17, and 5.18 show the images of the fixed specimen at different energies. Artifacts (horizontal stripes) are noted probably due to the beam instability at the time of the acquisition.

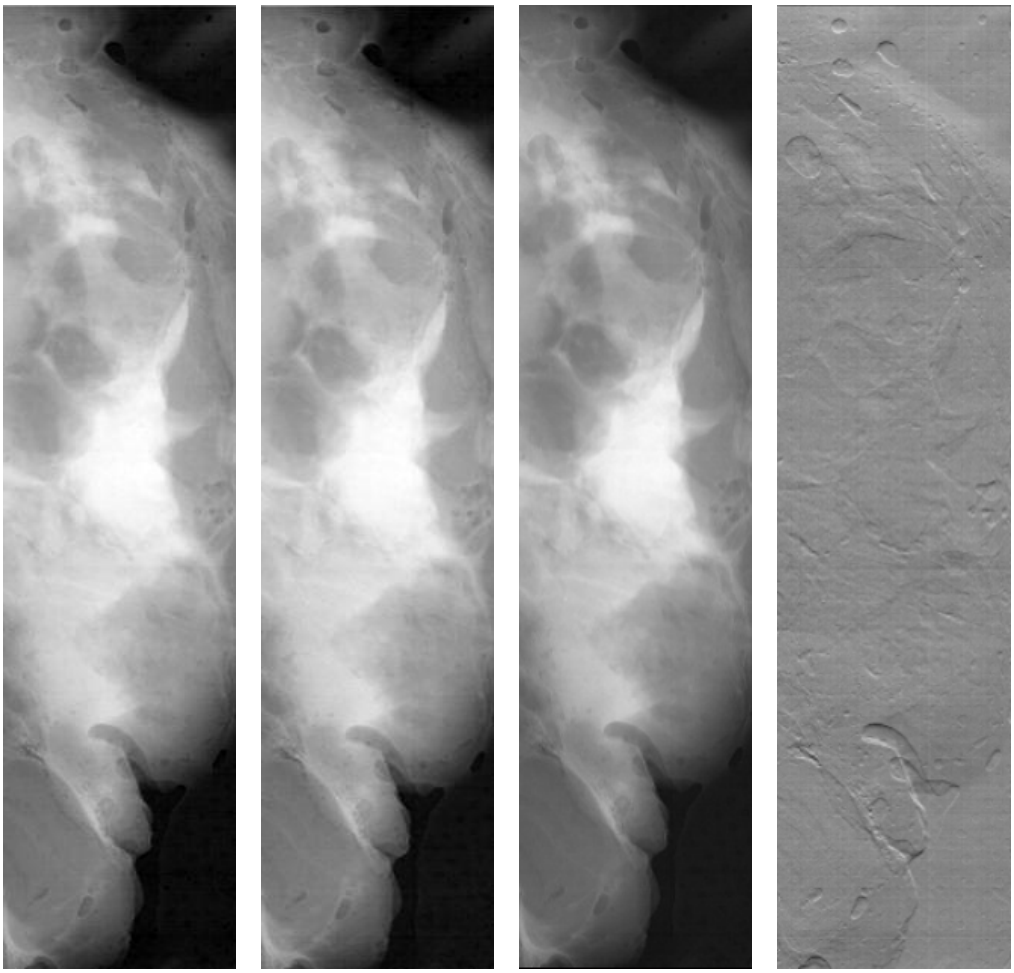

$(a)\ I_+$ $(b)\ I_-$ $(c)\ Absorption$ $(d)\ \frac{1}{k}\frac{\partial\phi}{\partial\xi}$

Figure 5.14: Images of the non-fixed breast specimen taken at 20 keV.

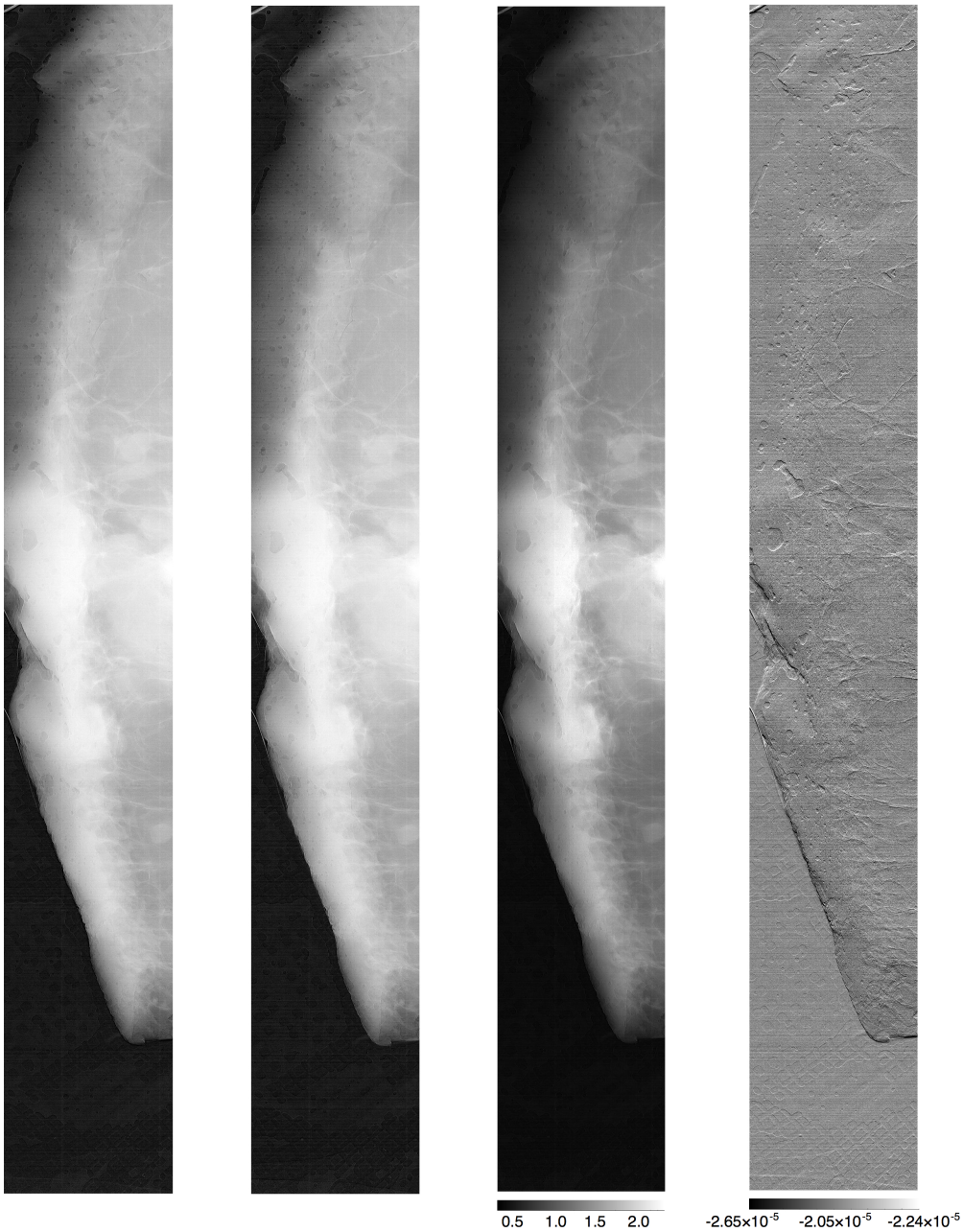

$(a)\, I_+$ $(b)\, I_-$ $(c)\, Absorption$ $(d)\, \frac{1}{k}\frac{\partial \phi}{\partial \xi}$

Figure 5.15: Images of the fixed breast specimen taken at 17 keV.

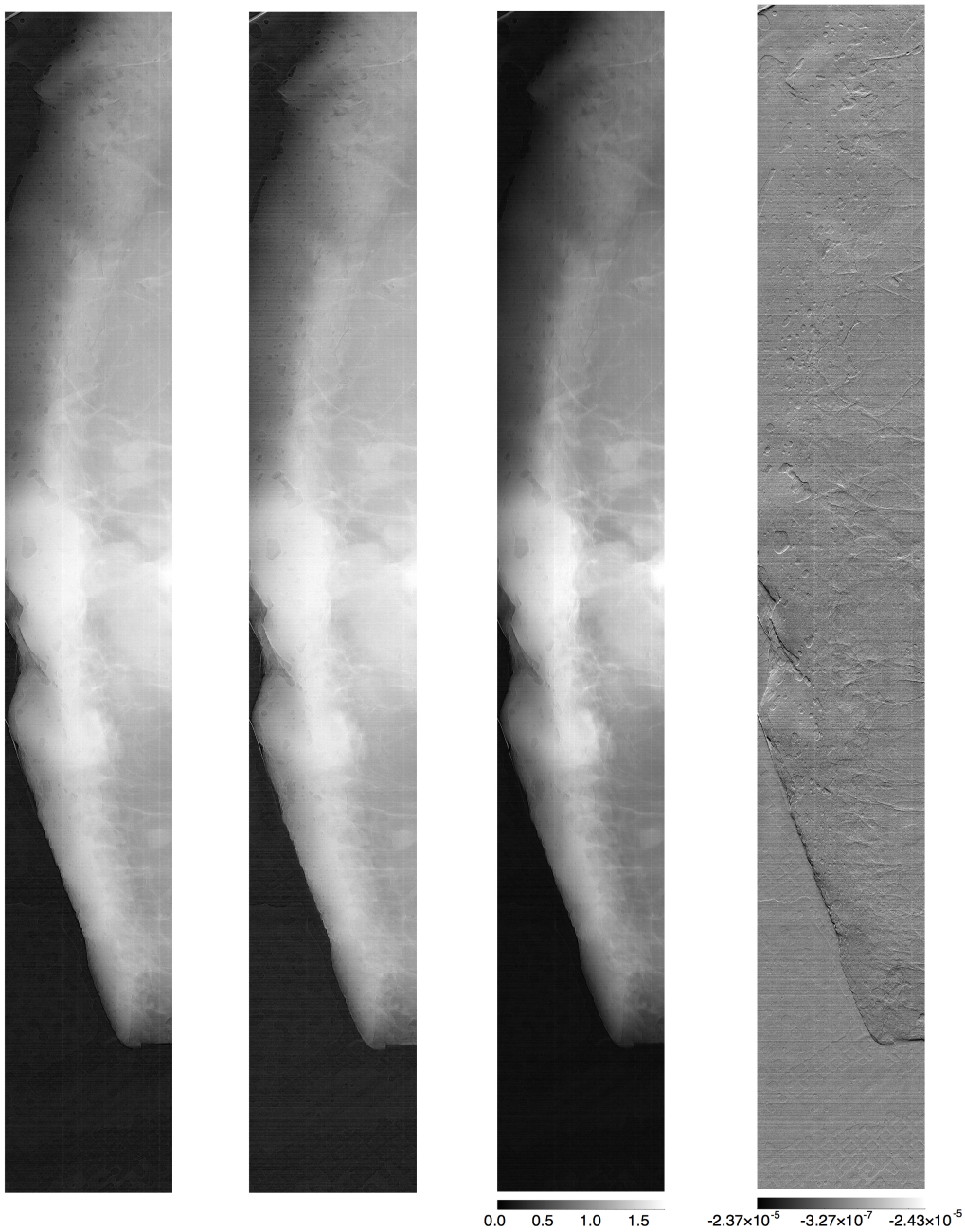

$(a)\, I_+$ $(b)\, I_-$ $(c)\, Absorption$ $(d)\, \frac{1}{k}\frac{\partial\phi}{\partial\xi}$

Figure 5.16: Images of the fixed breast specimen taken at 20 keV.

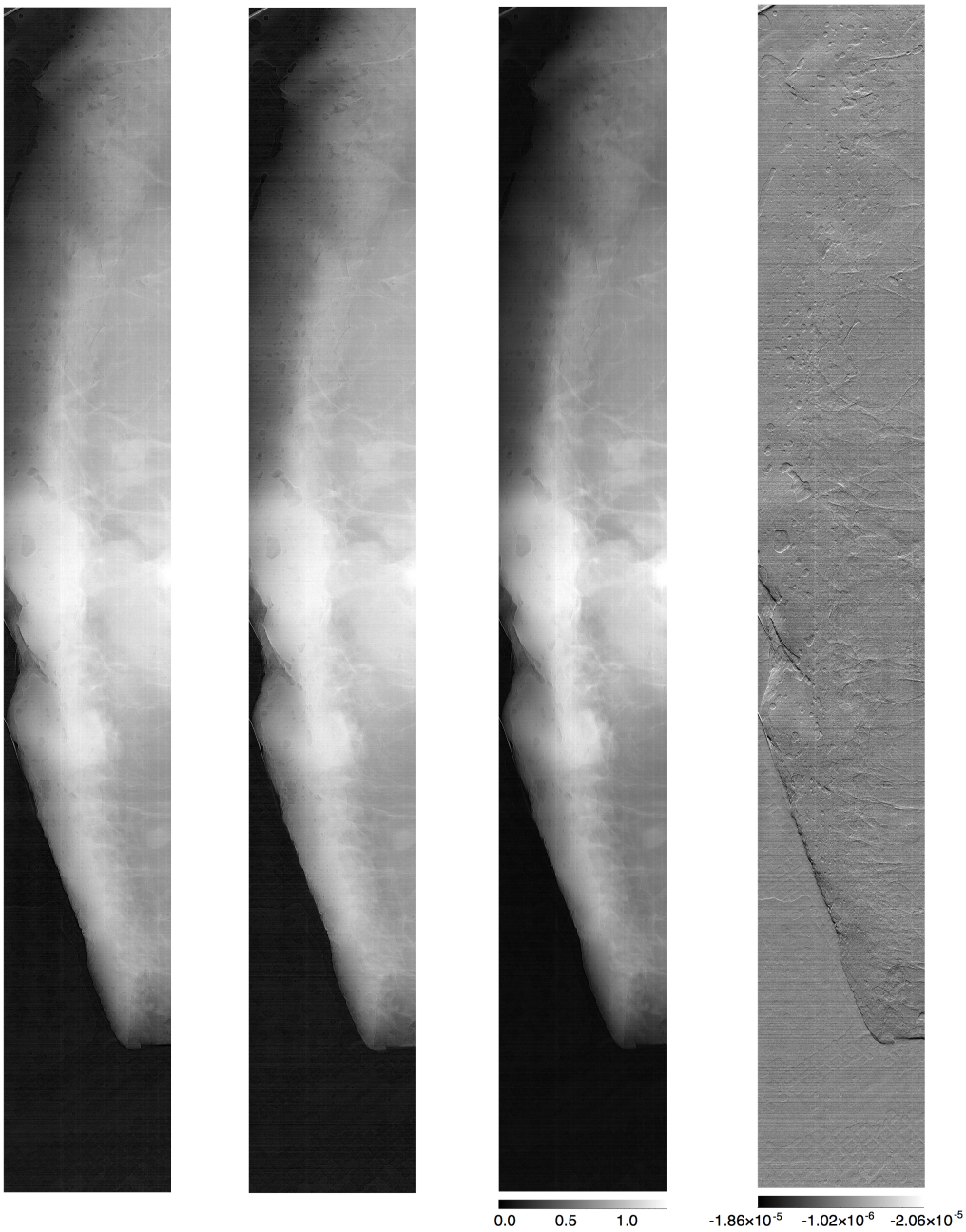

$(a)\ I_+$ $(b)\ I_-$ $(c)\ Absorption$ $(d)\ \frac{1}{k}\frac{\partial\phi}{\partial\xi}$

Figure 5.17: Images of the fixed breast specimen taken at 23 keV.

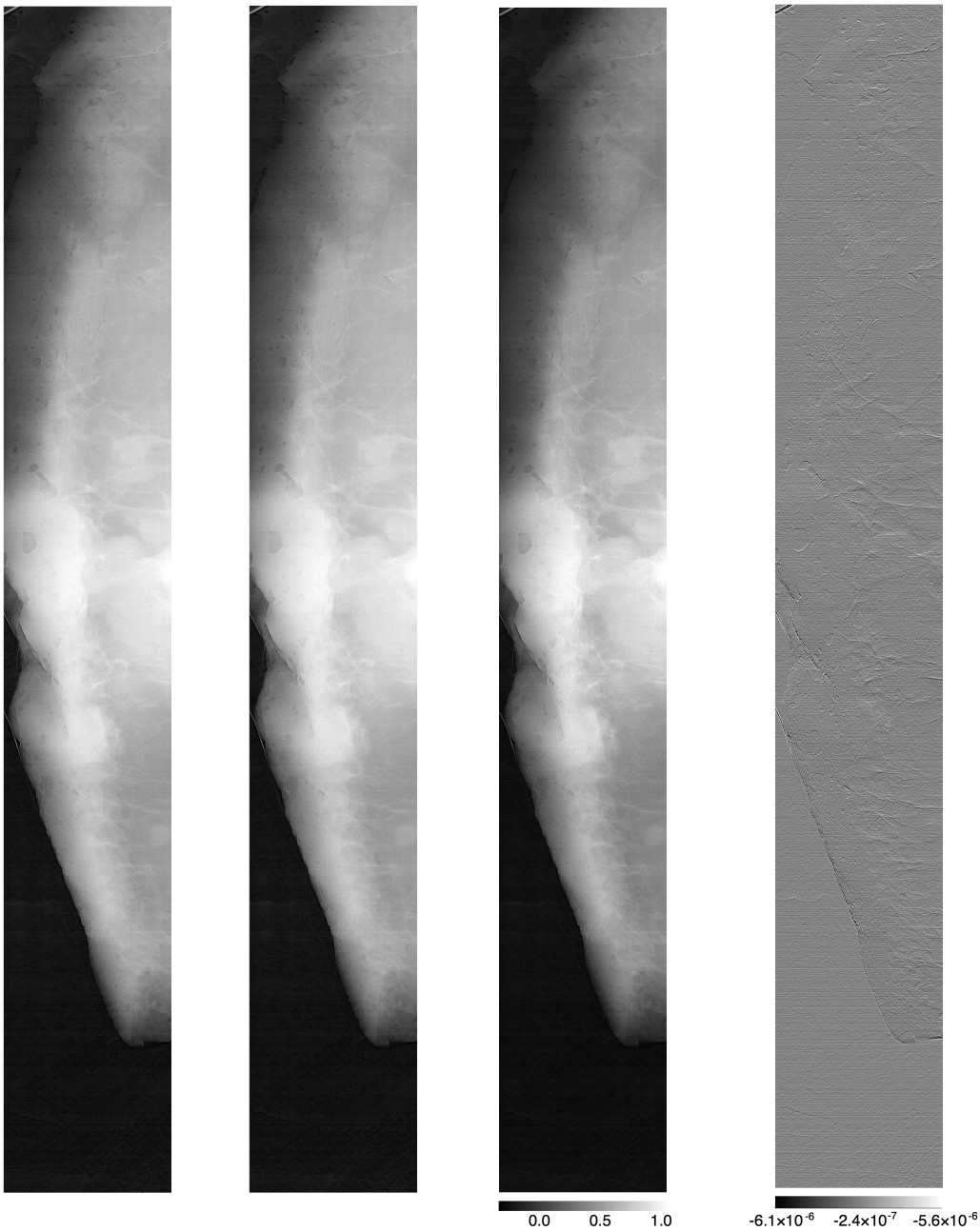

$(a)\, I_+$ $(b)\, I_-$ $(c)\, Absorption$ $(d)\, \frac{1}{k}\frac{\partial \phi}{\partial \xi}$

Figure 5.18: Images of the fixed breast specimen taken at 26 keV.

A region of interest was chosen in the on the acquired images for absorption and $\frac{1}{k}\frac{\partial\phi}{\partial\mu}$ represented in Figure 5.19 and the profiles for the different energies also presented (Figure 5.20). The value for the absorption decreases with energy. The same behavior is noted with phase. Also, we can infer that the contrast we can extract from Figure 5.20 are strongly energy dependent and they decrease with energy which is partialy due to the δ term

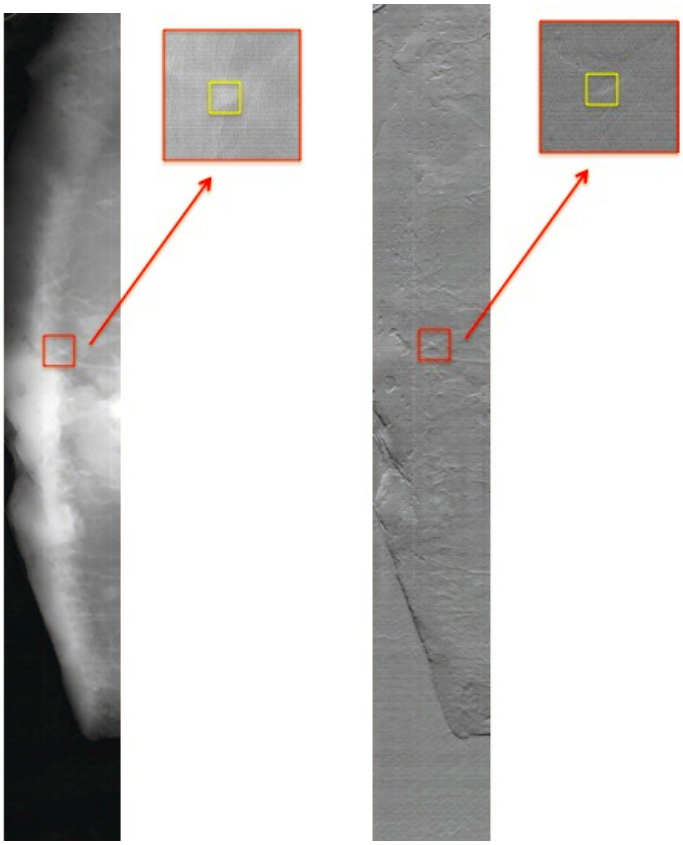

(a) *Absorption* (b) $\frac{1}{k}\frac{\partial\phi}{\partial\xi}$

Figure 5.19: Regions of interest from absorption and differential phase images acquired at 20 keV.

However, it is notewothrthy to evaluate the sensitivity of the system for what concerns discrimination of small deviation angles. We have seen that failure starts to be aparent at highrer energies. In Figure 5.21, the deviation limits are shown for two energies for configurations I_+ and I_-. The likelihood that a photon creates a positive and negative peak is higher for 20 keV compared to 26 keV. We say that at 20 keV, the peaks or rises more intensely than at 26 keV, hence affecting the $\frac{1}{k}\frac{\partial\phi}{\partial\xi}$ images. This describes the decrease of contrast with energy.

Futher reduction of contrast is met based from the PSF characteristics of the detector. Looking forward at Figure(6.7) in Chapter 6, PSF is not a perfect box function. This flaw affects the images taken with our simplified set up, hence absorption and $\frac{1}{k}\frac{\partial\phi}{\partial\xi}$. For the different wires however, imaging was performed with a detector mask that shapes the detector pixel, thus avoiding the tails of the PSF. The edges of the PSF inefficiently counts the refracted angles and the non-symmetry distorts the phase retrieval algorithm.

Given these limitations, the absorption and the differential phase images may be slightly degraded. It would be interesting to expand the phase-retrieval method and include these limitations to understand the appropreate corrections that may be applied for ease of implementation in simplified set-ups. In terms of dose, the width of beam not hitting the detector may be reduced in order to achieve a low dose as resonably as possible. That is, a balance must be set between the delivered dose and the signal-to-noise ratio.

Notwithstanding the given limitations, our group was able to validate phase-contrast imaging by implementing *edge illumination* coded-aperture technique assuming a point source, both for pre-sample plus detector apertures with the wires and a more simplified set-up for the breast with the Picasso detector. This linear array detector was able to demonstrate that with even a demanding set-up as mentioned, experimen-

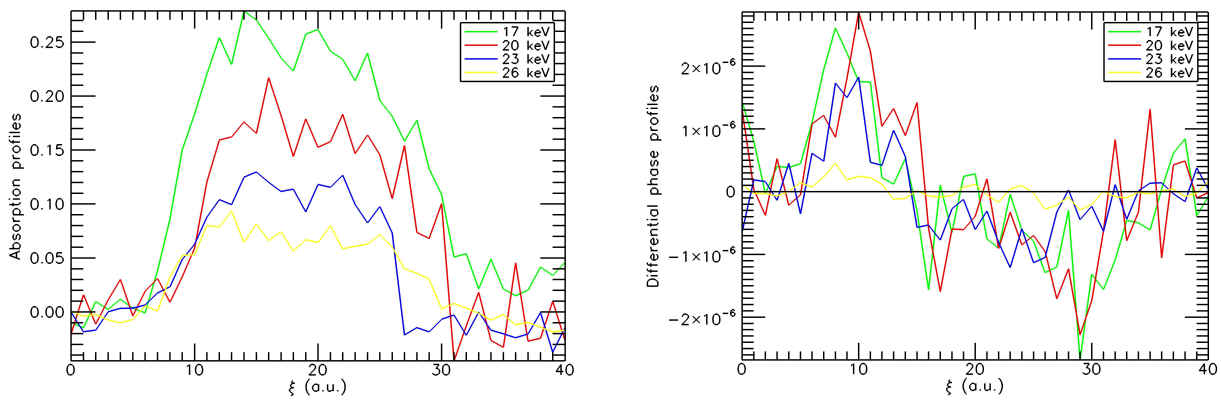

(a) *Absorption* (b) $\frac{1}{k}\frac{\partial\phi}{\partial\xi}$

Figure 5.20: Retrieved absorption and phase profiles of the ROI indicated in Figure 5.19 at the different energies.

tally determined phase gradients matched the theoretically expected results quite closely.

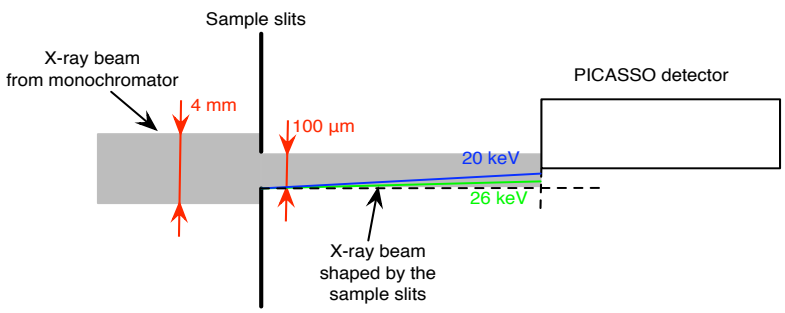

(a) Bottom side

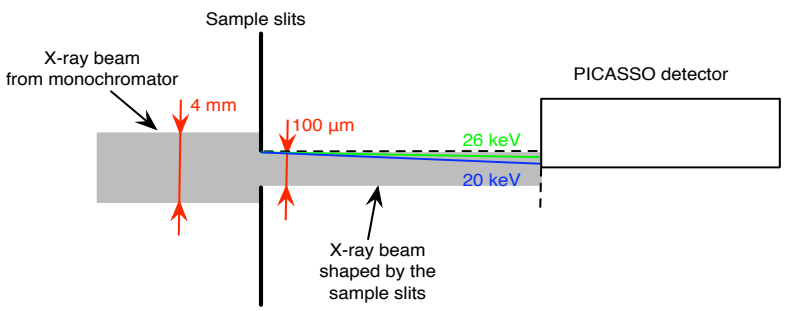

(b) Bottom side

Figure 5.21: Angle deviation limts for 20 keV and 26 keV

Chapter 6

PICASSO four-layer assembly: first results

The final assembly consisting the four layers of the Picasso detector was completed during the third quarter of 2012 and was tested with photons for the first time in November 2012. In this chapter, the final assembly is going to be introduced. The process of synchronizing the four layers will be discussed. The average horizontal and vertical pixel dimensions of the sensors has been estimated puting into consideration the rigid design of the layers. Further, the images acquired with the system will also be presented.

6.1 The PICASSO four layers

The mounted layers of the final Picasso assembly is shown in Figure 6.1 and work in the principle presented in Figure 3.2. The front and back Alimunum frames that holds the boards, separated by 180 *mm*, are mouted in a resin-based aluminum box.

The front layers are controlled by one controller, while the back detectors are controlled by another. The stream of data generated by each detector couple are independently put on queue to the switch and timestamped accordingly. See Figure 6.2. The receiving acquisition PC provides a separate buffer for data coming each remote Picasso device, and appends the data for each frame before encoding them to disk.

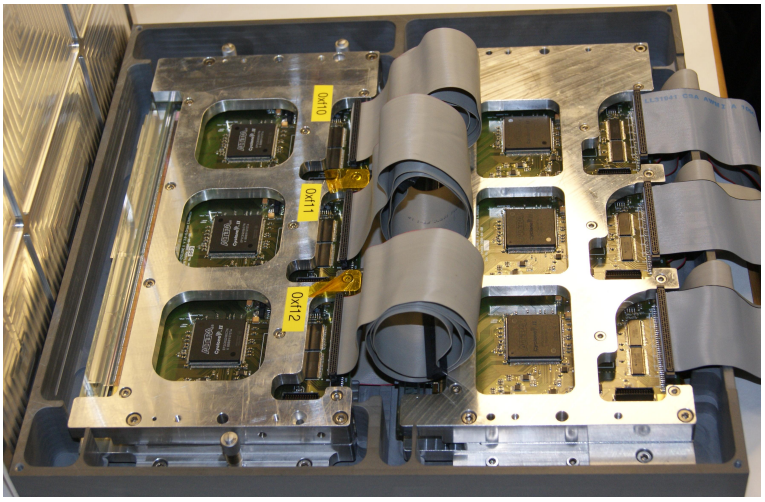

Figure 6.1: All four layers mounted together in its protective box.

6.2 Synchronization

There are two ways that one can communicate with the detector using the upgraded software:

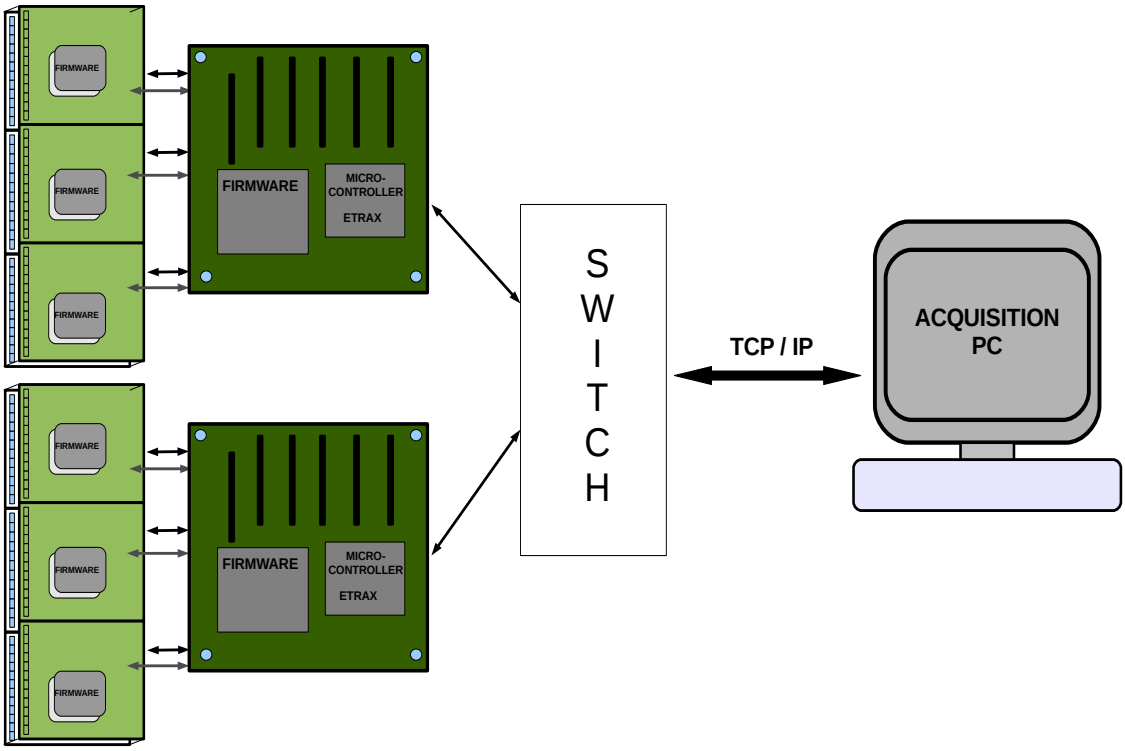

Figure 6.2: The architecture of the Picasso four-layer architecture. One controller handles one Picasso couple while the other controller controls the other couple.

1. **multiDetector class**

   This class is represented by the two or more controllers which operate simultaneously with the same input parameters common to the detector. In this class, it is possible establish or define more than one detector system. In order to have the acquisition PC recognize the packets sent by each controller's ethernet device, each controller must be assigned a unique IP address that also must be indexed differently. The detectors are ordered in such a way that the indexing starts with 0, and that means that the data will be written to disk according to how the index are ordered. In other words, the controller that is indexed 0 is the master, and the remaining controller is the slave. In this mode, the data is written to disk based on master-slave architecture where data from the slave controller is concatenated with the data from the master controller. Important parameters such as number frames, exposure time, dynamic range, energy threshold settings and clock settings which must be set identical for both controllers is immediately taken care of this class without indexing each of the controllers separately. This definitle saves time during initialization. The *acquire* command is also given once without separate indexing and acts on the controllers at the same time. It is handy to use this class as it takes care of the master and slave simultaneously.

   A simple schematic diagram is illustrated in Figure 6.3. The detector controllers are the *multiDetector* servers that are initialised by the *multiDetector* class. The Picasso client is actually the Picasso acquisition PC that is handled by the user. It is also where the data is written an post-processed.

2. **picassoDetector class**

   This class is represented by a single controller. Here, several detectors are defined by indexing them individually using unique assignments for each controller. The difference between this class and the *multiDetector* class is that in the former, control parameters are fed individually while the later, indexes are automatically assigned to the detectors contained in it. *picassoDetector* class is particularly useful for debugging purposes if one wishes to understand the problems arising from each controller.

Delay between controllers has been monitored in our laboratory by connecting one of the output lemos of the board to an oscilloscope. Currently, the delay between the two device is around 750 μs. A sample waveform from each controller is presented in Figure 6.4.

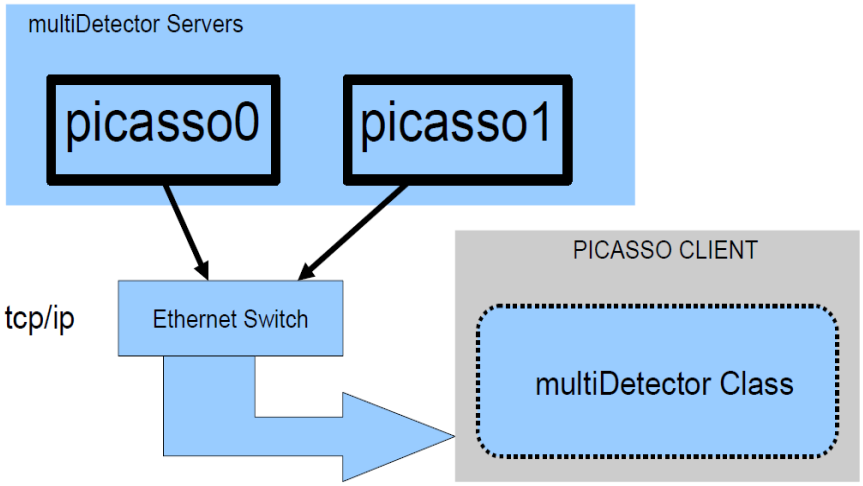

Figure 6.3: A *multiDetector* class working together simultaneously

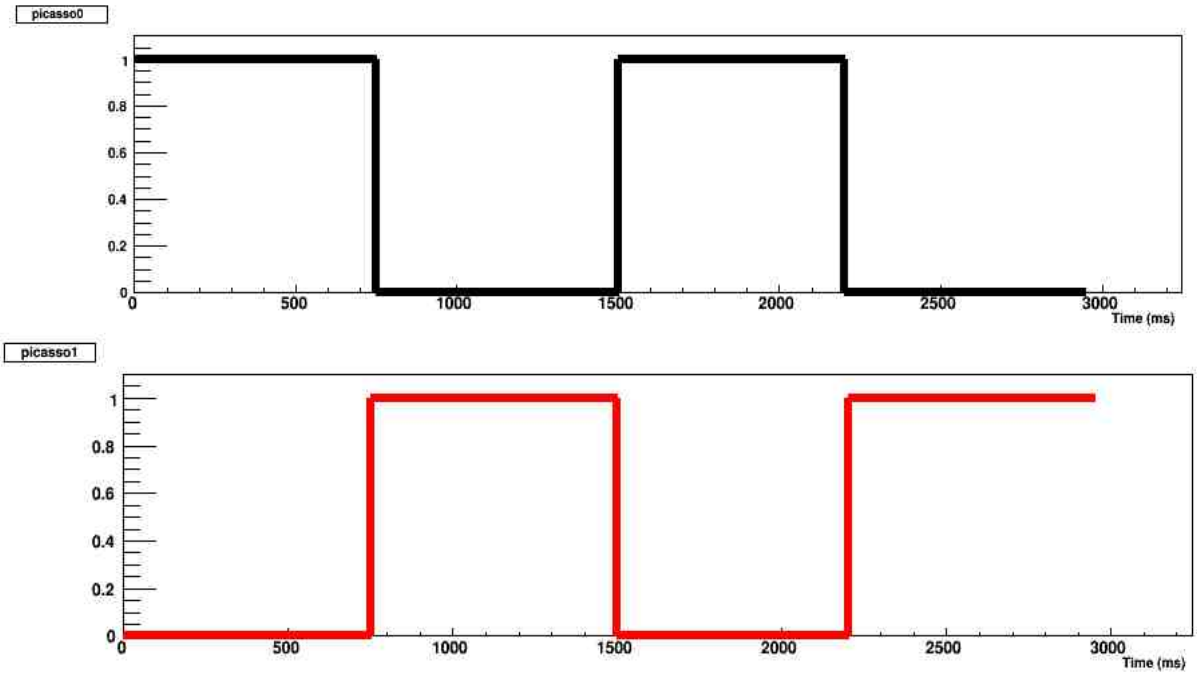

Figure 6.4: Delay between frames between the two controllers.

6.3 Sensor vertical alignment and pixel size

6.3.1 Vertical PSF

Before releasing the detector used for routine imaging, it is important to understand if the pixels can be well illuminated considering the rigid clearance of the sensor spacing. The mechanical mounting of the Aluminum frames in the protective box can very well affect their separation. By design, two high-precision micrometric screws are mounted in the front detectors. These screws were meant to enable adjustment between the frame separation, *ie.* increase or decrease the distance between them, and consequently the sensors. By design, the sensor lay-out along the beam's path is depicted in Figure 6.5. To achieve a full illumination along the pixel height, a separation of 800μm and 100μm between the front sensors and back sensors are needed, respectively.

The preliminary check of the vertical distcances between the sensors has been evaluated with the use of X-rays. This excercise was performed at the experimental hutch of the SYRMEP beamline. This hutch offers only 14cm of beam width, as opposed to our detector which has a width of 21cm. The detector therefore received partial illimination at a time.

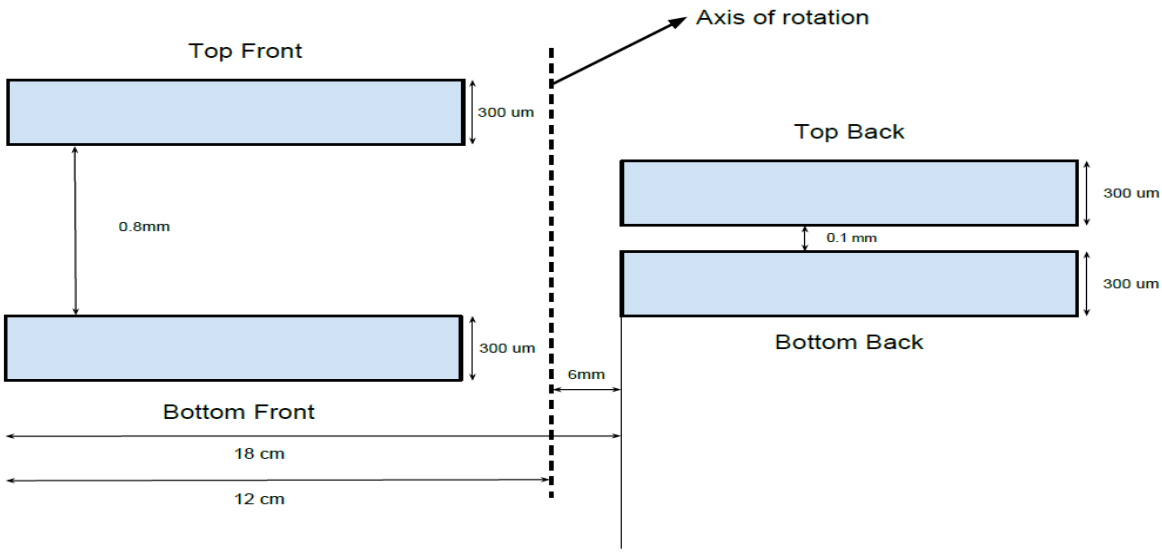

Figure 6.5: The sensor lay-out (as per design) of the Picasso detector

The geometry of the four-layers has been assessed by scanning a Tungsten edge in front of the detector. As an intial procedure, the system was alligned with the beam to give the maximum illumination possible. Thereafter, the horizontal edge was scanned vertically producing an edge-spread function (ESF) [124] for each pixel. The line-spread function (LSF) of each pixel was calculated by taking the derivative of the ESF, and the full-width at half maximum (FWHM) is the sensor thickess. Presented in Figure 6.6 is a 2D histogram of the LSF of the illuminated pixels. This histogram is also known as the *detector footprint*.

Among the challenges met with the design as can bee seen in Figure 6.6 and Table 6.1, is penumbra. The front detectors are casting a shadow on the back sensors (see especially Back Bottom layer). This means that the distances between the sensors has not been met that required us to return the detector for review of the mounting.

Sensor	Thicknes
Top Front	298 μm
Bottom Front	295 μm
Top Back	288 μm $^{(**)}$
Bottom Back	119 μm

Table 6.1: The average measured thickness of the illuminated sensors of the four-layer Picasso detector. $^{(**)}$The Top Back layer has been partially cut by the PCB of the Front Top detector.

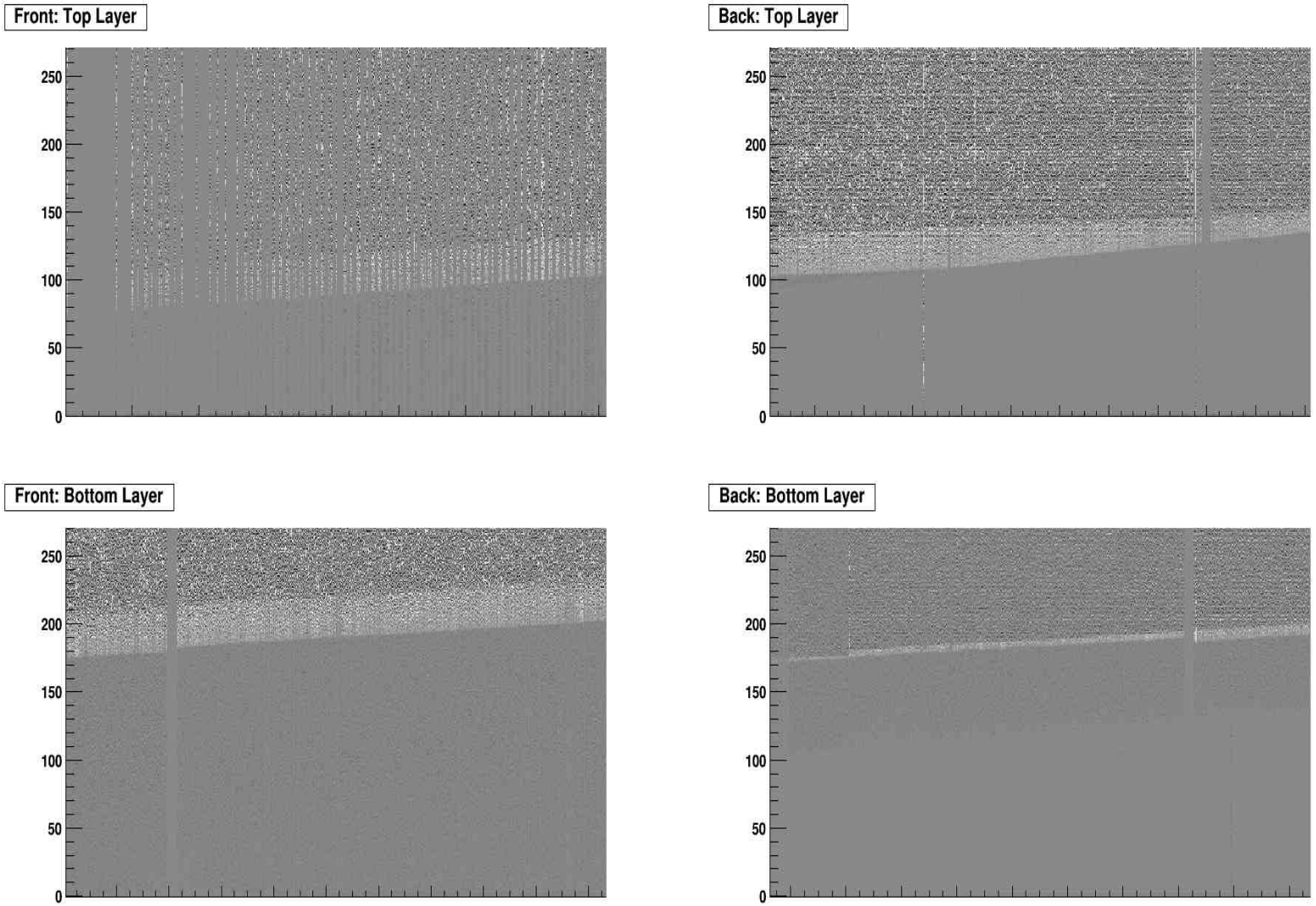

Figure 6.6: Footprint of the sensors of the Picasso detector. The sensors at the back detector are partially covered by the front detector board. The sensors are slightly slanted due to the misalignment in the roll direction.

6.3.2 Horizontal PSF

In a slighly different procedure, the pixel width was also evaluated by way of LSF as above. This time, the detector was translated horizontally accross the beam at a step of 2 μm with a bar pattern test object in front of it. The bar pattern test object has several openings, but in our case only selected apertures were chosen so that the aperture's edge is coincident with a pixel's edge at the first detector position. At each step, a threshold scan was collected. As the detector is translated, the illuminated pixel fraction increases, consequently the photon counts increases as already shown a similar study previously performed with Picasso [125].

Ideally, the PSF of a photon counting detector resembles a box function with the width given by the pixel size. This function becomes a deformed isosceles trapezoid due to the influence of charge sharing and of electronic noise. Figure 6.7 presents the horizontal PSF of the PICASSO detector obtained at $25keV$ and $20keV$. It compares the ideal PSF of the 50-μm pitch detector devoid of charge sharing and noise presented by the black dashed line, and the PSF of the detector at different comparator threshold settings presented in colored solid lines. As we can see, the area under the curve increases with the increase in comparator threshold, and the aparent width of the pixel also increases. The reason for this is that the a single event caused by a charge is encoded in the two neighboring strips. On the other hand, an important event in the pixel may not be counted at all if the amplitude of threshold is set too low againts the the set comparator discriminator for a given photon energy. This may be elaborated in Figure 6.8 where the figures show the composite PSF for three neighboring channels. For 25 keV for instance, the composite PSF is more than 100% for $430DACu$ and $450DACu$, exceeding in fact the theoretical PSF (hence the theoretical pixel width) while the PSF is reduced in the other threshold values presented, indicating a reduced effective pixel size. In both extreme cases, the spatial resolution is degraded. Demonstrated here are data from the bottom layer of the front detector that was reasonably illuminated, with less dead channels with respect with the top layer.

Since the spatial resolution for microstrip detectors is highly non-uniform as it is highly dependent on the event point (position where the photon was absorbed) with respect to the strip center [126], the FWHM of the PSF is often not adequate to assess the spatial resolution. In the case of a trapezium, the FWHM represents the strip pitch of the sensor like that of the box function but the full width (maximum residue) of the PSF results to the sum of the ideal pitch and a length we will define Δ, which is half of the difference between the two parallel sides of the trapezoid. For our detector, the maximum residue results to around 80 microns.

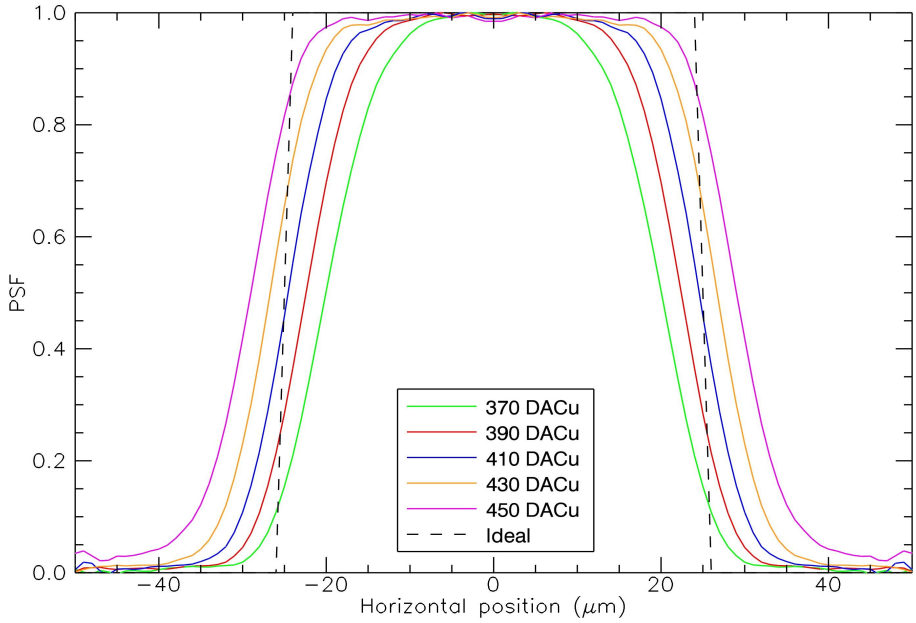

(a) 25 keV.

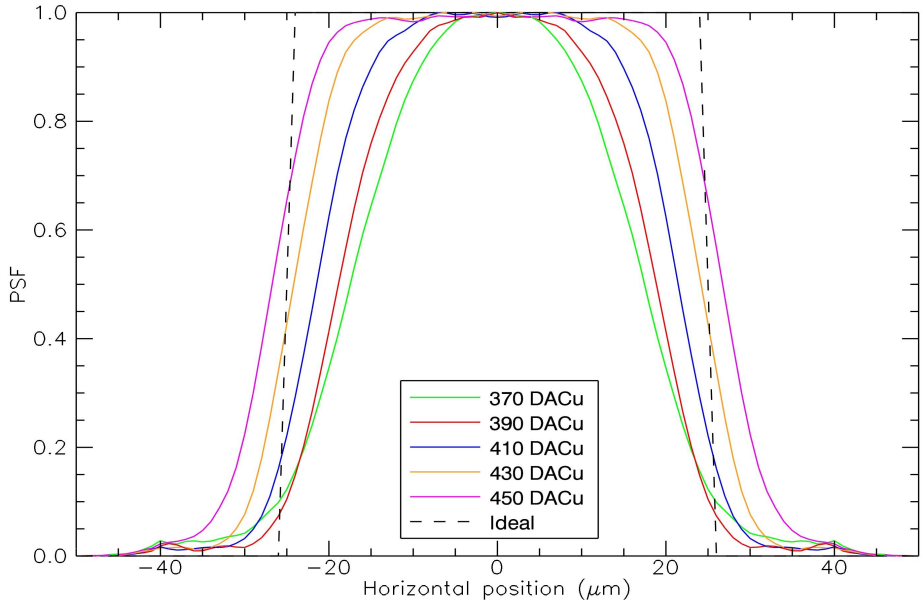

(b) 20 keV.

Figure 6.7: Point spread function of the Picasso detector various energies

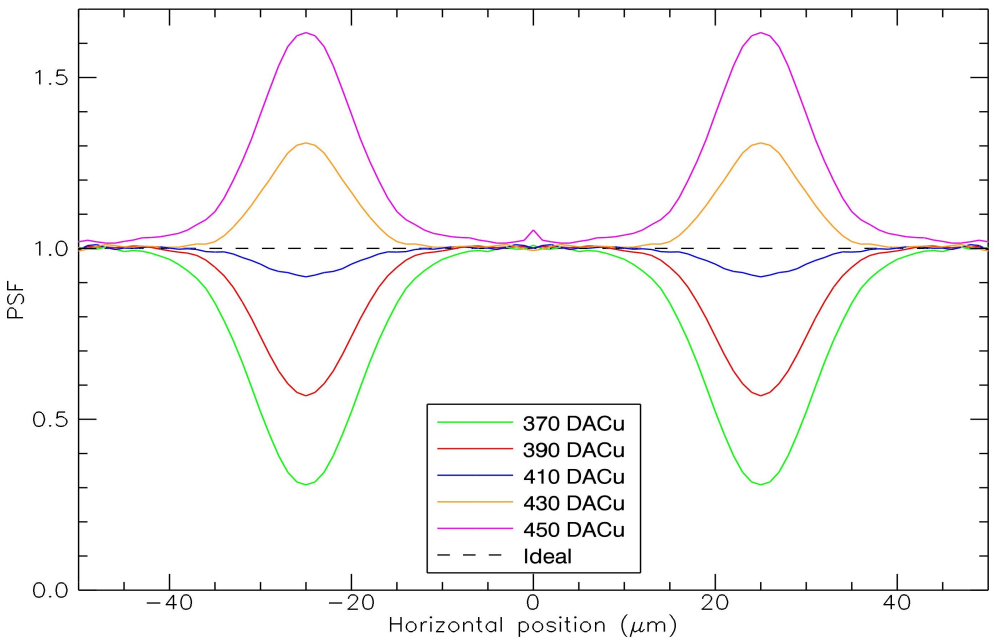

(a) 25 keV.

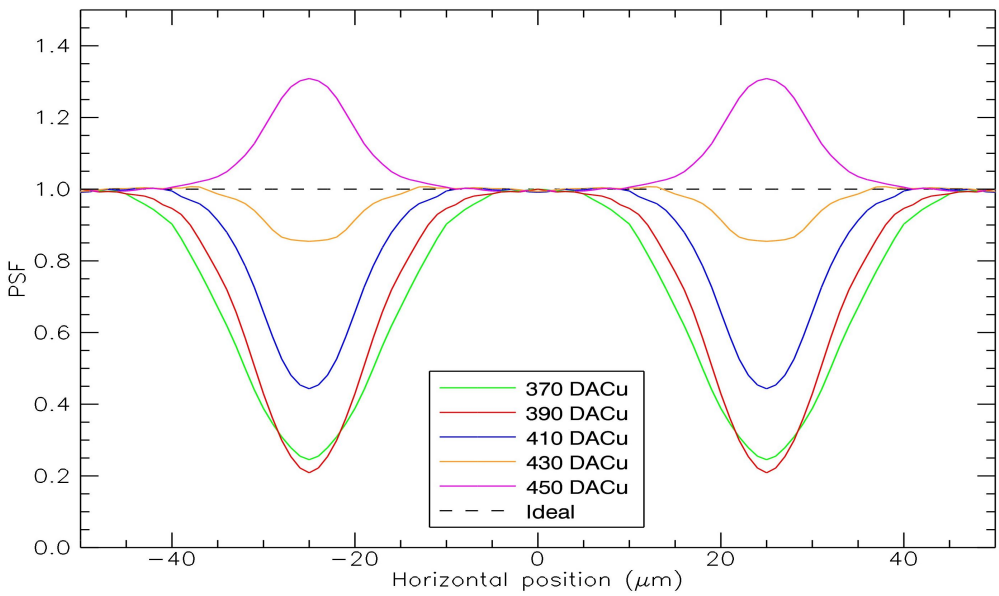

(b) 20 keV.

Figure 6.8: Composite point spread function from three neighboring pixels

6.4 First images with the four-layer Picasso detector

Nevertheless, considering the principle of the design of the detector, it is possible to generate a single image coming from the four layers by fusing the images generated by each, resulting to the image presented in Figure 6.9e. This was achieved by creating an matrix array alligning the data from the pixels which are in the same vertical position in space, then taking their average. See in the same figure for instance that the Top Front layer is heavily damaged. Several channels are dead as can be seen in the black vertical stripes. In cases where flat field and dead channel corrections are difficult to apply, the value for the missing channel in the column was compensated by a valid value from one of the elements of the column array. In this figure, an image of an RMI 160 Ackerman phantom that measures $10cm$ vertically and $8cm$ horizontally, is presented. It was acquired in the vertical direction using a continous scan at 10 *ms/frame* at a scan speed of $5mm/s$, hence an effective resolution of 50 μm. At these acquisition parameters, the total acquisition time is $20s$.

6.5 Conclusion

Layed-out in this chapter are the details of the full assembly of the Picasso detector consisting four layers grouped in couples and mounted one in front of the other. The hardware, architecture and the controller delays are introduced.

Since the sensor separation of the beam's path is severly crucial, the mounting of the layers has been assessed. This is a critical measure because one needs to be assured that the whole height of the pixel is fully illuminated. Since the pixel element of the sensor is not a square, the line spread function has been evaluated both at the horizontal and vertical directions. We have seen that the size of the pixel diminishes with a decreased threshold while the aparent size increases with increased threshold.

Moreover, the detector was tested at a framing rate of $10ms/frame$, the fastest so far achieved with the four layers. With this respect, an image of a standard mamographic phantom has been acquired through a scan mode acquisition to simulate a typical woman's breast. The full system was able to sustain with high stability the scan for the full length of the phantom.

Challenges has been met with the sensor separation of the sensors, especially at the back detectors. Initial assessment showed us that they were not optimally illuminated. Nonetheless, this matter has been addressed by our colleagues at the INFN mechanical workshop, but recent data for the modified allignment are no longer included in this thesis.

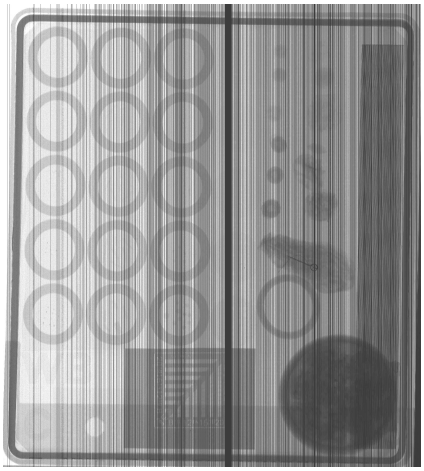

(a) Top Front

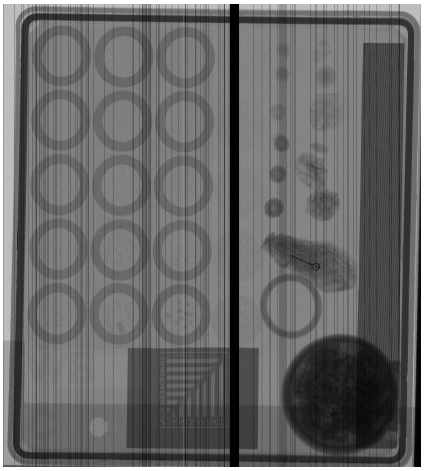

(b) Bottom Front

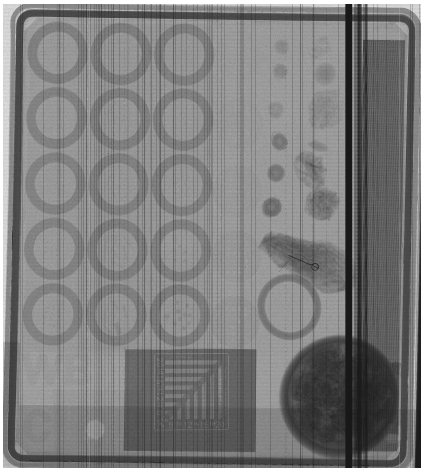

(c)Top Back

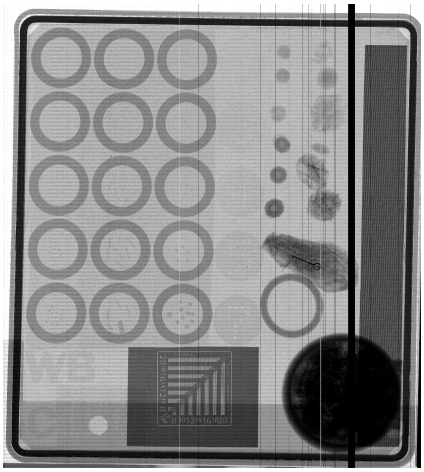

(d) Bottom Back

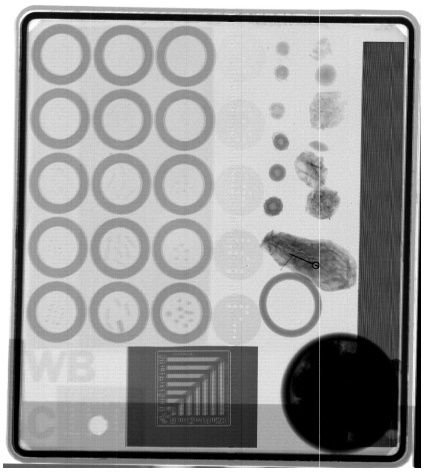

(e) Fused image coming from the four layers of the detector.

Figure 6.9: (a) to (d) Images of an Ackerman phantom coming form the different layers of the Picasso detector. (e) The fused imaged coming from (a) to (d). The object was scanned at continous mode in the vertical direction at $10ms/frame$ at a scan speed of $5mm/s$ resulting to an effective resolution of 50μm. The test object measures $10cm\ x\ 8cm$, and the total acquisition time is $20s$.

Conclusions

Breast cancer continues to be one of the most common lethal malignancy in women across the globe. In the cancer group, it accounts to more than 20% the total new cancer cases, and 14 % of the total cancer deaths [1]. More than half of the deaths are estimated to occur in economically developing nations. The battle remained over the past years, however based from the latest annual report issued by the American Cancer Society, the mortality rates has decreasing by 2.2% per year [5], thanks to the improvements of breast cancer treatment and early detection.

Mammography for many years has been the golden standard for breast cancer detection. Good quality mammograms are also effective means to screen a high-risk population to detect these malignancies at early stages where treatment is an option for long-term survival. However, mammography has some limitations. Not all breast cancer will be detected by a present day mammogram, and some breast cancers still have poor prognosis. Also, a small percentage of of breast cancers detected by screening (particularly ductal carcinoma *in-situ*), would have not progressed and thus may be treated uncessarily [127]. Futhermore, mammography sometimes leads to additional or follow-up examinations, that are often determined not to be cancer.

Nonetheless the above drawbacks, mammography continues to have great potentials in saving lives over other available screening and detection methods. However, improvements may still come from the development of innovative sources coupled with better digital detection systems. These advancements may also be taken advantage by people who are involved in research to develop new imaging techniques that can dynamically enhance the diagnostic capabilities of breast imaging.

Monochromatic and coherent sources escalates the image quality since unuseful low energy beams are absent, unlike that of conventional sources that produce polychromatic beams. In Chapter 1, we have mentioned that high intensity beams like that from synchrotron sources are monochromatised but still getting sufficient intensity in order to implement a clinical program. Moreover, since these beams are also coherent, they also allow scrutiny of phase shift of beams passing through samples by detecting scattered photons or interference from diffracted or undiffracted waves. Several methods has been developed and implemented in synchrotron facilities to understand both absorption and phase-contrast effects [101] to improve X-ray imaging, that everybody hopes to be implemented with ease in hospitals.

The SYRMEP beamline at Elettra Sincrotrone in Trieste (Italy) is involed with a clinical project, mainly in mammography, employing propagation-based phase-contrast techniques. The SYRMEP team has been successful implementing the first phase of the project, where commercial screen-film systems were used. Along with their goals is to be able to perform the program using a *in-house*-developed detector capable of detecting not only absorption but also phase-effects.

In this present thesis, the final step of the developement of a Silicon microstrip detector has been completed. A Silicon microstrip detector with an active area equal to a synchrotron cross-section is on its way to installation at the mammography facility of the SYRMEP beamline. The detection system called PICASSO (Phase Imaging for Clinical Application with Silicon detector and Synchrotron radiatiOn), developed in this work rely on direct conversion sensor and photon-counting readout. The microstrips are oriented parallel with the incident beam, which provides high detection efficiency in the photon range useful for mammography. The detector pixel size is given by the strip pitch (50μm) and the wafer height (300μm). The sensitivity of the sensors gives a good opportunity to perform single photon counting readout.

The readout electronics has been upgraded in order to meet the demands of the mammography project of SYRMEP. In this light, the thesis was aligned to the development of a new readout system for the four layers of the Picasso detector that is compact, fast, low noise and reliable for clinical research. With a new architecture, the firmware for the detector and controller boards have been havily modified, based on the ones developed by the Detector Group of the Swiss Light Source. A software has been created for the

management of the detector parameters and the data transfer based on TCP/IP communication. In its final configuration, a *multiDetector* class has been created to run the detector in parallel. The designs concerning these are mentioned in Chapter 3 and Chapter 6. The time needed to read the ASICs requires 150μs while the delay between the controllers spans around 750μs.

On several occasions, the detector (in part and in whole) has been brought to the SYRMEP beamline for tests. Images of mammographic test objects and excised breast samples have been acquired in both absorption and phase-contrast modes. Moreover, imaging was also performed to simulate clinical conditions where the acquisition time, field of view and counting rates are of the essence.

Moreover, the availability of phase effects using phase sensitive techniques have been demonstrated with the Picasso detector as was presented in Chapter 5.

Overall, this compact detector performed well in terms interms of electronics and imaging. It has also demonstrated compatibility with absorption and phase-contrast imaging, as called for by the Picasso project.

The graphical interface for the whole detector prototype in not yet complete. Future work on this endeavor would simplify the acquisition for the users. Also, efforts must done to bring down the delay between controllers to fully claim that the detector works in parallel. The detector needs proper integration with the instrumentation relevant to the the clinical room of the SYRMEP beamline. This means that the detection system will be able to communicate with the control and safety systems of the mamography station.

Bibliography

[1] Jemal, A. *et al.* Global Cancer Statistics *CA CANCER J CLIN* (2011) 61 69-90 doi:10.3322/caac.20107

[2] Abdulrahman, GOJ. and Rahman,GA. Epidemiology of Breast Cancer in Europe and Africa *Journal of Cancer Epidemiology* (2012) 2012 1-5 doi:10.1155/2012/915610

[3] Autier, P. *et al.* Breast cancer mortality in neighboring European countries with different levels of screening but similar access to treatment:trend analysis of WHO mortality database *BJM* (2011) 343:d4411 1-10 doi:10.1136/bmj.d4411

[4] Greenwald, P. and Dunn,BK. Landmarks in the History of Cancer Epidemiology *Cancer Res* (2009) 69:6 2151-2162 doi:10.1158/0008-5472.CAN-09-0416

[5] American Cancer Society. *Breast Cancer Facts and Figures* 2011-2012 Altlanta: American Cancer Society, Inc.

[6] Surveilance Epidemiology and End Results (SEER) Program. *SEER Cancer Statistics Review 1975-2009: Incidence and US death rates by Race/Ethnicity* (2011) http://seer.cancer.gov/csr/1975_2009_pops09/browse_csr.php?section=4&page=sect_04_zfig.04.html accessed 09/21/12 07:40:00 AM

[7] Cao, M. *et al.* Mammographic signs of systemic disease *Radiographics* (2011) 31 1085-1100 doi:10.1148/rg.314105205

[8] Abrami, A. *et al.* Medical applications of synchrotron radiation at the SYRMEP beamline at ELETTRA *Nuclear Instruments and Methods in Physics Research A* (2005) 548 1-2 221-227 doi:10.1016/j.nima.2005.03.093

[9] Röntgen, WK. On the new kind of rays *Nature* (1896) 53 274-276

[10] SYRMEP Specification http://www.elettra.trieste.it/lightsources/elettra/elettra-beamlines/syrmep/specification.html accessed 20 November 2012

[11] Jackson, JD. Classical Electrodynamics Wiley New York, 1998 Third Edition Ch 14

[12] Rubenstein, E. *et al.* Transvenous coronary arteriography in humans using synchrotron radiation *Proc. Natl Acad. Sci. USA*(1986) 83 9742-9748

[13] Wallace, BA. Protien characterisation by synchrotron radiation circular dichroism spectroscopy *Quarterly Reviews of Biophysics* (2009) 42 317-370 doi:10.1017/S00335835100003X

[14] Hendrickson, WA. Determination of macromolecular structures from anomalous diffraction of synchrotron radiation *Science* (1991) 254 51-58 doi:10.1126/science.1925561

[15] Poulsen, HF. *et al.* Three-dimensional maps of grain boundaries and stress state of individual grains in polycrystals and powders *Journal of Applied Crystallography* (2001) 34 751-756 doi:10.1107/S0021889801014273

[16] Rossmann, MG. Synchrotron radiation as a tool for investigating virus structures *J. Synchrotron Rad.* (1999) 6 816-821 doi:10.1107/S0909049599005075

[17] Synchrotron Radiation for Materials Science Applications www.coe.berkeley.edu/AST/srms

[18] Mobilio, S. and Balerna, A. Introduction to the main properties of Synchrotron Radiation In Mobilio and Vlaic, editors, Synchrotron Radiation: fundamentals, methodologies and applications, pages 1,23. SIF, Bologna, 2003.

[19] Atwood, D. Soft X-rays and extreme ultraviolet radiation: Principles and Applications Cambridge University Press Cambridge 1999

[20] Shenoy, G. Basic characteristics of Synchrotron radiation *Structural Chemistry* (2003) 14 3-14 doi:10.1023/A:1021656723964

[21] Shi, W. SASE X-ray Free Electron Laser in DESY - The 4th Generation Light Source *Journal of the GCPD eV* (2000) 6 5-16

[22] Pellegrini, C. *et al.* Optimization of an X-ray SASE-FEL *Nucl. Instrum. Meth. Phys. Res. A* (2001) 475 328-3

[23] Parmigiani, F. *et al.* The FERMI@Elettra free-electron-laser source for coherent x-ray physics: photon properties, beam transport system and applications *New Journal of Physics* (2010) 12 2-17 doi:10.1088/1367-2630/12/7/075002

[24] Patterson, BD. *et al.* Coherent science at the SwissFEL X-ray laser *New Journal of Physics*(2012) 12 2-17 doi:10.1088/1367-2630/12/3/035012

[25] Kim, KJ Brightness and Coherence of Radiation from undulators and high gain free electron lasers *IEEE* (1987)

[26] Arfelli, F. *et al.* Mammography with synchrotron radiation:phase-detection techniques *Radiology* (2000) 215 286293

[27] Cloetens, P. *et al.* Hard x-ray phase imaging using simple propagation of a coherent synchrotron radiation beam *J. Phys. D:App. Phys* (1999) 32 A145-A151 doi:10.1088/0022-3727/32/10A/330

[28] Introduction and History Elettra Light Source http://www.elettra.trieste.it/lightsources/elettra/elettra-intro.html?showall= accessed 20 November 2012

[29] Heinzmann, U. Angle, energy and spin-resolved photoelectron emission using circularly polarized synchrotron radiation *Physica Scripta* (1987) 17 77-88

[30] Karantzoulis, E. *et al.* Top-up implementation and operation at Elettra *Proceedings of the 1st International Particle Accelerator Conference* 23-28 May 2010 Kyoto, Japan.

[31] Kalantari, B. *et al.* Enhancements of top-up operation at the Swiss Light Source *Proceedings of 9th European Particle Accelerator Conference* 5-9 July 2004 Lucerne, Switzerland

[32] Bovi, M. *et al.* Absolute air-kerma measurement in a synchrotron radiation beam by ionization freeair chamber *Proceedings of the Absorbed Dose and Air Kerma Primary Standards Workshop* Paris, France, May 911, 2007. Published October 2, 2007 http://www.nucleide.org/ADAKPS_WS/Session%20G%20-%20Special%20Standards/G4_PaToni.pdf

[33] Castelli, E. *et al.* Mammography with synchrotron radiation: first clinical experience with phase-detection technique *Radiology* (2011) 259 684-694 doi:10.1148/radiol.11100745

[34] Arfelli, F. *et al.* Synchrotron radiation mammography: Clinical experimentation *AIP Conf. Proc.* (2007) 879 1895-1898 doi:10.1063/1.2436442

[35] Dreossi, D. *et al.* The mammography project at the SYRMEP beamline *Eur. J. Radiol.* (2008) 63 S58-S62 doi:10.1016/j.ejrad.2008.04.038

[36] Leo, WR. Techniques for Nuclear and Particle Physics Experiments: A How-to Approach Springer Verlag New York p210

[37] Leroy, C. and Rancoita, PG. Principles with radiation intection with matterand detection, 2nd Edition *World Scientific* New Jersey Ch6

[38] Hall, G. Semiconductor particle tracking detectors *Rep. Prog. Phys.* (1994) 57 481-531 doi:10.1088/0034-4885/57/5/002

[39] Straulino, S. Spatial resolution of double-sided silicom microstrip detectors for the PAMELA apparatus *Nucl. Instrum. Meth. Phys. Res. A* (2006) 556 100-114 doi:10.1016/j.nima.2005.10.014

[40] Carter, JR. *et al.* The silicon microstrip sensors of the ATLAS semiconductor tracker *Nucl. Instrum. Meth. Phys Res A* (2007) 578 98118 doi:10.1016/j.nima.2007.04.157

[41] Bergamaschi, A. *et al.* The MYTHEN detector for X-ray powder diffraction experiments at the Swiss Light Source *J. Synch. Rad.* (2010) 17 653-668 doi:10.1107/S0909049510026051

[42] Bornefalk, H. and Danielsson, M. Photon-counting spectral computed tomography using silicon strip detectors: a feasibility study *Phys. Med. Biol.* (2010) 55 1999- doi:10.1088/0031-9155/55/7/014

[43] Arfelli, F. *et al.* Design and evaluation of AC-coupled FOXFET-biased "edge-on" silicon strip detectors for X-ray imaging *Nucl. Instrum. Meth. Phys. Res. A* (1997) 385 311-320 doi:10.1016/S0168-9002(96)01076-5

[44] Vallazza, E. *et al.* A double layer silicon detector for single photon counting *Proc of the 10th ICATPP Conference* (2008) 2-12 October 2007 Como, Italy World Scientific Publishing doi:10.1142/9789812819093_0117

[45] Bergamaschi, A. *et al.* FROST: an ASIC for digital mammography with synchrotron radiation *Nucl. Instrum. Meth. Phys. Res. A* (2003) 510 51-56 10.1016/S0168-9002(03)01678-4

[46] Lutz, G. Semiconductor radiation detectors: Device Physics Springer Verlag Berlin 1999 Ch7

[47] Baricchello, G. Performance of long modules of silicon microstrip detectors *CERN PPE/92-132* December 11,1997

[48] Rashevskaya, I. *et al.* Investigation on an abnormal patterm of leakage currents in silicon micristrip detectors *Nucl. Instrum. Meth. Phys Res A* (2010) 617 582-584 doi:10.1016/j.nima.2009.09.046

[49] Simi, G .*et al.* Design and characterization of integrated front-end transistors in a micro-strip detector technology *Nucl. Instrum. Meth. Phys Res A* (2002) 485 193-198 10.1016/S0168-9002(02)00554-5

[50] Harper, RD. *et al.* Evaluation of silicon microstrip detector currents during proton irradiation at the CERN PS *Nucl. Instrum. Meth. Phys Res A* (2002) 479 548-554

[51] Johnson, JB. Thermal agitation of electricity in conductors *Physical Review* (1928) 32 97-108 doi:10.1103/PhysRev.32.97

[52] Nyquist, H. Thermal agitation of electric charge in conductors *Physical Review* (1928) 32 110-113 doi:10.1103/PhysRev.32.110

[53] Hara, K. *et al.* Prototype Si microstrip sensors for the CDF-II ISL detector *Nucl. Instrum. Meth. Phys Res A* (1999) 435 437-445 doi:10.1016/S0168-9002(99)00653-1

[54] Meschini, M. *et al.* Performace of CMS silicon microstrip detectors with the AVP readout chip *Nucl. Instrum. Meth. Phys Res A* (2000) 447 133-141 doi:10.1016/S0168-9002(00)00181-9

[55] Xray Mass Attenuation Coefficient http://physics.nist.gov/PhysRefData/XrayMassCoef/ElemTab/z14.html NIST

[56] Olivo, A. *et al.* Experimental evaluation of a simple algorithm to enhance the spatial resolution in scanned radiographic systems *Med. Phys.* (2000) 27 2609-2616 doi:10.1118/1.1318219

[57] Vrtacnik, D. *et al.* Side-illuminated 100 μm pitch X-ray detector for digital radiology *Sensors and Actuators* (2000) 85 209-216 http://dx.doi.org/10.1016/S0924-4247(00)00381-2

[58] Vrtacnik, D. *et al.* Investigation of cutting edge in edge-on silicon microstrip detector *Nucl. Instrum. Meth. Phys Res A* (2010) 620 557-562 doi:10.1016/j.nima.2010.03.144

[59] Wu, X. *et al.* Recent advances in processing and characterization of edgeless detectors *JInst* (2011) 7 1-10 doi:10.1088/1748-0221/7/02/C02001

[60] Mori, R. *et al.* Charge collection measurements on slim-edge microstrip detectors *JInst* (2012) 7 1-9 doi:10.1088/1748-0221/7/05/P05002

[61] Bomben M. *et al.* Novel Silicon n-on-p Edgeless Planar Pixel Sensors for the ATLAS upgrade (2012) arXiv:1212.3580v1

[62] Yun, S. *et al.* Detective quantum efficiency of a silicon microstrip photon-counting detector having edge-on geometry under mammography imaging condition *JInst* (2011) 6 C12006 doi:10.1088/1748-0221/6/12/C12006

[63] Åslund, M. *et al.* Physical characterization of a scanning photon counting digital mammography system based on Si-strip detectors *Med. Phys.* (2007) 34 1918-1925 doi:10.1118/1.2731032

[64] Lundqvist, M. *et al.* Computer simulations and performance measurements on a silicon strip detector for edge-on imaging *IEEE Trans Nucl. Sci.* (2000) 47 1487-1492 doi:10.1109/23.873002

[65] Bollini, D. *et al.* Energy resolution of a silicon detector with the RX64 ASIC designed for X-ray imaging *Nucl. Instrum. Meth. Phys. Res. A* (2003) 515 458-466 doi:10.1016/j.nima.2003.07.02

[66] Baldazzi, G. *et al.* X-ray imaging with a silicon microstrip detector coupled to the RX64 ASIC *Nucl. Instrum. Meth. Phys. Res A* (2003) 509 315-320 doi:10.1016/S0168-9002(03)01643-7

[67] Mozzanica, A. *et al.* Mythen II: A 128 channel single photon counting read-out chip *Nucl. Instrum. Meth Phys. Res. A* (2009) 250-252 doi:10.1016/j.nima.2009.03.166

[68] Rigon, L. *et al.* Breast computed tomography with the PICASSO detector:A feasibility study *Nucl. Instrum. Meth Phys. Res. A* (2011) 628 419422 doi:10.1016/j.nima.2010.07.015

[69] Lopez, F. *et al.* Development of a fast read-out system of a single photon counting detector for mammography with synchrotron radiation *JInst* (2011) 6 C12031 1-6 doi:10.1088/1748-0221/6/12/C12031

[70] Altera http://www.altera.com/

[71] Axis LX100 http://www.axis.com/files/datasheet/etrax/etrax_lx_ds_18354.pdf

[72] Scientific Linux https://www.scientificlinux.org/

[73] GNU Compiler Collection http://gcc.gnu.org/

[74] Radeka, V. Low-noise techniques in detectors *Ann. Rev. Nud. ParI. Sci.* (1988) 38 217-277

[75] Mitchel, T. *et al.* A fundamental method to determine the signal-to-noise ratio (SNR) and detective quantum efficiency (DQE) for a photon counting pixel detector *Nucl. Instrum. Meth. Phys. Res. A* (2006) 568 799802 doi:/10.1016/j.nima.2006.08.115

[76] Bergamaschi, A. *et al.* Performance of a single photon counting microstrip detector for strip pitches down to 10 μm *Nucl. Instrum. Meth. Phys. Res. A* (2008) 591 163166 doi:10.1016/j.nima.2008.03.048

[77] Marchal, J. Theoretical analysis of the effect of charge-sharing on the Detective Quantum Efficiency of single-photon counting segmented silicon detectors *JInst* (2010) 5 P01004 doi:10.1088/1748-0221/5/01/P01004

[78] Kraft, P. *et al.* Characterization and calibration of PILATUS detectors *IEEE Trans. Nuc. Sci.* (2009) 56 758-764 doi:10.1109/TNS.2008.2009448

[79] Trueb, P. *et al.* Improved count rate corrections for highest data quality with PILATUS detectors *J. Synch. Rad.* (2012) 19 347351 doi:10.1107/S0909049512003950

[80] Uesugi, M. *et al.* Comparison of lens-and fiber-coupled CCD detectors for X-ray computed tomography *J. Synch. Rad.* (2011) 18 217-223 doi:10.1107/S0909049510044523

[81] Rigon, L. *et al.* A single-photoncounting *edge-on* silicondetector for synchrotron radiation mammography *Nucl. Instrum. Meth. Phys. Res. A* (2009) 608 S62S65 doi:10.1016/j.nima.2009.05.036

[82] Coan, P. *et al.* Evaluatioin of imaging performance of a taper optics CCD FReLon camera designed for medical imaging *J. Synch. Rad.* (2006) 13 260-270 doi:10.1107/S0909049506008983

[83] Yagi, N. *et al.* A large-area CMOS imager as an X-ray detector for synchrotron radiation experiments *J. Synch. Rad.* (2004) 11 347-352 doi:10.1107/S0909049504008519

[84] Fredenberg, E. *et al.* Contrast-enhanced spectral mammography with a photon-counting detector *Med. Phys.* (2010) 37 2017-2029 doi:10.1118/1.3371689

[85] http://www.leedstestobjects.com/

[86] Chen, R. *et al.* Measurement of the linear attenuation coefficients ofbreast tissues by synchrotron radiation computedtomography *Phys. Med. Biol.* (2010) 55 4993-5005 doi:10.1088/0031-9155/55/17/008

[87] Rose, A. The sensitivity of the human eye on an absolute scale *J. Opt. Soc. Am. A* (1948) 38 196

[88] Burgess, A. The Rose model, revisited *J. Opt. Soc. Am. A* (1999) 16 633 doi:10.1364/JOSAA.16.000633

[89] Webb, S. The Physics of Medical Imaging *Taylor and Francis* New York USA (1988)

[90] Johns, HE. and Cunningham, JR. The Physics of Radiology, 4th Ed., *C. Charles Thomas Publisher* Illinois U.S.A. (1983).

[91] Olivo, A. *et al.* An innovative digital imaging set-up allowing a low-dose approach to phase contrast applications in the medical field *Med. Phys.* (2001) 1610-1619 doi:10.1118/1.1388219

[92] Bergamaschi, A. A high performance detection system for breast tomography with synchrotron radiation (2005) PhD Thesis University of Trieste

[93] Boone, J. Normalized glandular dose DgN coefficients for arbitrary x-ray spectra in mammography: Computer-fit values of Monte Carlo derived data *Med. Phys.* (2002) 29 doi:10.1118/1.1472499

[94] Munro, P. *et al.* A quantitative, non-interferometric X-ray phase contrast imaging technique *Optics Express* (2013) 21 647-661 doi:10.1364/OE.21.000647

[95] Suortti, P. and Thomlinson, W. Medical applications of synchrotron radiation *Phys. Med. Biol.* (2003) 48 R1R35 doi:10.1088/0031-9155/48/13/201

[96] Born, M. and Wolf, E. Principles of Optics : Electromagnetic theory of propagation, interference and diffraction of light, 7th edition 1999 Cambridge University Press

[97] Peterzol, A. *et al.* The effects of the imaging system on the validity limits of the ray-optical approach to phase contrast imaging *Med. Phys.* (2005) 32 3617-3627 doi:10.1118/1.2126207

[98] Lewis, A. Medical phase contrast x-ray imaging: current status and future prospects *Phys. Med. Biol.* (2004) 49 35733583 doi:10.1088/0031-9155/49/16/005

[99] Zhou, S. and Brahme, A. Development of phase-contrast X-ray imaging techniques and potential medical applications *Physica Medica* (2008) doi:10.1016/j.ejmp.2008.05.006

[100] Snigirev, A. *et al.* On the possibilities of x-ray phase-contrast microimaging by coherent high-energy synchrotron radiation *Rev. Sci. Instrum* (1995) 66 5486-5492 doi:10.1063/1.1146073

[101] Bravin, A. *et al.* X-ray phase-contrast imaging: from pre-clinical applications towards clinics. *Phys. Med. Biol.* (2013). 58 R1-R35 doi:10.1088/0031-9155/58/1/R1

[102] Arfelli, F. *et al.* Low-dose phase contrast x-ray medical imaging *Phys. Med. Biol.* (1998) 43 28452852 doi:10.1088/0031-9155/43/10/013

[103] Chapman, D. Diffraction enhanced x-ray imaging *Phys. Med. Biol* (1997) 20152025 doi:10.1088/0031-9155/42/11/001

[104] Keyrilainen, J. *et al.* Toward high-contrast breast CT at low radiation dose *Radiology* (2008) 249 321-327 doi:10.1148/radiol.2491072129

[105] Rigon, L. *et al.* Three-image diffraction enhanced imaging algorithm to extract absorption, refraction, and ultrasmall-angle scattering *Appl. Phys. Lett.* (2007) 90114102 doi:10.1063/1.2713147

[106] Hu, C. *et al.* Comparison of refraction information extraction methods in diffraction enhanced imaging. *Optics Express* (2008) 21 16704-16710doi:10.1364/OE.16.016704

[107] Pagot, E. *et al.* Quantitative comparison between two phase contrast techniques: diffraction enhanced imaging and phase propagation imaging *Phys. Med. Biol.* (2005) 50 709724 doi:10.1088/0031-9155/50/4/010

[108] Nesterets, YI. *et al.* On qualitative and quantitative analysis in analyser based imaging *Acta Crystallogr.* (2006) 62 296308 doi:10.1107/S0108767306017843

[109] Diemoz, P *et al.* Absorption, refraction and scattering in analyzer-based imaging: comparison of different algorithms *Optics Express* (2010) 18, 3494-3509 doi:10.1364/OE.18.003494

[110] Diemoz, P. *et al.* Comparison of analyzer-based imaging computed tomography extraction algorithms and application to bone-cartilage imaging *Phys. Med. Biol.* (2010) 55 7663-7679 doi:10.1088/0031-9155/55/24/018

[111] Bonse, U. and Hart, M. An X-ray interferometer *Applied Physics Letters* (1965) 6 155-156

[112] Momose, A. Recent advances in X-ray phase imaging *Jap. J. App. Phys.* (2005) 44 63556367 doi:10.1143/JJAP.44.6355

[113] Momose, A. Phase-sensitive imaging and phase tomography using X-ray interferometers *Optics Express* (2003) 11 2303-2314 doi:10.1364/OE.11.002303

[114] Momose, A. Demonstration of phase-contrast x-ray computed-tomography using an x-ray interferometer *Nucl. Instrum. Meth. Phys. Res. A* (1995) 352 622628 doi:10.1016/0168-9002(95)90017-9

[115] Takeda, T. *st al* Vessel imaging by interferometric phase-contrast X-ray technique *Circulation* (2002) 105 1708-1712. doi:10.1161/01.cir.0000012752.35225.6c

[116] Weitkamp, T. *et al* X-ray phase imaging with a grating interferometer *Optics Express* 13 6296-6304 doi:10.1364/OPEX.13.006296

[117] Pfeiffer, F. *et al.* Phase retrieval and differential phase-contrast imaging with low-brilliance X-ray sources *Nature Physics* 2 258-261 doi:10.1038/nphys265

[118] Zambelli, J. *et al.* Radiation dose efficiency comparison between differential phase contrast CT and conventional absorption CT *Med. Phys.* (2010) 37 2473-2479 doi:10.1118/1.3425785

[119] Munro, P. *et al.* Source size and temporal coherence requirements of coded aperture type x-ray phase contrast imaging systems *Optics Express* (2010) 18 19681-19692 doi:10.1364/OE.18.019681

[120] Olivo, A. and Speller,R. A coded-aperture technique allowing x-ray phase contrast imaging with conventional sources *Appl. Phys. Let.* (2007) 91 0741061-3 doi:10.1063/1.2772193

[121] Olivo, A. and Speller, R. Modelling of a novel x-ray phase contrast imaging technique based on coded apertures *Phys. Med. Biol.* (2007) 52 6555-6573 doi:10.1088/0031-9155/52/22/001

[122] Henke, B. *et al.* X-ray interactions: photoabsorption, scattering, transmission, and reflection at E = 50-30,000 eV, Z = 1-92 *Atomic Data and Nuclear Data Tables* (1993) 54 181-342 doi:10.1006/adnd.1993.1013

[123] Longo,M. A quantitative study of coded-aperture based X-ray phase contrast imaging with synchrotron radiation (2011) Master's Thesis Univeristy of Trieste

[124] Samei, E. *et al.* A method for measuring the presampled MTF of digital radiographic systems using an edge test device *Med. Phys.* (1998) 25 102-113. doi:10.1118/1.598165

[125] Rigon, L. *et al.* Evaluation of charge-sharing effects on the spatial resolution of the PICASSO detector *Nucl. Instrum. Meth. Phys. Res. A* (2010) 617 244-245 doi:10.1016/j.nima.2009.09.007

[126] Bergamaschi, A. *et al.* Beyond single photon counting X-ray detectors *Nucl. Instrum. Meth. Phys. Res. A* (2011) 628 238241 doi:10.1016/j.nima.2010.06.326

[127] Duffy, SW. *et al.* Absolute numbers of lives saved and overdiagnosis in breast cancer screening from a radomised trial and from the Breast Screening program in England *J. Med. Screen* (2010) 17 25-30 doi:10.1258/jms.2009.009094

Acknowledgement

Much acknowledgement is accorded to the following people who are important in the realization of this work....

Sgra. Lia Brautti and to the Brautti family, for the opportunity to undertake a PhD activity in Trieste. Much appreciation is accorded to them because they value science and its relevance to the society.

Prof. Edoardo Castelli for the opportunity to undertake the challenge with the PICASSO detector.

Prof. Renata Longo for acting as my supervisor on this project. Thank you for asking me to continue the work at the time that I almost did not want to finish it.

Dr. Bernd Scmhitt and Dr. Anna Bergamaschi, and the SLS Detector Group in Switzerland, from whom I owe everything I now know about detector technology. Thank you for teaching me to be resilient amidst demanding and sometimes unreasonable detector users. All of you have been a joy to work with.

the SYRMEP group : Dr. Luigi Rigon and Dr. Fulvia Arfelli for their availability and sharing their technical *know-hows* on detector and imaging demands. To the beamline scientists that I came accorss at the SYRMEP beamline for the assistance : Dr. Giuliana Tromba, Dr. Diego Dreossi and Dr. Nicola Sodini.

Dr. Erik Vallazza for the assistance. To Chen and Mariaconcetta for the express data. To collaborators whom I learned imaging from.

the engineers and technicians of INFN-Trieste, who have been kind in assisting with technical concerns about electronics.

and to Dario Manzoni, who patiently waited and stood beside me until this thesis work is over. <3